INFORMATION TO USERS

This manuscript has been reproduced from the microfilm master. UMI films the text directly from the original or copy submitted. Thus, some thesis and dissertation copies are in typewriter face, while others may be from any type of computer printer.

The quality of this reproduction is dependent upon the quality of the copy submitted. Broken or indistinct print, colored or poor quality illustrations and photographs, print bleedthrough, substandard margins, and improper alignment can adversely affect reproduction.

In the unlikely event that the author did not send UMI a complete manuscript and there are missing pages, these will be noted. Also, if unauthorized copyright material had to be removed, a note will indicate the deletion.

Oversize materials (e.g., maps, drawings, charts) are reproduced by sectioning the original, beginning at the upper left-hand corner and continuing from left to right in equal sections with small overlaps. Each original is also photographed in one exposure and is included in reduced form at the back of the book.

Photographs included in the original manuscript have been reproduced xerographically in this copy. Higher quality 6" x 9" black and white photographic prints are available for any photographs or illustrations appearing in this copy for an additional charge. Contact UMI directly to order.

UMI

A Bell & Howell Information Company
300 North Zeeb Road, Ann Arbor MI 48106-1346 USA
313/761-4700 800/521-0600

Continuum Damage Model for Plastic Fracture of Work-Hardening Materials

by

KHALED M. MAHMOUD

A dissertation submitted to the Graduate Faculty in Engineering in partial fulfillment of the requirements for the degree of Doctor of Philosophy, The City University of New York

1997

This manuscript has been read and accepted for the Graduate Faculty in Engineering in satisfaction of the dissertation requirements for the degree of Doctor of Philosophy.

September 17, 1997
Date

Mumtaz K. Kassir
Chair of Examining Committee

9/17/97
Date

Executive Officer

Professor Feridun Delale

Professor Charles Miller

Professor Michel Ghosn

Dr. Kamal Bandyophadyay

Supervisory Committee

The City University of New York

Abstract

Continuum Damage Model for Plastic Fracture of Work-Hardening Materials

by

KHALED M. MAHMOUD

Adviser: Professor Mumtaz K. Kassir

This dissertation proposes a continuum damage model for plastic fracture of work-hardening materials containing cracks subjected to mode I and mode III loadings. The model, which is based on interaction between a well-developed crack and microvoids ahead of its tip, describes the conditions necessary for the onset of crack instability, fatigue crack propagation due to cyclic loading, and rates of crack growth due to steady-state creep. This is accomplished through the introduction of a mechanical damage variable into the constitutive equations of an elastic-plastic formulation of a work-hardening material. The main hypothesis throughout the dissertation is that damage is proportional to the crack opening displacement.

Because of mathematical simplicities, an anti-plane stationary crack subjected to shear loading (mode III) is dealt with first to illustrate the model. A hodograph transformation is used to derive a closed form expression for the displacement, and also to determine a circular damage-zone engulfing the crack-tip. Damage is assumed confined within this damage-zone and any damage outside the zone is neglected. For an embedded stationary crack subjected

to remotely applied tensile loading (mode I), under plane strain conditions, the leading term of an asymptotic expression of the displacement is determined. Guided by the results of mode III, a circular damage-zone centered at the crack-tip is postulated.

A critical stress is determined and found to be proportional to $a_0^{-1/(n+1)}$ for crack extension and growth, where a_0 is the initial crack length and n is the strain hardening exponent. For fatigue crack propagation, a period of incubation (where damage accumulates without a crack extension) followed by a growth period and then failure are observed. The number of loading cycles required to cause the onset of crack growth and failure increases with reducing the external load and/or reducing the material parameters. For given material parameters, the influence of strain hardening on the number of cycles required for failure is revealed and shown graphically. In the steady-state creep, the incubation and growth periods that precede failure are also demonstrated. The elapsed time required to cause the onset of crack growth and failure is found to increase with a decrease in the external load, a decrease in the material parameter and/or an increase in the modular ratio. Variations of the normalized crack length with time are graphically exhibited.

To
my parents

Acknowledgment

I would like to express my deepest appreciation to my adviser, Professor Mumtaz K. Kassir, for the undivided attention he provided to me throughout the course of accomplishing this dissertation. I feel privileged to have him as my mentor.

I would like also to thank the members of my Doctoral Committee, Professor Feridun Delale, Professor Charles Miller, Professor Michel Ghosn and Dr. Kamal Bandyophadyay, for their constructive comments. Enlightening discussions with Professor Feridun Delale are gratefully acknowledged.

I am indebted to my family, for their encouragements, their prayers, and the constant support that they have offered. Words are inadequate to express my gratitude to my parents for their wisdom and strength. They have given me the opportunity for this education, they taught me how to aspire for knowledge and they have been always a source of inspiration.

Finally, I would like to thank Him, my Creator. He has always been my greatest encouragement and my Helper. By His grace, He has guided, corrected and protected me. His Word has been a continual source of comfort, guidance and Wisdom.

CONTENTS

List of Tables x
List of Figures xi
List of Notations xvi

1 **INTRODUCTION** 1

1.1 Historical Background 2
1.2 Objective of Dissertation 6
1.3 Organization of Dissertation 8

2 **DAMAGE FIELD FOR A CRACK SUBJECTED TO ANTI-PLANE SHEAR LOADING (MODE III)** 11

2.1 Introduction 11
2.2 Summary of Basic Equations 13
2.3 Determination of Damage-Zone 18
2.4 Criterion for Crack Instability 24
2.4.1 Small-Scale Yielding Solution 25
2.4.2 Large-Scale Yielding Solution 26
2.5 Fatigue Crack Propagation 28

3 **MODE III NUMERICAL RESULTS AND DISCUSSION** 31

3.1 Introduction 31
3.2 Criterion for Crack Instability 32
3.3 Fatigue Crack Propagation 34

4 **TIME -DEPENDENT DAMAGE FIELD FOR A CRACK SUBJECTED TO ANTI-PANE SHEAR LOADING (MODE III)** 53

4.1 Introduction 53
4.2 Time-Dependent Basic Equations 58
4.3 Time-Dependent Damage 61
4.4 Time-Dependent Crack Growth Numerical Results 64
4.4.1 Creep Crack Growth 65
4.4.2 Theoretical Instability Time 87

5 **DAMAGE FIELD FOR A CRACK SUBJECTED TO TENSILE LOADING (MODE I)** 91

5.1 Introduction 91

5.2 Summary of Basic Equations 93
5.3 Damaged Material Governing Equations 98
5.4 Determination of Damage-Zone 103
5.5 Criterion for Crack Instability 110
5.5.1 Small-Scale Yielding Solution 111
5.5.2 Large-Scale Yielding Solution 112
5.6 Fatigue Crack Propagation 116
5.7 Time-Dependent Crack Propagation 119
5.7.1 Introduction 119
5.7.2 Time-Dependent Basic Equations 120
5.7.3 Steady-State Creep Crack Growth 123

6 MODE I NUMERICAL RESULTS AND DISCUSSION 125

6.1 Introduction 125
6.2 Criterion for Crack Instability 126
6.3 Fatigue Crack Propagation 130
6.4 Time-Dependent Crack Growth 137
6.4.1 Steady-State Creep Crack Growth 137
6.4.2 Theoretical Instability Time 147

7 SUMMARY AND CONCLUSIONS 151

8 SUGGESTIONS FOR FUTURE RESEARCH 153

References 154

List of Tables

Table 2.1 Numerical values of the function h(n) in equation (2.46). 27

Table 5.1 Numerical values of the function h_I (n) in equation (5.47). 114

List of Figures

Figure 2.1	Edge crack physical plane.	14
Figure 2.2	Map of physical plane into strain plane.	16
Figure 2.3	Geometry of small-scale yielding solution for anti-plane straining of a work-hardening elastic-plastic material.	22
Figure 2.4	Description of fatigue crack growth criterion.	30
Figure 3.1	Variation of the external stress, τ_∞/s_0, with crack length, a_0.	33
Figure 3.2	Crack growth due to cyclic loading at $\tau_\infty/s_0 = 0.4$ and $\eta s_0 a_0 /G = 0.02$.	37
Figure 3.3	Variation of number of cycles versus normalized crack length at $\tau_\infty/s_0 = 0.4$ and $\eta s_0 a_0 /G = 0.01$.	38
Figure 3.4	Influence of strain hardening on crack growth at $\tau_\infty/s_0 = 0.6$ and $\eta s_0 a_0 /G = 0.01$.	39
Figure 3.5	Principal appearance of the incubation and growth periods.	40
Figure 3.6	Influence of strain hardening exponent on number of cycles to the onset of crack growth at $\eta s_0 a_0 /G = 0.01$.	41
Figure 3.7	Number of cycles to failure versus external stress ratio at $\eta s_0 a_0 /G = 0.01$.	42
Figure 3.8	Variation of the material parameter, $\eta s_0 a_0 /G$, versus number of cycles to the onset of crack growth at $\tau_\infty/s_0 = 0.4$.	43
Figure 3.9	Influence of strain hardening exponent on the number of cycles to failure at $\tau_\infty/s_0 = 0.4$.	44
Figure 3.10	Variation of the strain hardening exponent with number of cycles to the onset of crack growth at $\eta s_0 a_0 /G = 0.01$, for $\tau_\infty/s_0 = 0.4$ and $\tau_\infty/s_0 = 0.8$.	45
Figure 3.11	Strain hardening exponent versus the number of cycles to failure at $\eta s_0 a_0 /G = 0.01$, for $\tau_\infty/s_0 = 0.4$ and $\tau_\infty/s_0 = 0.8$.	46

Figure 3.12	Influence of the material parameter, $\eta s_0 a_0 /G$, on fatigue crack growth at $\tau_{-}/s_0 = 0.4$ for $n = 3$.	47
Figure 3.13	Fatigue crack growth at different external stress ratios at $\eta s_0 a_0 /G = 0.02$ for $n = 3$.	48
Figure 3.14	Influence of material parameter, $\eta s_0 a_0 /G$, on number of cycles to the onset of crack growth for n=3.	49
Figure 3.15	Number of cycles to failure versus external stress ratio at different values of the material parameter, $\eta s_0 a_0 /G$, for n=3.	50
Figure 3.16	Variation of the material parameter, $\eta s_0 a_0 /G$, versus number of cycles to the onset of crack growth at different external stress ratio for n=3.	51
Figure 3.17	Influence of external stress ratio, τ_{-}/s_0, on number of cycles to failure for n=3.	52
Figure 4.1	Schematic creep behavior of a material subject to a constant stress.	54
Figure 4.2	Creep zones at the tip of a crack.	56
Figure 4.3	Description of creep crack growth criterion.	62
Figure 4.4	Crack growth due to steady-state creep at $\tau_{-}/s_0 = 0.4$, $H/G = 40$ and $\beta s_0 a_0 /G = 8$.	68
Figure 4.5	Variation of time versus normalized crack length at $\tau_{-}/s_0 = 0.4$, $H/G = 40$ and $\beta s_0 a_0 /G = 16$.	69
Figure 4.6	Influence of creep exponent on crack growth at $\tau_{-}/s_0 = 0.5$, $H/G = 40$ and $\beta s_0 a_0 /G = 8$.	70
Figure 4.7	Steady-state creep crack growth at $\tau_{-}/s_0 = 0.5$, $H/G = 20$ and $\beta s_0 a_0 /G = 8$.	71
Figure 4.8	Variation of time versus normalized crack length at $\tau_{-}/s_0 = 0.5$, $H/G = 10$ and $\beta s_0 a_0 /G = 6$.	72
Figure 4.9	Principal appearance of the incubation and growth periods.	73
Figure 4.10	Influence of creep exponent on elapsed time to the onset of crack growth at $H/G = 10$ and $\beta s_0 a_0 /G = 6$.	74

Figure 4.11	Elapsed time to failure versus external stress ratio at H/G = 10 and $\beta s_0 a_0 / G = 6$.	75
Figure 4.12	Variation of the material parameter, $\beta s_0 a_0 / G$, versus elapsed time to the onset of crack growth at $\tau_\infty / s_0 = 0.5$ and H/G = 10.	76
Figure 4.13	Influence of creep exponent on the elapsed time to failure at $\tau_\infty / s_0 = 0.5$ and H/G = 10.	77
Figure 4.14	Variation of the creep exponent versus time to the onset of crack growth at H/G = 10 and $\beta s_0 a_0 / G = 6$, for $\tau_\infty / s_0 = 0.3$ and $\tau_\infty / s_0 = 0.7$.	78
Figure 4.15	Influence of external stress ratio on the variation of creep exponent versus time to failure at H/G = 10 and $\beta s_0 a_0 / G = 6$.	79
Figure 4.16	Influence of the material parameter, $\beta s_0 a_0 / G$, on creep crack growth at $\tau_\infty / s_0 = 0.5$ and H/G=10, for n = 3.	80
Figure 4.17	Creep crack growth corresponding to different external stress ratios at H/G = 10 and $\beta s_0 a_0 / G = 4$, for n = 3.	81
Figure 4.18	Variation of time versus normalized crack length due to different values of H/G at $\tau_\infty / s_0 = 0.5$ and $\beta s_0 a_0 / G = 8$, for n = 3.	82
Figure 4.19	Influence of material parameter, $\beta s_0 a_0 / G$, on elapsed time to the onset of crack growth at H/G = 10, for n=3.	83
Figure 4.20	Elapsed time to failure versus external stress ratio at different values of the material parameter, $\beta s_0 a_0 / G$, for n=3.	84
Figure 4.21	Material parameter, $\beta s_0 a_0 / G$, versus time to the onset of crack growth due to different external stress ratios, at H/G = 10, for n=3.	85
Figure 4.22	Influence of external stress ratio, τ_∞ / s_0, on elapsed time to failure at H/G = 10 for n=3.	86
Figure 4.23	Influence of creep exponent on elapsed time needed to double the initial crack length at H/G = 10 and $\beta s_0 a_0 / G = 6$.	89
Figure 4.24	Influence of material parameters on elapsed time needed for doubling the initial crack length for n=3.	90

Figure 5.1	Notations at the crack-tip.	94
Figure 5.2	Two circular contours around the crack-tip.	100
Figure 5.3	Schematic of near-tip behavior under J-dominance conditions.	104
Figure 5.4	Definition of crack-tip opening displacement.	105
Figure 5.5	Approximate extensions of elastic-plastic boundary ahead and behind the crack-tip for plane strain of power-hardening material.	108
Figure 5.6	Large-strain crack-tip finite element results of McMeeking and Parks.	113
Figure 6.1	Variation of the external stress, σ_∞/s_0, with crack length, a_0.	127
Figure 6.2	Influence of Poisson's ratio on crack instability for n=20.	129
Figure 6.3	Crack growth due to cyclic loading at $\sigma_\infty/s_0 = 0.4$ and $\eta s_0 a_0 /E = 0.8$.	132
Figure 6.4	Variation of number of cycles versus normalized crack length at $\sigma_\infty/s_0 = 0.4$ and $\eta s_0 a_0 /E = 0.4$.	133
Figure 6.5	Influence of strain hardening on crack growth at $\sigma_\infty/s_0 = 0.6$ and $\eta s_0 a_0 /E = 0.8$.	134
Figure 6.6	Influence of the material parameter, $\eta s_0 a_0 /E$, on fatigue crack growth at $\sigma_\infty/s_0 = 0.4$ for $n = 2$.	135
Figure 6.7	Fatigue crack growth at different external stress ratios at $\eta s_0 a_0 /E = 0.8$ for $n = 2$.	136
Figure 6.8	Crack growth due to steady-state creep at $\sigma_\infty/s_0 = 0.5$, $F/E = 10$ and $\beta s_0 a_0 /E = 60$.	140
Figure 6.9	Variation of time versus normalized crack length at $\sigma_\infty/s_0 = 0.5$, $F/E = 10$ and $\beta s_0 a_0 /E = 120$.	141
Figure 6.10	Influence of creep exponent on crack growth at $\sigma_\infty/s_0 = 0.4$, $F/E = 10$ and $\beta s_0 a_0 /E = 60$.	142
Figure 6.11	Steady-state creep crack growth at $\sigma_\infty/s_0 = 0.4$, $F/E = 5$ and $\beta s_0 a_0 /E = 60$.	143

Figure 6.12 Influence of the material parameter, $\beta s_0 a_0 / E$, on creep crack growth at $\sigma_\infty / s_0 = 0.5$ and $F/E = 5$, for $n = 2$. 144

Figure 6.13 Creep crack growth corresponding to different external stress ratios at $F/E = 5$ and $\beta s_0 a_0 / E = 60$, for $n = 2$. 145

Figure 6.14 Variation of time versus normalized crack length due to different values of F/E at $\sigma_\infty / s_0 = 0.5$ and $\beta s_0 a_0 / E = 120$, for $n = 2$. 146

Figure 6.15 Influence of creep exponent on elapsed time needed to double the initial crack length at $F/E = 5$ and $\beta s_0 a_0 / E = 60$. 149

Figure 6.16 Influence of material parameters on elapsed time needed for doubling the initial crack length for n=2. 150

List of Notations

A	original cross-sectional area.
A_{net}	net cross-sectional area.
A_{void}	cross-sectional area occupied by voids.
a	crack length.
a_0	initial crack length.
$a(N)$	crack length at load cycle N.
$a(t)$	crack length at time t.
b	length of uncracked ligament.
C	plastic zone extension ahead of the crack-tip.
C^*	path-independent integral for a body undergoing steady-state creep.
D	damage variable.
$\dot{D}$	damage rate.
D_0	uniform component of damage.
d_n	strain hardening dependent, dimensionless constant.
E	Young's modulus of elasticity.
F	time-dependent modulus for mode I.
$f(n)$	strain hardening dependent constant for mode III at $\theta = \pi/4$.
G	shear modulus of elasticity.
$g(n)$	strain hardening dependent constant for mode III at $\theta = \pi/2$.
H	time-dependent modulus for mode III.
$h(n)$	strain hardening dependent function for mode III.
$h_1(n)$	strain hardening dependent function for mode I.
I_n	integration constant for mode I.
J	Rice's contour integral.
J_c	fracture resistance of the material.
K_I	mode I elastic stress-intensity factor.
K_{III}	mode III elastic stress-intensity factor.
K_c	fracture toughness of the material.
ℓ	arc length.
m	strain hardening dependent constant.
n	strain hardening exponent for time-independent deformation.
n	creep exponent for time-dependent deformation.
$\vec{n}$	outward normal vector.
N	number of loading cycles.
N_f	number of loading cycles required for failure.
N_i	number of loading cycles required for the onset of crack growth.
p, q	stress function arbitrary constants.

R	radius of the zone of dominance of the HRR field.
R_1	characteristic radius of the fracture process zone.
R_{max}	maximum size of approximate plastic zone for mode I under plane strain conditions.
$R(0)$	approximate distance to elastic-plastic boundary ahead of the tip of a crack loaded in mode I under plane strain conditions.
$R(\pi)$	approximate distance to elastic-plastic boundary behind the tip of a crack loaded in mode I under plane strain conditions.
r	polar distance measured from the crack-tip.
r_1	radius of a region described by elastic singularity around crack-tip.
r_2	radius of a region described by HRR singularity around crack-tip.
s	effective stress.
s_e	effective von Mises equivalent stress.
s_{ij}	effective deviatoric stress tensor.
s_0	effective yield stress of the material.
t	time.
t_f	elapsed time required for failure.
t_i	elapsed time required for the onset of crack growth.
t_R	theoretical instability time.
t_2	time required to double the initial crack length.
$\mathbf{T}$	traction vector.
$\mathbf{u}$	in-plane displacement vector.
$\dot{\mathbf{u}}$	in-plane displacement rate.
w	anti-plane displacement.
$\dot{w}$	anti-plane displacement rate.
W	width of a structural strip subject to in-plane loading.
W_e	elastic strain energy.
x,y,z	cartesian coordinates.
β	damage parameter for time-dependent deformation.
Γ	counter clockwise contour around the crack-tip.
γ	shear strain.
γ_0	yield strain in shear.
δ_{ij}	Kronecker delta, $\delta_{ij}= 1$ if $i=j$ and $\delta_{ij}= 0$ if $i\neq j$.
δ_t	crack-tip opening displacement, CTOD.
$\zeta(n)$	strain hardening dependent constant for mode I at $\theta = \pi/2$.
η	damage parameter for cyclic loading.
θ	angle measured from the crack-tip.
κ	material constant independent of stress and time.
λ	damage parameter for time-independent deformation under constant load.
ν	Poisson's ratio of elastic contraction.
$\xi(n)$	strain hardening dependent constant for mode I at $\theta = \pi/4$.
σ_{ij}	stress tensor.

σ_e von Mises equivalent stress.
σ_0 yield stress in tension.
σ_∞ remotely applied in-plane tensile stress.
ς_{ij} deviatoric stress tensor.
τ shear stress.
τ_0 yield stress in shear.
τ_∞ remotely applied anti-plane shear stress.
ϕ the angle between the y-direction and the principal shear direction measured positive counterclockwise (Figure 2.1).
ψ scalar potential function for anti-plane deformation.
Ω continuity function of damage.
ω Airy stress function.
ε_{ij} strain tensor.
$\dot{\varepsilon}_{ij}$ rate of strain tensor.
ε_0 yield strain in tension.
ϑ material constant independent of stress and time.
$\varkappa$ amplitude of Airy stress function.
$\varpi(\theta)$ dimensionless angular function of θ.
$\hat{\alpha}(\theta)$ dimensionless angular variation of the von Mises equivalent stress.
$\hat{\upsilon}_r(\theta)$ radial dimensionless angular displacement function.
$\hat{\upsilon}_\theta(\theta)$ tangential dimensionless angular displacement function.

1 INTRODUCTION

The success of any structural component design depends on an appropriate selection of a specific material with respect to its mechanical and physical properties. Until very recently, the only material properties of any interest were the elastic properties. The wide safety margins inherent to this design philosophy (when applied to ductile materials) effectively discouraged inquiries into the true behavior of solids, relegating the research into the inelastic material theories to the more rarefied atmosphere of the academic world. However, the ever increasing demands placed by modern industry on materials, which more and more frequently have to cope with severe thermal and chemical environments, coupled with the emphasis on economy (reflecting the diminishing resources) present a strong incentive to re-examine the general philosophies of design.

The initial effort in unfolding the mysteries of the nonlinear behavior of solids was mostly developed within the framework of the classical theory of plasticity. However, phenomena such as: softening (negative slope of the stress-strain curve), positive dilatancy (volumetric strain), and the gradual change of the elastic modulus in subsequent cycles of loading can not be satisfactorily interpreted within the framework of the plasticity theory. Hence, there is a need for a theory which will recognize the difference between a plastic flow and microcracking. To this end, it appears reasonable to introduce the damage experienced by structural components due to the accumulation of microvoids and investigate their failure within this framework. This dissertation addresses the interaction between a macroscopic crack and microvoids ahead of its tip. Elastic-plastic solutions of the deformation theory of

plasticity are used in conjunction with continuum damage mechanics to model fracture of work-hardening materials.

1.1 Historical Background

Since man began to design structures, fracture has been studied as a "yes or no" process related to a critical value of load, stress, strain, and time or number of cycles of loading. To analyze or predict the failure of a structural component is one of the main goals of engineering science. Consequently, fracture mechanics became one of its leading branches. Fracture mechanics is based on the analysis of existing cracks. However, especially under conditions of cyclic loading, this might be too late to prevent failure. Therefore, the question regarding the precursory state, that is, the evolution of internal damage before macrocracks become visible, was then posed. In the first half of this century, many attempts were made to develop a variable related to the progressive deterioration prior to failure. One of the successful approaches to the problem was Weibull's theory (see for example Bolotin [1] and Cherepanov [2]) which examined, in a statistical manner, the "weakest link" in the material volume under consideration. Unfortunately, it proved too difficult mathematically to be applied to structural components. It was not until 1958, when L. M. Kachanov published the first Paper [3] on a field variable, Ω, called "continuity" to describe the damage process. About fifteen years later, a scalar damage variable, $D = (1-\Omega)$, which represents the fraction of the original cross-sectional area occupied by voids, received the status of an internal state variable in the thermodynamical sense, where, $0 \leq D \leq 1$ (0 for the undamaged state and 1

for failure).

During these fifteen years, this concept was practically ignored and only one important result appeared, in 1968, with the concept of effective stress introduced by Y. N. Rabotnov [4]. In his original paper, Kachanov [3] did not specify the physical meaning of the damage. Rather, he introduced its complement $\Omega = 1\text{-}D$, which as previously mentioned, he called continuity. Rabotnov proposed that the cross-sectional area available for the transfer of loads is a meaningful measure of the recorded history of loading. The basic development of damage mechanics occurred during the 1970s, at least twenty years after the tremendous development of fracture mechanics. Damage mechanics can be defined as the branch of continuum mechanics that studies, through the introduction of mechanical variables, the mechanisms involved in the material deterioration when they are subjected to loading. At the microscale level, the damage of the material occurs due to the accumulation of microstresses in the neighborhood of defects and also the breaking of bonds which create voids and cracks. At the macroscale level, this manifests itself in the growth of a crack. While the theory itself can be traced back to its progenitor, L. M. Kachanov [3], the name "continuum damage mechanics" was , according to Krajcinovic [5], coined by Janson and Hult [6] in 1977. The damage concept and its applications to predict the behavior of structures have been expanded in the works of Lemaitre and Chaboche [7], Leckie and Hayhurst [8], Hult [9], Broberg [10] and others.

Many investigators suggested further modifications to the scalar damage model, including tensorial representation of damage. However, the scalar representation is more appropriate to characterize the damage experienced by ductile materials in form of a sufficiently dilute

concentration of spheroidal voids (Krajcinovic [11]).

In the past few decades, and in an effort to unlock the enigma of fracture mechanics, many works have been developed to investigate the asymptotic solutions of stationary crack-tip elasto-plastic fields. For power-law hardening materials, Hutchinson [12] and Rice and Rosengren [13], independently, developed the well-known HRR solution for mode I crack-tip singularity field under plane strain and plane stress conditions. The amplitude of the HRR singularity field is given by the path-independent J-integral discovered by Rice [14] and Eshelby [15]. The J-integral provides the theoretical basis for non-linear fracture mechanics. This pioneering work established the corner stone of the current applications of fracture mechanics to analyze and predict failures in structural components. Rice [14] was able to generalize the energy release rate to nonlinear materials by idealizing plastic deformation as nonlinear elasticity. He showed that the nonlinear energy release rate can be expressed as a line integral, which he called J-integral, evaluated along an arbitrary contour around the crack. In 1971, Begley and Landes [16] characterized fracture toughness of nuclear pressure vessel steels with the J-integral. Their experimental work was a break-through and led to the publication of a standard procedure for J-testing as a measure of fracture toughness of metals [17]. In 1976, Shih and Hutchinson [18], introduced the theoretical framework for the mathematical relationship between toughness, stress, and crack size based on the J-integral. Using their methodology, the Electric Power Research Institute (EPRI) published a fracture design handbook [19] for the analysis of elastic-plastic fracture. Shih [20] devised a relationship between the J-integral and crack-tip opening displacement (CTOD). This relationship confirms that both the J-integral and CTOD are equally valid

characterizing parameters for fracture. To this end, it is worth mentioning that in 1971, in Britain, Burdekin and Dawes [21] applied the ideas suggested by Wells [22] several years earlier and developed the CTOD design curve, a semi-empirical fracture mechanics methodology for welded steel structures. The British nuclear power industry developed their own fracture design analysis [23] based on the strip yield model of Dugdale [24] and Barenblatt [25].

On the other hand, only in the last two decades, continuum damage mechanics has been extended to investigate the fracture associated with damage. The earliest attempt at applying the continuum damage mechanics theory in conjunction with fracture mechanics for a well-developed crack was considered, in 1977, by Janson and Hult [6]. In 1978, the interaction between existing cracks and microvoids was explored by Janson [26,27] who studied an idealized Dugdale model with continuous damage formation for a crack under mode I, subjected to cyclic tensile loading and time-dependent deformation. Alam and Kassir [28] studied a plastic strip model for an axisymmetric penny shaped crack with damage accumulation, under mode I conditions. However, none of the aforementioned works uses elastic-plastic solutions to investigate the interaction between a macrocrack and the damaged material near the crack-tip.

1.2 Objective of Dissertation

It is now generally agreed that both localized macroscopic defects (major cracks) and distributed microscopic defects (damage) have significant influence on the failure of materials. Conventional fracture mechanics deals only with the influence of a major crack in a defect free continuum. Damage mechanics deals with the collective effect of distributed defects without a major crack. However, in real situations, both a major crack and microscopic damage may exist simultaneously, especially in the neighborhood of a crack-tip. So the interaction between the major crack and microscopic damage need to be considered. Therefore, a realistic and convenient way of achieving this would be the introduction into the constitutive equations of a homogeneous continuum scalar damage variable, and the resulting stress-strain field near the crack-tip should dictate the instability and growth of the crack. In conventional fracture mechanics, the critical value of the stress-intensity factor, K_c, is used as a measure of fracture toughness in linear elastic analysis. Fracture in the plastic domain is characterized by the fracture resistance, J_c, of the material. However, in this dissertation, the fracture criteria required for the onset of crack extension, fatigue crack propagation, and time-dependent crack growth are based on the evolution of a scalar damage variable, D, coupled with the opening displacement obtained for elastic-plastic solutions of a cracked body.

Extensive experiments [29,30,31] have shown that ductile fracture in metals involves considerable damage via the nucleation, growth and coalescence of microvoids or microcracks. The material ahead of the crack-tip deforms intensely and a "damage-zone" will form in which microvoids or microcracks are usually nucleated by cracking and then

grow with increase of deformation. Consequently, the crack propagates by the coalescence of the voids. This process will continue until the final failure. Apparently, the constitutive behavior of the material near the crack-tip is different from the original virgin material due to the anticipation of distributed damage. So, this coupling behavior should be taken into account in the analysis of the crack-tip deformation and damage fields, which in turn have fundamental importance in describing fracture. To the author's best knowledge, only a few of these works have been carried out so far.

This dissertation investigates crack-tip fields of deformation and damage for a power-law hardening material containing cracks subjected to mode I and mode III loading conditions. Because of mathematical simplicities, and in order to establish basic characteristics of the model, a crack subjected to longitudinal shear loading (mode III) is first investigated. Second, the deformation and damage fields for a crack subjected to tensile loading (mode I) are investigated using the HRR singularity fields. A scalar damage variable, D, which represents the fraction of the original cross-sectional area occupied by voids, is introduced to describe the mechanical effect of distributed microscopic damage ahead of the tip of a macroscopic crack, a postulation substantiated by an assumed ductile behavior of the material of the components. Due to the elevated strains ahead of the crack-tip, the damage field is envisaged to be concentrated in the plastic zone, which will also be called the damage-zone throughout the dissertation. Any damage outside the damage-zone is considered small and negligible. Inside the damage-zone, damage is assumed to vary linearly with the crack opening displacement.

1.3 Organization of Dissertation

This dissertation is organized into 8 Chapters including this introduction. Cracks subjected to anti-plane shear loading (mode III) are dealt with in Chapter 2 through Chapter 4. The remaining part, Chapters 5 and 6, investigate cracks subjected to in-plane tensile loading (mode I). A brief description of the content of each Chapter is as follows: Chapter 2 is devoted to the determination of damage field for a crack subjected to anti-plane shear loading (mode III). A hodograph transformation is employed to linearize the non-linear governing differential equation and derive a closed form expression for the displacement and the size of a circular damage-zone, engulfing the crack-tip. The conditions necessary for the onset of crack instability in the small-scale yielding and fully-plastic solutions are investigated. The remotely applied stress, τ_∞, is found to be proportional to $a_0^{-1/(n+1)}$, where a_0 is the original crack length and n is the strain hardening exponent of the material. This result reduces to Griffith classical result, obtained by energy criterion [32], for elastic material (n=1). Fatigue crack propagation due to cyclic loading is also considered, with attention focused on the small-scale yielding solution. In Chapter 3, numerical results and discussion of the influence of strain hardening and material parameters on the onset of crack instability and fatigue crack growth are presented and graphically exhibited. An insignificant dependence of the strain hardening exponent on the crack instability criterion is observed in the small-scale yielding range while somewhat appreciable dependence is shown for the fully-plastic solution. Extensive numerical results of fatigue crack propagation are then presented to reveal the influence of the strain hardening exponent and material parameters on the relationship between the number of load cycles and crack length required for failure.

Chapter 4 describes the time-dependent damage field for a crack subjected to mode III loading under steady-state creep conditions. A brief summary of the basic mathematical equations required for the analysis of steady-state creep is presented, and the criterion for creep crack growth under constant load is then developed. Numerical analysis is performed and the elapsed time required for the onset of crack growth and the elapsed time required for failure are determined and graphically exhibited for different combination of material parameters. The theoretical time of rupture, which is basically a creep phenomenon, is determined and found to envelope all other time curves. It is also found that the theoretical time curve demonstrates an asymptotic slope of $-1/\hat{n}$ when $t_R \rightarrow \infty$, where $\hat{n}$ is a material constant that is independent of stress and time and t_R is the theoretical time.

Chapter 5 investigates the damage field for a crack subjected to tensile loading (mode I). Similar to the HRR solution, the formulation of the governing equations of a damaged material and the derivation of the asymptotic leading term for the displacements are presented. Guided by the results obtained in Chapter 2, a circular damage-zone, centered at the crack-tip is postulated. Then, a criterion for the onset of crack instability for the small-scale yielding and fully-plastic solutions is developed. The remotely applied stress, σ_∞, is found (as expected) to be proportional to $a_0^{-1/(n+1)}$. It is clear that this also reduces to Griffith's classical result for elastic material (n=1). This confirms the well-known observation that the characteristics of the anti-plane mode are similar to those of the opening mode. Another noteworthy feature of the onset of crack instability criterion, for mode I, is its dependence on Poisson's ratio. Fatigue crack propagation under cyclic loading and time-dependent crack propagation under steady-state creep conditions, are also investigated.

Chapter 6 is concerned with numerical results and discussion of the influence of the strain hardening, creep exponent, and material parameters on the criteria developed earlier. The influence of Poisson's ratio on the crack instability criterion is explored. For highly ductile material, the crack length required to cause instability is found to be higher than that required for materials with lower value of Poisson's ratio. As expected, in the criterion for fatigue crack propagation , the number of cycles required for failure increases with decreased values of the applied loads. The variations of the normalized crack length with the number of cycles required for failure are shown graphically. For creep crack growth, a reduction in the elapsed time required to cause failure is observed for higher values of the applied stress. Similar to the anti-plane mode, the theoretical time curve exhibits an asymptotic slope of $-1/\delta$ when $t_R \rightarrow \infty$. For given material parameters, rates of crack growth are graphically exhibited. Finally, the dissertation concludes by summarizing the contribution of this research in Chapter 7 and recommending extensions for future research in Chapter 8.

2 DAMAGE FIELD FOR A CRACK SUBJECTED TO ANTI-PLANE SHEAR LOADING (MODE III)

2.1 Introduction

The damage field near the tip of a stationary crack subjected to anti-plane shear loading is investigated in this Chapter. A material with a power hardening stress-strain relationship is considered. The strain concentration near the crack-tip leads to nucleation, growth, and coalescence of microcracks or microvoids in the material. Consequently, the constitutive behavior of the material near the crack-tip becomes different from that of the material far away from the crack-tip. A damage variable, which represents the fraction of the original cross-sectional area occupied by voids, is introduced to describe the mechanical effect of distributed microscopic damage. The constitutive equations coupled with damage and appropriate boundary conditions are used to derive the governing equations. Since the governing differential equation for the normal displacement is non-linear, a hodograph transformation technique is employed to linearize the problem and determine a closed form expression for the displacement.

Section 2.2 contains a brief summary of the basic mathematical equations required for the analysis. In section 2.3, a circular damage-zone is determined engulfing the crack-tip. Section 2.4 describes the conditions necessary for the onset of crack instability . A critical stress is determined as a function of crack length and a material parameter. The remotely applied stress, τ_{∞}, is found to be proportional to $a_0^{-1/(n+1)}$ and for n=1, this result reduces to Griffith classical result. Section 2.5 deals with fatigue crack propagation under cyclic

loading. For given material parameters, the number of load cycles required for the onset of crack propagation, N_i, and the number of cycles required to failure, N_f, are determined and shown graphically.

2.2 Summary of Basic Equations

Consider a semi-infinite body occupying the region $x \geq -a_0$, $-\infty < y, z < \infty$ as shown in Figure 2.1. In terms of the usual cartesian coordinates (x,y,z), centered at the crack-tip, the body is subjected to remotely applied shearing stress, $\tau_{yz} = \tau_\infty$. By symmetry, this problem is equivalent to the problem of an infinite body with a crack of length $2a_0$ subjected to the same loading. The nonvanishing displacement component is the z-component w(x,y). Consequently, the shearing strains ($\gamma_{xz} = \partial w/\partial x$ and $\gamma_{yz} = \partial w/\partial y$) and the corresponding stresses (τ_{xz} and τ_{yz}) must satisfy the compatibility and equilibrium equations:

$$\partial \gamma_{xz}/\partial y = \partial \gamma_{yz}/\partial x \tag{2.1}$$

$$\partial \tau_{xz}/\partial x + \partial \tau_{yz}/\partial y = 0. \tag{2.2}$$

The principal anti-plane shear stress and engineering strain which are given by:

$$\tau = (\tau_{xz}^2 + \tau_{yz}^2)^{1/2}, \quad \gamma = (\gamma_{xz}^2 + \gamma_{yz}^2)^{1/2} \tag{2.3}$$

obey a linear law to the reference point (τ_0, γ_0) and thereafter a power hardening relation given by:

$$\gamma/\gamma_0 = (\tau/\tau_0)^n \tag{2.4}$$

where, $\tau_0 = G\gamma_0$, with G being the elastic shear modulus and n is the power hardening exponent. The Hencky stress-strain relations take the form:

$$\gamma_{xz}/\gamma = \tau_{xz}/\tau \text{ and } \gamma_{yz}/\gamma = \tau_{yz}/\tau \tag{2.5}$$

Equations (2.1) through (2.5) need to be solved subject to the appropriate boundary conditions, namely, the crack faces are stress free, specified loading at the remote boundary, and the stress and strain distributions become elastic at the elastic-plastic boundary at some distance from the crack region.

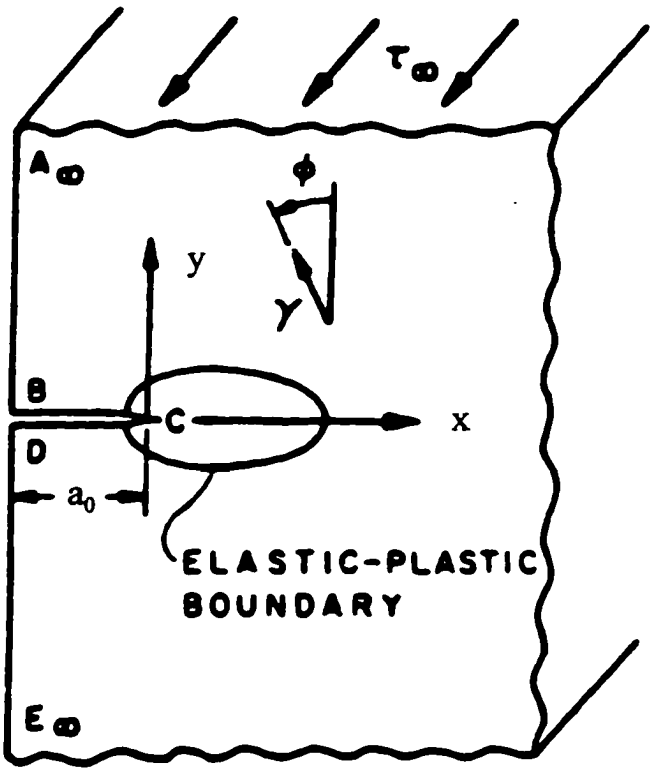

Figure 2.1 Edge crack physical plane.

It is clear from equations (2.4)-(2.5) and the strain displacement relations that the governing differential equation for w is nonlinear. However, the problem can be reduced to a linear problem by the hodograph transformation.

In this transformation, the roles of the dependent variables (γ_{xz},γ_{yz}) and the independent variables (x,y) are interchanged using implicit function theory. The hodograph transformation was first used by Rice [33] to obtain a perturbation solution of the anti-plane problem for elastic-plastic materials. Earlier, Neuber [34] used a stress hodograph plane to analyze the double-notched problem. Similar techniques are employed in fluid mechanics which reduce the nonlinear equations of two dimensional compressible flow to linear equations in terms of velocity components [35]. The transformation which is performed by regarding the physical coordinates as functions of the strains, namely, $x = x(\gamma_{xz},\gamma_{yz})$ and $y = y(\gamma_{xz},\gamma_{yz})$, maps the physical plane shown in Figure 2.1 onto the strain or hodograph plane shown in Figure 2.2. It is readily shown that the compatibility equation reduces to:

$$\partial x/\partial\gamma_{yz} = \partial y/\partial\gamma_{xz} \tag{2.6}$$

while the equilibrium equation becomes:

$$\partial x/\partial\tau_{xz} + \partial y/\partial\tau_{yz} = 0. \tag{2.7}$$

The compatibility equation (2.6) implies the existence of a scalar potential function, $\psi = \psi(\gamma,\phi)$, such that the physical coordinates are related to the derivatives of the potential function by:

$$x = -\sin\phi\,(\partial\psi/\partial\gamma) - \cos\phi\,(\partial\psi/\partial\phi)\,/\,\gamma \tag{2.8a}$$

$$y = \cos\phi\,(\partial\psi/\partial\gamma) - \sin\phi\,(\partial\psi/\partial\phi)\,/\,\gamma \tag{2.8b}$$

In equations (2.8), ϕ is the angle between the y-direction and the principal shear direction,

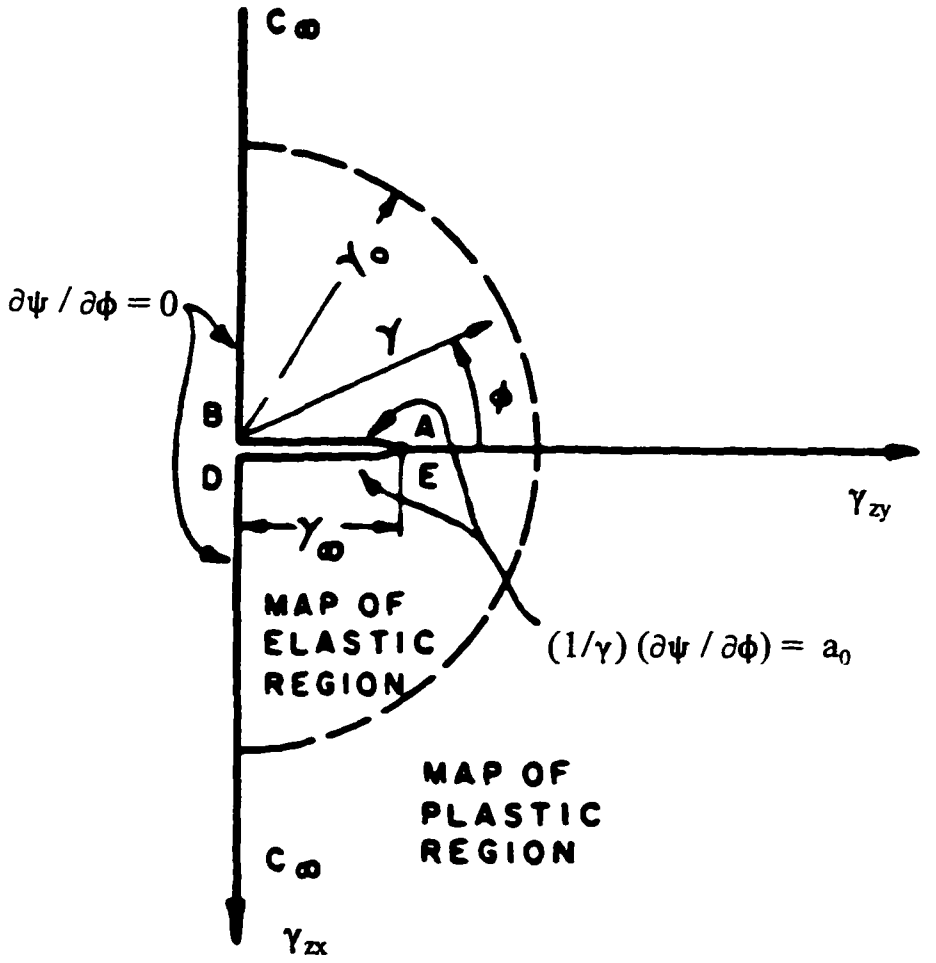

Figure 2.2 Map of physical plane into strain plane [33].

measured positive counterclockwise (see Figures 2.1 and 2.2).

It has been established in reference [33] that the potential function, $\psi(\gamma,\phi)$, satisfies the differential equation:

$$[\tau(\gamma)/\gamma\tau'(\gamma)]\,(\partial^2\psi/\partial\gamma^2) + (1/\gamma)\,(\partial\psi/\partial\gamma) + (1/\gamma^2)\,(\partial^2\psi/\partial\phi^2) = 0. \qquad (2.9)$$

where, $\tau'(\gamma)$ stands for $d\tau(\gamma)/d\gamma$. Moreover, the expression for the displacement, w, in terms of the potential function, ψ, is obtained from the Legendre transformation:

$$w(\gamma,\phi) = \gamma\,(\partial\psi/\partial\gamma) - \psi \qquad (2.10)$$

In this manner, the problem is reduced to a partial differential equation in the hodograph plane which must be satisfied by the potential function $\psi(\gamma,\phi)$ subject to appropriate boundary conditions. Since $y = 0$ on the crack surfaces, equation (2.8b) requires $\partial\psi/\partial\phi = 0$ at $\phi = \pm\,\pi/2$. The crack-tip point in the physical plane is mapped into points at infinity in the strain plane, and thus the derivatives of ψ must vanish at infinity, since $x = y = 0$ at the crack-tip. Therefore, at the elastic-plastic boundary, $(\partial\psi/\partial\gamma)$ and $(1/\gamma)\,(\partial\psi/\partial\phi)$ approach zero. The strain plane in Figure 2.2 shows the map of the physical plane and the aforementioned boundary conditions.

In the next section, the potential function, $\psi(\gamma,\phi)$, coupled with continuum damage mechanics, are used to obtain a solution of the governing equation (2.9) and the expression for the displacement follows from equation (2.10).

2.3 Determination of Damage-Zone

In this section, the concept of continuum damage mechanics coupled with the basic equations of the previous section are used to determine the extent of the damage zone ahead of the crack-tip using small-scale yielding solution.

Continuum damage mechanics deals with the load carrying capacity of solids due to the presence of microscopic defects such as microcracks or voids. The theory was originally conceived by Kachanov [3] and Rabotnov [4]. This concept has been further extended by Lemaitre [36], Lemaitre and Chaboche [37], and Hayhurst and Leckie [38] and others. Because of the elevated strain ahead of the crack-tip, the damage field is envisaged to be concentrated in the plastic zone in the vicinity of the crack-tip, and any damage outside the plastic zone is considered small and may be neglected.

The nominal shear stress, τ, is related to the effective (or net) shear stress, s, by the relationship:

$$\tau = s(1 - D) = \Omega\, s \tag{2.11}$$

where Ω is the continuity function and D is a scalar damage parameter, defined as:

$$D = A_{void} / A = 1 - (A_{net} / A) \tag{2.12}$$

where A and A_{net} are the macroscopically observable original and net cross-sectional areas, respectively. A_{void} is the fraction of cross-sectional area occupied by voids.

The damage accumulation and growth are determined by the effective stress in the damage-zone near the crack-tip. Within the zone, the effective (net) stress, s, equals the effective (net) yield stress, s_0. In this dissertation, the following damage hypothesis is used: Inside the zone, damage varies linearly with the crack opening displacement, i.e.

$$D = \lambda \cdot w \tag{2.13}$$

where λ is a damage parameter denoting a fraction of the crack opening displacement in the damaged material, and w is the anti-plane displacement determined from equation (2.10). In order to derive the expression of w in the damage-zone, Lemaitre's strain equivalence principle [39] which states that "any strain constitutive equation for a damaged material may be derived in the same way as for a virgin material except that the usual stress is replaced by the effective stress" is used. Introducing this principle into equation (2.4), the constitutive relation for an isotropic material with isotropic damage may be expressed as:

$$\gamma/\gamma_0 = (s/s_0)^n \quad , \gamma > \gamma_0 \tag{2.14}$$

To obtain the extent of the damage zone near the crack-tip, a solution, $\psi(\gamma,\phi)$, of the governing partial differential equation (2.9), defined in the interval $\gamma \in [0,\infty]$ and $\phi \in [-\pi/2 , \pi/2]$, is needed. Assuming a solution for ψ in the form of $\sin\phi$ times a function of γ, the boundary conditions on the crack surfaces in the strain plane are automatically satisfied, and the problem reduces to determining $\psi(\gamma)$ so that the differential equation (2.9) and the remaining boundary conditions at the origin and at elastic-plastic boundary are satisfied. It has been shown in reference [33] that for small-scale yielding:

$$\psi = (-K_{III}^2 \gamma_0 / \pi \tau_0) \{ \gamma \int_\gamma^\infty [du / (u^2 \tau(u))] \} \sin\phi \quad , \gamma > \gamma_0 \tag{2.15a}$$

$$\psi = (-K_{III}^2 \gamma_0^2 / 2\pi\tau_0^2) \{(1/\gamma) + (\gamma/\gamma_0^2) \cdot (2\gamma_0\tau_0 \int_{\tau_0}^\infty [du / (u^2 \tau(u))] - 1)\} \sin\phi \quad , \gamma < \gamma_0 \tag{2.15b}$$

where K_{III} is the elastic stress-intensity factor for mode III.

Substituting equation (2.11) in equation (2.15a) yields:

$$\psi = (- K_{III}^2 \gamma_0 / \pi \Omega s_0)\{\gamma \int_{\gamma}^{\infty} [1 / (u^2 \Omega s(u))]du \} \sin\phi \quad , \gamma > \gamma_0 \qquad (2.16)$$

The derivatives of the potential function, ψ, with respect to γ and ϕ, respectively, are:

$$\partial\psi/\partial\phi = (- K_{III}^2 \gamma_0 / \pi \Omega s_0) \{ \gamma \int_{\gamma}^{\infty} [1 / (u^2 \Omega s(u))]du \} \cos\phi \qquad (2.17)$$

$$\partial\psi/\partial\gamma = (- K_{III}^2 \gamma_0 / \pi \Omega s_0) \{ \int_{\gamma}^{\infty} [1 / (u^2 \Omega s(u))]du + [1 / (\gamma \Omega s(\gamma))]\} \sin\phi \qquad (2.18)$$

Equations (2.8) when combined with equations (2.17) and (2.18) yield:

$$x=(K_{III}^2\gamma_0/(2\pi\Omega s_0))\{(2\int_{\gamma}^{\infty}[1/(u^2\Omega s(u))]du-[1/(\gamma\Omega s(\gamma))] +(\cos2\phi / [1/(\gamma\Omega s(\gamma))])\} \qquad (0<\gamma<\infty, -\pi/2\le\phi\le\pi/2) \qquad (2.19a)$$

$$y = (K_{III}^2\gamma_0/(2\pi\Omega s_0)) (\sin2\phi / [1/(\gamma\Omega s(\gamma))]) \qquad (2.19b)$$

Subtracting the term independent of ϕ from equation (2.19a), squaring both x and y and adding, the equations of lines in the plastic region along which the strain has the constant magnitude γ are circles:

$$[x - X(\gamma)]^2 + y^2 = [R(\gamma)]^2 \qquad (2.20)$$

centered ahead of the crack-tip at the distance:

$$X(\gamma) = (K_{III}^2\gamma_0/(2\pi\Omega s_0))(2\int_{\gamma}^{\infty}[1/(u^2\Omega s(u))]du-[1/(\gamma\Omega s(\gamma))]) \qquad (2.21)$$

and with radius:

$$R(\gamma) = (K_{III}^2\gamma_0/(2\pi\Omega s_0))(1/(\gamma\Omega s(\gamma))) \qquad (2.22)$$

Now, the solution is particularized to the power-hardening law described by equation (2.14). The integral appearing in equations (2.16) and (2.21) can be evaluated as:

$$\int_{\gamma}^{\infty}[1/(u^2\Omega s(u))]du = [n / (n+1)] [1/(\gamma\Omega s(\gamma))] \qquad (2.23)$$

Also, the parameters $X(\gamma)$, $R(\gamma)$ describing the geometry of the plastic region become (see

Figure 2.3):

$$X(\gamma) = [(n-1) / (n+1)]\ [K_{III}^2/(2\pi(\Omega s_0)^2)]\ (\gamma_0/\gamma)^{(n+1)/n} \quad (2.24a)$$

$$R(\gamma) = [K_{III}^2/(2\pi(\Omega s_0)^2)]\ (\gamma_0/\gamma)^{(n+1)/n} \quad (2.24b)$$

It is apparent from Figure 2.3, in terms of polar coordinates (r, θ) centered at the crack-tip, that:

$$r = R(\gamma)\ (\sin 2\phi / \sin\theta) \quad (2.25)$$

It then follows from equations (2.24b) and (2.25) that:

$$\gamma = \gamma_0[K_{III}^2 \sin 2\phi/2\pi(\Omega s_0)^2 r \sin\theta]^{n/(n+1)} \quad , \gamma > \gamma_0 \quad (2.26)$$

which indicates that the strain has a $r^{-n/(n+1)}$ singularity at the crack-tip.

Utilizing equations (2.24), it may be readily shown that the circular plastic zone extends a distance:

$$R(\gamma_0) + X(\gamma_0) = [n / (n+1)][K_{III}^2/(\pi(\Omega s_0)^2)] \quad (2.27)$$

ahead of the crack-tip and a distance:

$$R(\gamma_0) - X(\gamma_0) = [1 / (n+1)][K_{III}^2/(\pi(\Omega s_0)^2)] \quad (2.28)$$

behind the crack-tip. Substituting for the integral from equation (2.23) into equation (2.16), the potential function, ψ, can be written as:

$$\psi = [-K_{III}^2\gamma_0(\gamma_0)^{1/n} / (\pi(\Omega s_0)^2)]\ [n / (n+1)]\ (1/\gamma)^{1/n} \sin\phi \quad (2.29)$$

and it follows that:

$$\partial\psi/\partial\gamma = [K_{III}^2\gamma_0(\gamma_0)^{1/n} / (\pi(\Omega s_0)^2)]\ [1 / (n+1)]\ (1/\gamma)^{(n+1)/n} \sin\phi \quad (2.30)$$

Substituting equations (2.29) and (2.30) in equation (2.10), the expression for anti-plane

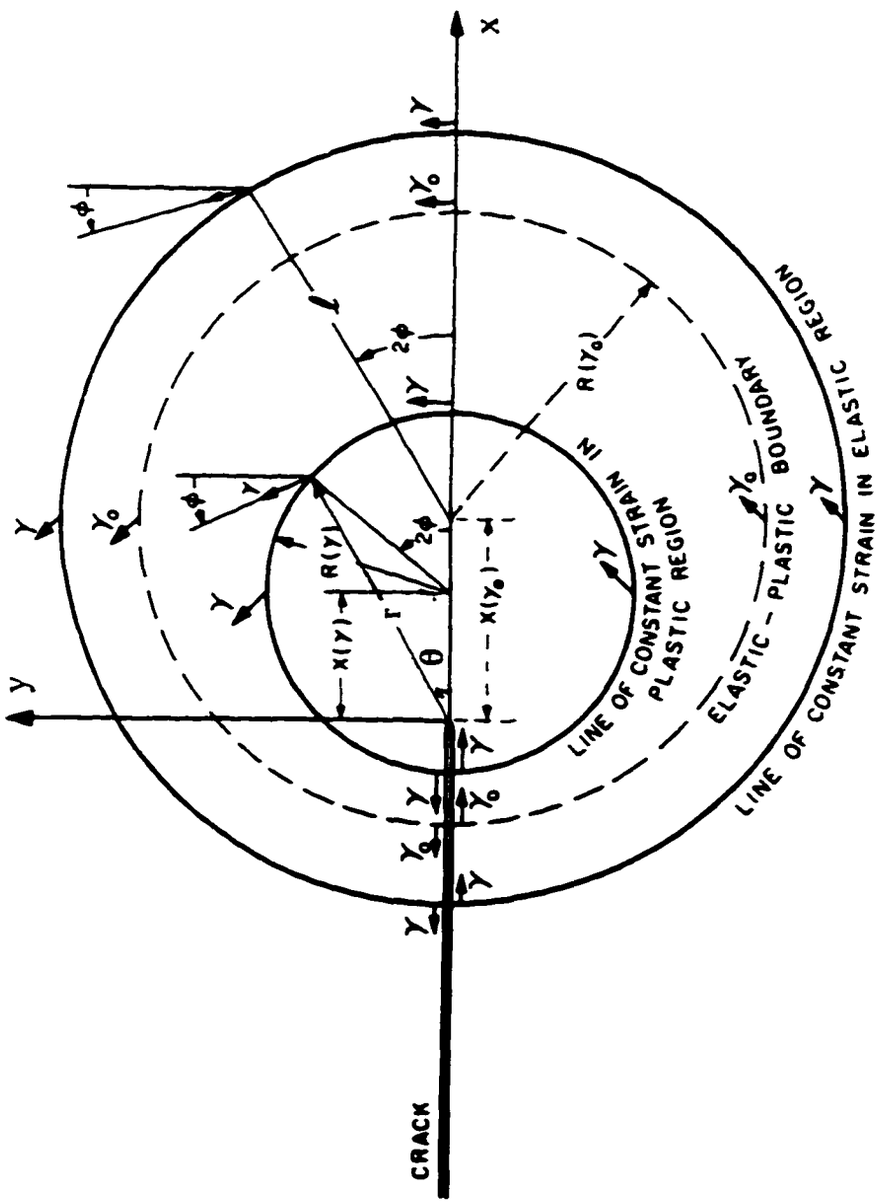

Figure 2.3 Geometry of small-scale yielding solution for anti-plane straining of a work-hardening elastic-plastic material [33].

displacement $w(\gamma, \phi)$ is obtained as:

$$w(\gamma,\phi) = [K_{III}^2 \gamma_0 (\gamma_0)^{1/n} / (\pi(\Omega s_0)^2)] (\gamma)^{-1/n} \sin\phi \quad (2.31)$$

Combining equations (2.26) and (2.31), the anti-plane displacement, w, is finally expressed as:

$$w = [K_{III}^2 (\gamma_0) / (\pi(\Omega s_0)^2)] [K_{III}^2 \{h(\theta)/r\} / (\pi(\Omega s_0)^2)]^{-1/(n+1)} \sin\phi \quad (2.32)$$

where $h(\theta) = (\sin 2\phi / 2\sin\theta)$.

Note that for the small-scale yielding, the stress-intensity factor K_{III} is related to Rice's J-integral [33] by the relation $K_{III}^2 = 2GJ$.

In the sequel, the conditions required to describe the onset of crack instability and crack growth under cyclic loading, on the elastic-plastic boundary, are determined.

2.4 Criterion for Crack Instability

In this section, the concepts of continuum damage mechanics developed earlier are applied to the stress and displacement fields to determine the conditions required for the onset of crack instability. As mentioned earlier, the damage is confined to circles of critical strain within the plastic zone and any uniform damage induced outside the plastic region is neglected. Inside the zone, the continuity function, Ω, is assumed to take constant values. From equation (2.32), the anti-plane displacement, $w(r,\theta)$, expressed in terms of polar coordinates (r,θ) measured from the crack-tip, can be shown to take the following simple form on the elastic-plastic boundary (see Figure 2.3):

$$w(r,\theta) = [2\, J / (\pi \Omega^2 s_0)] \sin\phi \qquad (2.33)$$

where J is Rice's path-independent integral and $r/h(\theta) = 2\, R(\gamma_0)$.

Within the damage-zone, the principal shear stress is given in terms of the net yield stress:

$$\tau = s_0 [\, 1 - \lambda .w(r,\theta) \,] \qquad (2.34)$$

One way of obtaining an expression for the continuity function, Ω, is to equate the exact shear stress given by equation (2.34) to the approximate stress, $\Omega\, s_0$, at $(r, \pi/4)$. This yields:

$$(1- \Omega) = \lambda .[2\, J / (\pi \Omega^2 s_0)] \sin\phi \qquad (2.35)$$

Then;

$$\Omega^2 = \Omega^3 + \lambda .(2\, J / (\pi\, s_0))\, f(n) \qquad (2.36)$$

where,

$$f(n) = \{ [3n + 1 - (n^2 + 6n+1)^{1/2}]/ 4(n+1)\}^{1/2} \qquad (2.37)$$

The measure of damage, D, is computed from the crack-tip opening displacement, $2\, w(r, \pi/2)$, which yields:

$$D = \lambda .[2J / (\pi \Omega^2 s_0)] g(n) \quad (2.38)$$

where,

$$g(n) = 2. [n/(n+1)]^{1/2} \quad (2.39)$$

The criterion for the onset of crack instability is established by requiring $D(r,\pi/2)$ in equation (2.38) to approach unity and using equation (2.36) to eliminate the continuity function, Ω. The result is:

$$\lambda .(2 J / (\pi s_0)) = [1 - (f(n)/g(n))]^2 / g(n) \quad (2.40)$$

In the remaining part of this section, equation (2.40) is used to predict the onset of crack instability for external loading characterized by the small-scale yielding and the fully plastic solutions.

2.4.1 Small-Scale Yielding Solution

For small-scale yielding, the J-integral is replaced by the elastic stress-intensity factor, namely, $J = K_{III}^2 / 2G$, and equation (2.40) yields:

$$\lambda .[K_{III}^2/(\pi s_0 G)] = [1 - (f(n)/g(n))]^2 / g(n) \quad (2.41)$$

It follows that for a crack of length $2a_0$, in an infinite body subjected to stress τ_∞ at the remote boundary, where $K_{III}^2 = \tau_\infty^2 \pi a_0$, the following condition for the onset of crack instability is obtained:

$$(\lambda s_0 a_0 / G) (\tau_\infty/s_0)^2 = [1 - (f(n)/g(n))]^2 / g(n) \quad (2.42)$$

In order for small-scale yielding solution to be valid, (τ_∞/s_0) has to be less than about 0.5. It is clear that equation (2.42) confirms Griffith's classical result, namely, τ_∞ is proportional to $a_0^{-.5}$. The constant of proportionality in equation (2.42) is a material parameter.

2.4.2 Large-Scale Yielding Solution

The extension to large-scale yielding involves using the fully plastic solution for Rice's J-integral in equations (2.36) and (2.38). For large scale yielding, when the plastic zone reaches across the entire uncracked ligament, the plastic zone assumes an elongated shape. As demonstrated by Rice [33], the transition from the circular plastic zones of small-scale yielding to the highly elongated zones of large-scale yielding occurs at stress level of about $\tau_\infty/s_0 > 0.5$. However, in this dissertation, the damage is assumed confined to the plastic zone of the small-scale yielding solution. The fully plastic J for the damaged material can be obtained along the same lines developed by Amazigo [40]. For a crack of length, $2a_0$, in an infinite body subjected to a constant stress, τ_∞, at the remote boundary, it can be shown that:

$$J / s_0 = (s_0 a_0/G) (\tau_\infty/s_0)^{n+1} \Omega^{-n} h(n) \qquad (2.43)$$

where h(n) is a function of the strain hardening exponent [40], whose numerical values are given in Table 1.

Substituting equation (2.43) into equation (2.38) and setting the damage parameter, D, to unity, the following relation is reached:

$$\Omega = \{(2 \lambda /\pi) (s_0 a_0/G) (\tau_\infty/s_0)^{(n+1)} h(n) g(n)\}^{1/(n+2)} \qquad (2.44)$$

In addition equations (2.35) and (2.43) yield:

$$\Omega = 1 - (2 \lambda /[\pi \Omega^{(n+2)}]) (s_0 a_0/G) (\tau_\infty/s_0)^{n+1} h(n) g(n) \qquad (2.45)$$

Eliminating Ω from equations (2.44) and (2.45) results in:

$$(\lambda s_0 a_0/G) (\tau_\infty/s_0)^{n+1} = \{(2/\pi) h(n) g(n)\}^{-1} [1 - (f(n)/g(n))]^{(n+2)} \qquad (2.46)$$

Equation (2.46) is valid for values of τ_∞/s_0 in the range 0.5 to 1.0.

Table 2.1

Numerical Values of the function h(n) in equation (2.46)

n	h(n)
1	1
1.5	1.23
2	1.45
3	1.82
5	2.46
10	3.69
20	5.43
30	8.83
50	12.61
100	40.22

It is worth noting that equation (2.46) of the large-scale yielding reveals that the critical stress is proportional to $a_0^{-1/(n+1)}$, which reduces to Griffith's classical result for elastic material (n = 1).

Numerical evaluations of conditions (2.42) and (2.46) are carried out and discussed in Chapter 3.

2.5 Fatigue Crack Propagation

Fatigue crack propagation under cyclic loading is considered in this section. Attention is focused on the small-scale yielding solution. In each cycle, the structural component is subjected to a constant step function varying from 0 to τ_- and an instantaneous damage increment is accumulated in the circle of critical strain. Unloading from τ_- to 0 does not cause any damage. Within the elastic-plastic circle, the damage increment, ΔD, per each cycle of loading is proportional to the crack opening displacement, $w(r,\theta)$.

Denoting by $D(r, \pi/2)$, the damage at a point $(r, \pi/2)$ from the crack-tip, it follows that after N load cycles:

$$D(r, \pi/2; N) = D(r, \pi/2: N-1) + \eta . w(r, \pi/2; N) \quad (2.47)$$

where η is a damage parameter and $D(r, \pi/2 ; N)$ is a function of the continuity function, Ω. To obtain a value of the continuity function, Ω, the exact and the approximate principal stresses are set equal at $(r, \pi/4)$, i.e.

$$\Omega(N) = 1 - D(r, \pi/4 ; N) \quad (2.48)$$

where now $D(r, \pi/4 ; N)$ is given by:

$$D(r, \pi/4 ; N) = D(r, \pi/4 ;N-1) + \eta . w(r, \pi/4 ;N) \quad (2.49)$$

Combining equations (2.33), (2.48) and (2.49), one can write:

$$\Omega(N) = 1 - \eta (K_{III}^2 / (G\pi s_0)) f(n)\{[1/\Omega^2(N - 1)] + [1/\Omega^2(N)]\} \quad (2.50)$$

For N = 0, there is no damage and Ω=1, while corresponding to N = 1, there is instantaneous damage accumulated in the plastic zone, whereby, the extent of the damage-zone and the crack opening displacement in the damage-zone can be evaluated. The extent of damage-zone ahead of the crack-tip is obtained from equation (2.27) as:

$$C(N) = [n / (n+1)][K_{III}^2/(\pi(\Omega s_0)^2)] \quad (2.51)$$

For each cycle of loading, w(r, π/2), w(r, π/4), Ω(N) and C(N), are calculated using equations (2.33) and (2.48)-(2.51). Figure 2.4 depicts a description of the crack growth criterion, where D(r, θ; N) is shown versus r, the polar distance ahead of the crack-tip. As schematically indicated in Figure 2.4, for N=1 and N=2, where D(r, π/2;N) is less than unity, a(N) = a_0 , the initial crack length. Next, the number of cycles is increased by one and Ω(N) of the previous step is used to update w(r, π/2), w(r, π/4). By using equations (2.47)-(2.51), an iterative procedure is repeated until D(r, π/2;N) assumes a value slightly above one (1+), then the crack has grown during the actual cycle.

The new crack length, a_N, which is found from the condition:

$$D(a_N , N) = 1. \quad (2.52)$$

is incrementally computed from:

$$a_N = a_0 + da_N \quad (2.53)$$

where:

$$da_N = [1 - \{1/ D(r, \pi/2;N)\}] \; C(N) \quad (2.54)$$

Using the new crack length given by equations (2.53) and (2.54), the iterative process can be repeated to obtain the final values of a(N), C(N), w(r, θ ;N), D(r, θ ;N) and Ω(N) at which instability is reached, i.e., the critical crack length to cause crack propagation is reached. Numerical calculations have been carried out and the influence of strain hardening and material parameters on the variations of load cycles with the critical crack lengths are presented in Chapter 3.

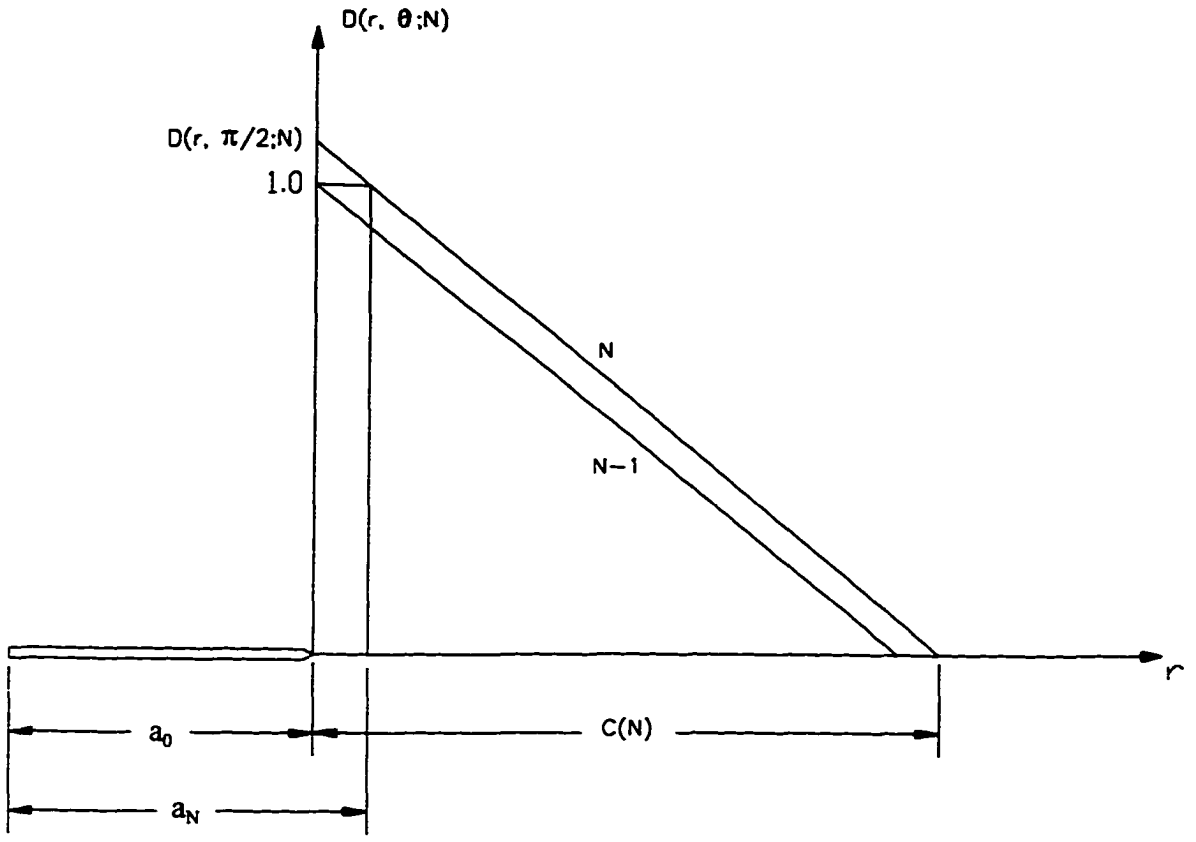

Figure 2.4 Description of fatigue crack growth criterion.

3 MODE III NUMERICAL RESULTS AND DISCUSSION

3.1 Introduction

In Chapter 2, a circular damage zone engulfing the crack-tip was determined and used to establish the conditions of crack instability and crack growth under cyclic loading. This Chapter presents numerical results and discussion of the influence of strain hardening and material parameters on these criteria.

The numerical results are presented in two parts: First, the onset of crack instability for external loading characterized by the small-scale and the fully-plastic solutions are numerically evaluated and displayed graphically. Second, extensive numerical results of the fatigue crack growth are obtained, for the small-scale yielding solution, to reveal the influence of the strain hardening and material parameters on the relation between the number of load cycles and crack length required for failure.

3.2 Criterion for Crack Instability

The criterion for the onset of crack instability is given in equations (2.42) and (2.46). These equations are plotted in Figure 3.1 where the variation of the critical external stress, $\tau_{\_}/s_0$, with the material parameter ($\lambda s_0 a_0 /G$) is shown. When the critical state is reached, the crack will start to grow unstably. The crack instability is followed immediately by crack growth to failure. In order for small-scale yielding to be valid, $\tau_{\_}/s_0$ has to be less than 0.5. On the other hand, large-scale yielding prevails when $\tau_{\_}/s_0$ assumes values in the range 0.5 to 1. For the small-scale yielding solution, Figure 3.1 demonstrates a straight line relationship between ($\tau_{\_}/s_0$) and ($\lambda s_0 a_0 /G$), in which $\tau_{\_}$ is proportional to $a^{-0.5}$, which is Griffith's classical result obtained by energy criterion [32]. For the large-scale yielding solution, Figure 3.1 also reveals that the critical stress is proportional to $a_0^{-1/(n+1)}$, which reduces to Griffith's classical result for elastic material (n = 1).

It is clear from Figure 3.1 that the external load required to cause instability decreases with increasing the strain hardening exponent n. The curves also show, relatively, little dependence on the hardening exponent in the small-scale yielding solution. This little dependence may be attributed to the fact that the J-integral is independent on hardening for small-scale yielding solution. However, somewhat appreciable dependence on hardening is shown for large-scale yielding solution. It is worthy to note that, as the crack length increases, lower external load is required to cause the onset of crack instability.

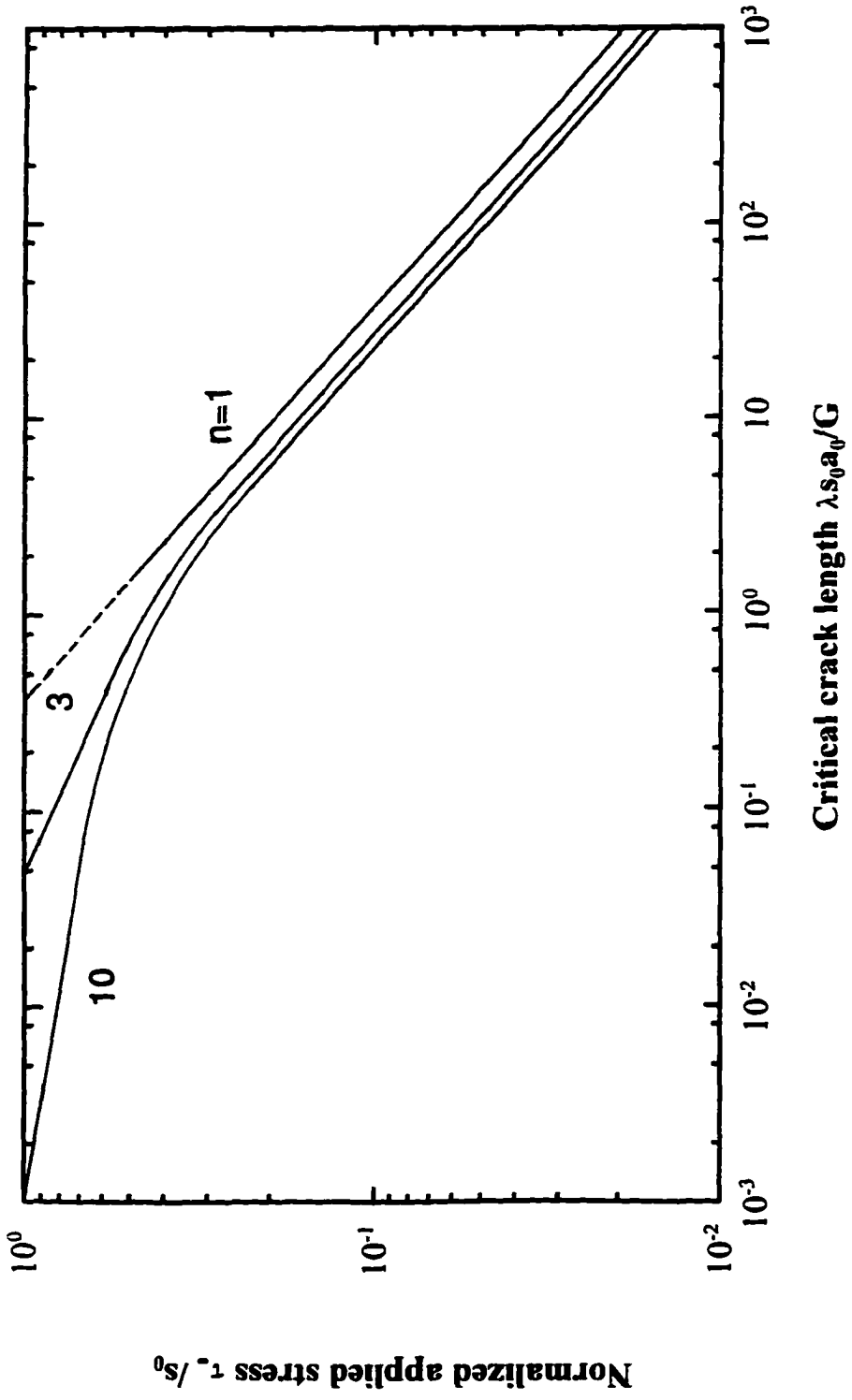

Figure 3.1 Variation of the external stress, τ_∞/s_0, with crack length, a_0.

3.3 Fatigue Crack Propagation

The course of fatigue crack propagation has been studied numerically for different material parameters and external stress levels, τ_∞/s_0. The numerical analysis revealed a strong influence of strain hardening, (n=1 to n=100), on the fatigue process.

Figures 3.2 and 3.3 exhibit the relationship between the normalized crack length, $a(N)/a_0$, and the number of loading cycles, N, with the stress level, τ_∞/s_0=0.4 and different values of material parameter, $\eta s_0 a_0 /G$, namely, 0.02 and 0.01, respectively. Figure 3.4 reveals the same behavior for τ_∞/s_0=0.6. Figures 3.2 through 3.4 show a period of incubation, where the damage accumulates without crack growth, followed by an accelerating crack growth period resulting in instability at certain crack length and number of loading cycles to failure, N_f. The crack growth period starts at the end of the incubation period where the damage parameter reaches unity at (r/2, π/2) and the corresponding number of cycles is N_i, signifying the onset of crack growth. A schematic diagram depicting the appearance of the incubation and the growth periods is shown in Figure 3.5. Comparing Figures 3.2 and 3.3, it is readily obtained that for the same stress level, (τ_∞/s_0=0.4), upon varying the material parameter ($\eta s_0 a_0 /G$) from .02 to .01, the number of cycles required for the onset of crack propagation, N_i, and for failure, N_f, is doubled for the lower material parameter. Moreover, Figures 3.3 and 3.4 indicate lower load cycles as the external stress ratio is increased from 0.4 to 0.6. This implies faster reach to the onset of crack growth and crack instability as the applied load, (τ_∞/s_0), and/or the material parameter, ($\eta s_0 a_0 /G$), are increased.

The variations of the number of cycles required for the onset of crack growth, N_i, and the

number of cycles required for failure, N_f, with external stress, τ_∞, are demonstrated in Figures 3.6 and 3.7, respectively, where (τ_∞/s_0) is shown versus N_i and N_f, for different strain hardening values, (n=1 to n=100), and fixed material parameter. The influence of the strain hardening on N_i and N_f is depicted in Figures 3.8 and 3.9, respectively, where $(\eta s_0 a_0 /G)$ is shown versus N_i and N_f, at $(\tau_\infty/s_0=0.4)$. The curves show how the number of cycles to the onset of crack growth, N_i, and number of cycles to failure, N_f, vary with the damage parameter, η, initial crack length, a_0, external stress ratio, (τ_∞/s_0), or strain hardening exponent, n. Figures 3.10 and 3.11 demonstrate the variation of the number of cycles to the onset of crack growth, N_i, and number of cycles to failure, N_f, respectively, versus the strain hardening exponent, n, for $(\eta s_0 a_0 /G) = 0.01$ and for different external stress, namely, (τ_∞/s_0) = 0.4 and 0.8.

To demonstrate the effect of material parameters and external load on a particular strain hardening exponent, Figures 3.12 thru 3.17 are developed for n=3. In Figures 3.12 and 3.13, the normalized length of the crack, $a(N)/a_0$, is shown versus the number of load cycles, N. Figure 3.12 shows the influence of material parameter, $(\eta s_0 a_0 /G)$, on the number of load cycles at a fixed external load and n = 3. It is clear that increasing the material parameter results in a lower number of cycles for the onset of crack growth and for failure. It is worthy to note that doubling the material parameter reduces the required number of cycles by half. Figure 3.13 exhibits the influence of the external applied load at constant material parameter, $(\eta s_0 a_0 /G)$, and n = 3. For decreasing value of the stress level, the number of load cycles required for failure increases. The variation of the number of cycles to the onset of crack growth, N_i, and the number of cycles to instability, N_f, is shown in Figures 3.14 and 3.15,

respectively, where ($\tau_{\_}/s_0$) is shown versus N_i and N_f, for material parameter ($\eta s_0 a_0$ /G) ranging from 0.01 to 0.08. The influence of the external stress level, ($\tau_{\_}/s_0$), on N_i and N_f, is demonstrated in Figures 3.16 and 3.17, respectively, where ($\eta s_0 a_0$ /G) is shown versus N_i and N_f, for ($\tau_{\_}/s_0$) ranging from 0.3 to 0.8. It is clear from Figures 3.14 thru 3.17 that the number of cycles required for the onset of crack growth, N_i, and for failure, N_f, increase with the reduction of damage parameter, η, initial crack length, a_0, and/or external stress ratio, ($\tau_{\_}/s_0$), for a specific strain hardening exponent.

From the results obtained in this Chapter, one is tempted to conclude that the continuous damage approach, adopted in this dissertation, describes the criterion for the onset of crack instability and the crack growth process very well, rendering reasonable figures that are comparable to conventional fracture mechanics.

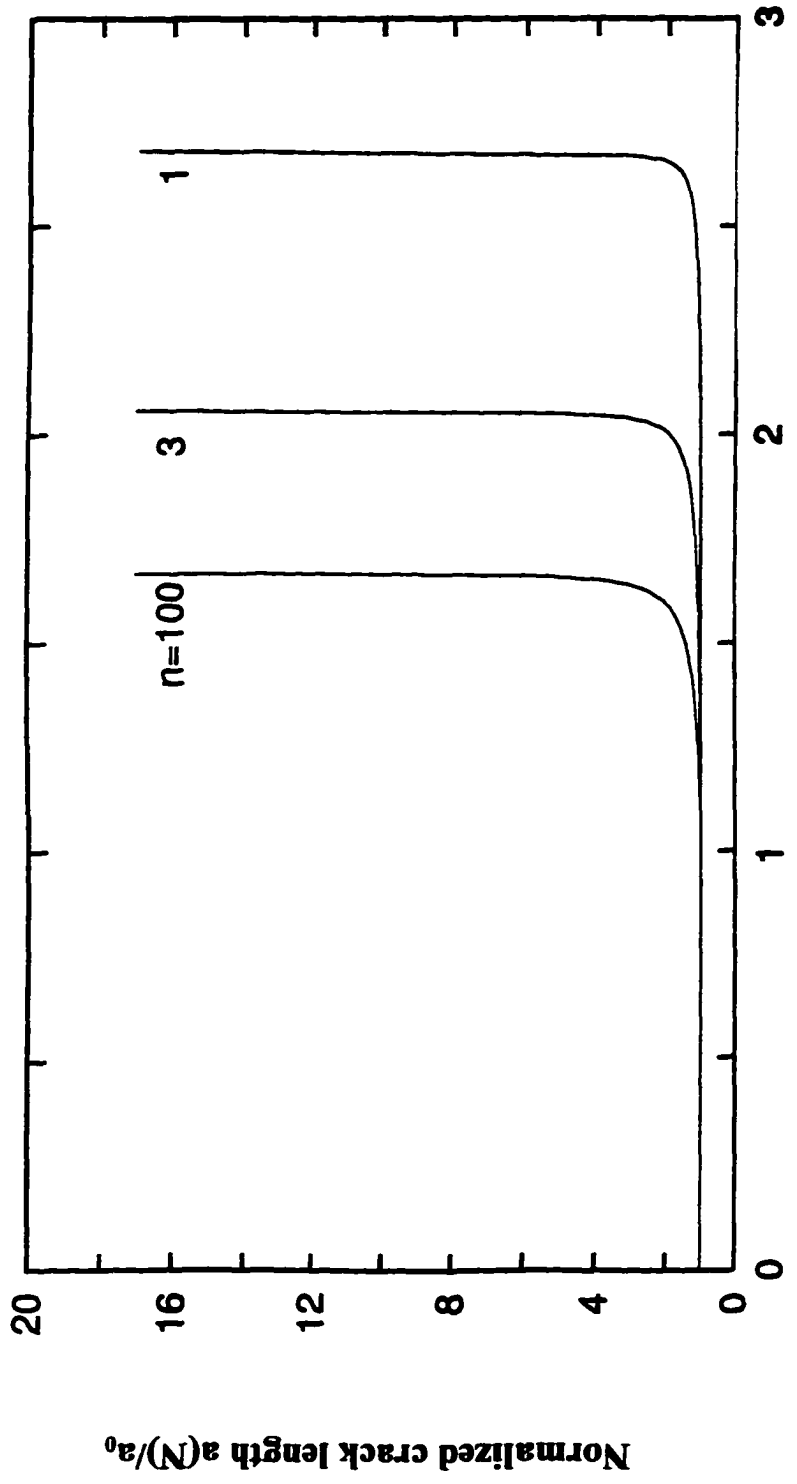

Figure 3.2 Crack growth due to cyclic loading at $\tau_a/s_0 = 0.4$ and $\eta s_0 a_0/G = 0.02$.

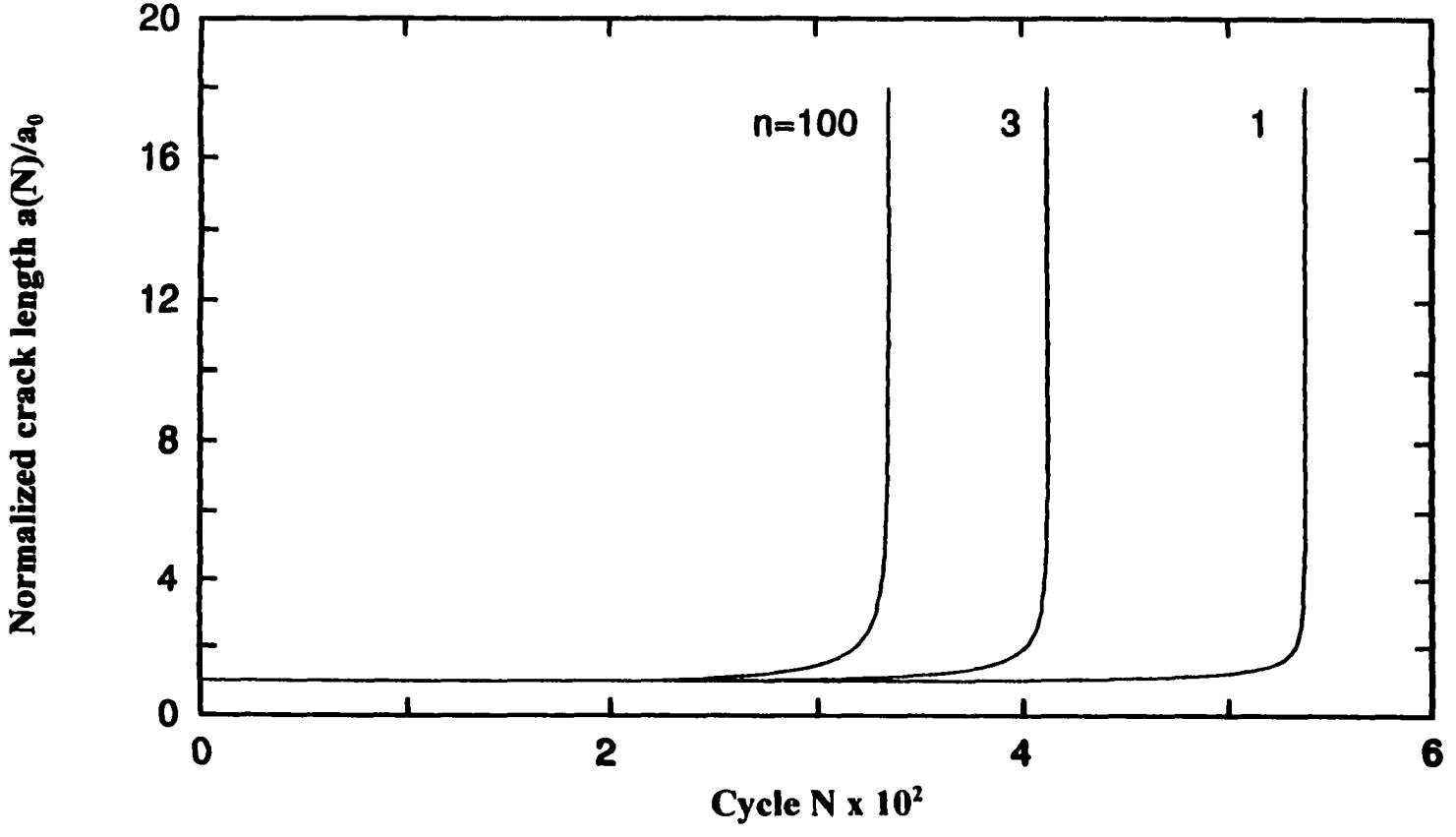

Figure 3.3 Variation of number of cycles versus normalized crack length at $\tau_f/s_0 = 0.4$ and $\eta s_0 a_0 /G = 0.01$.

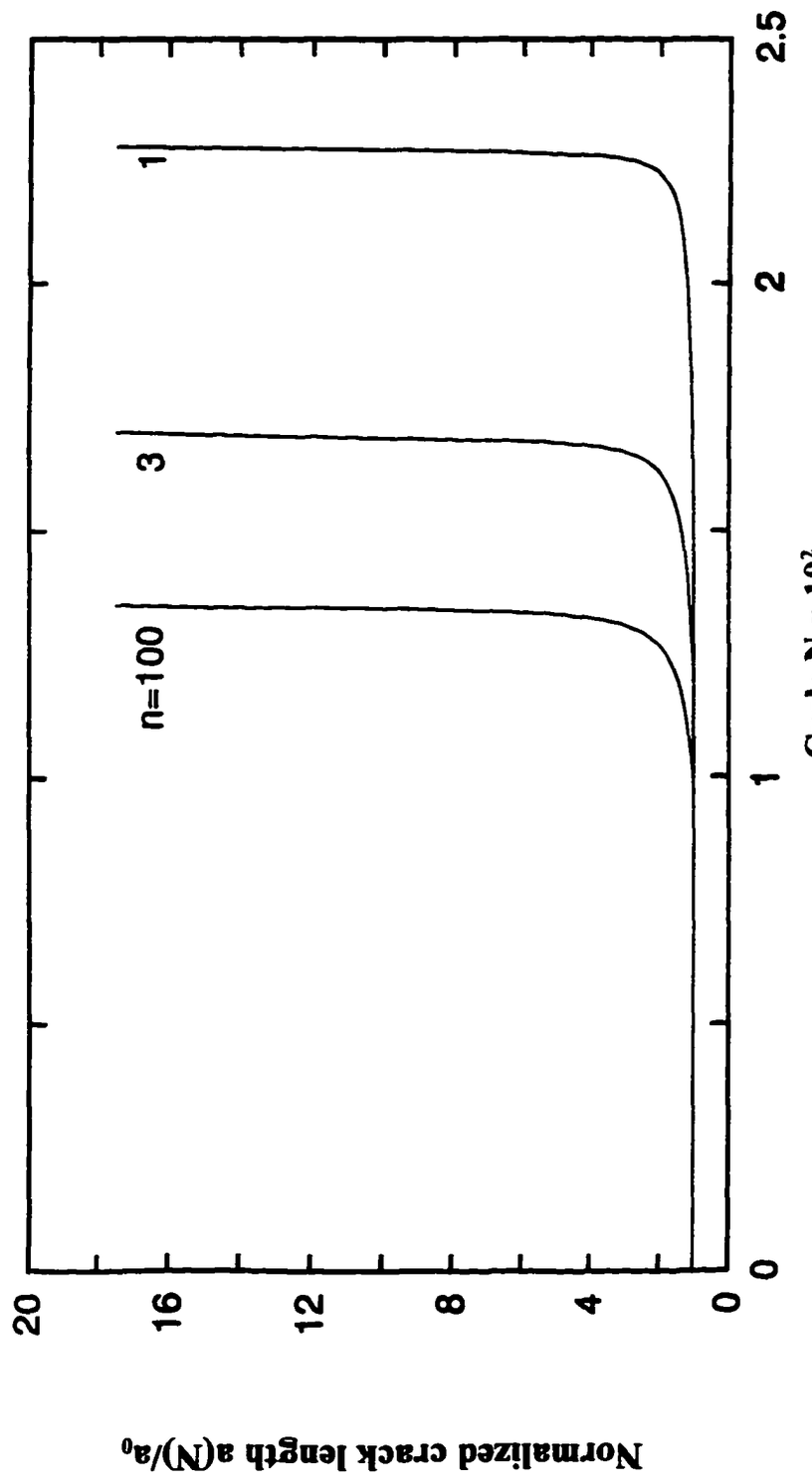

Figure 3.4 Influence of strain hardening on crack growth at $\tau_{-}/s_0 = 0.6$ and $\eta s_0 a_0 / G = 0.01$.

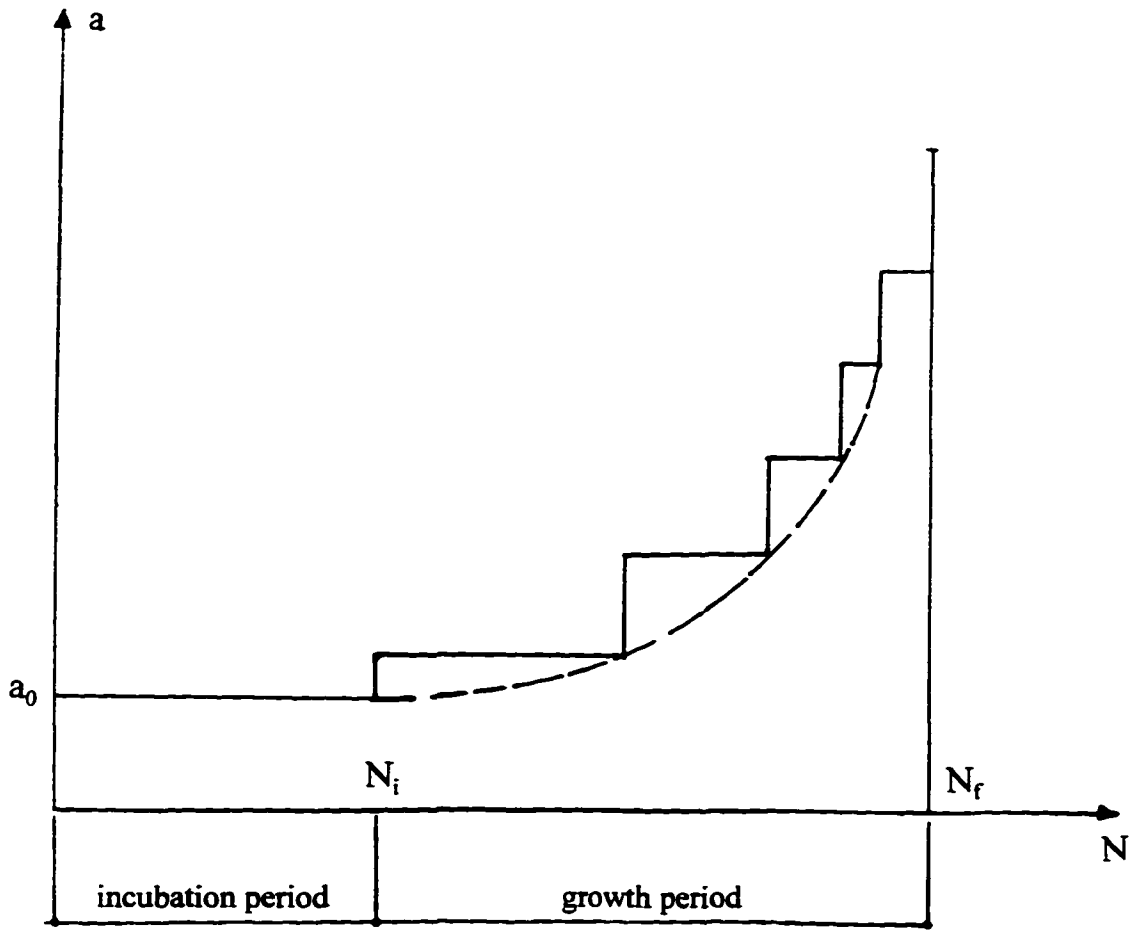

Figure 3.5 **Principal appearance of the incubation and growth periods.**

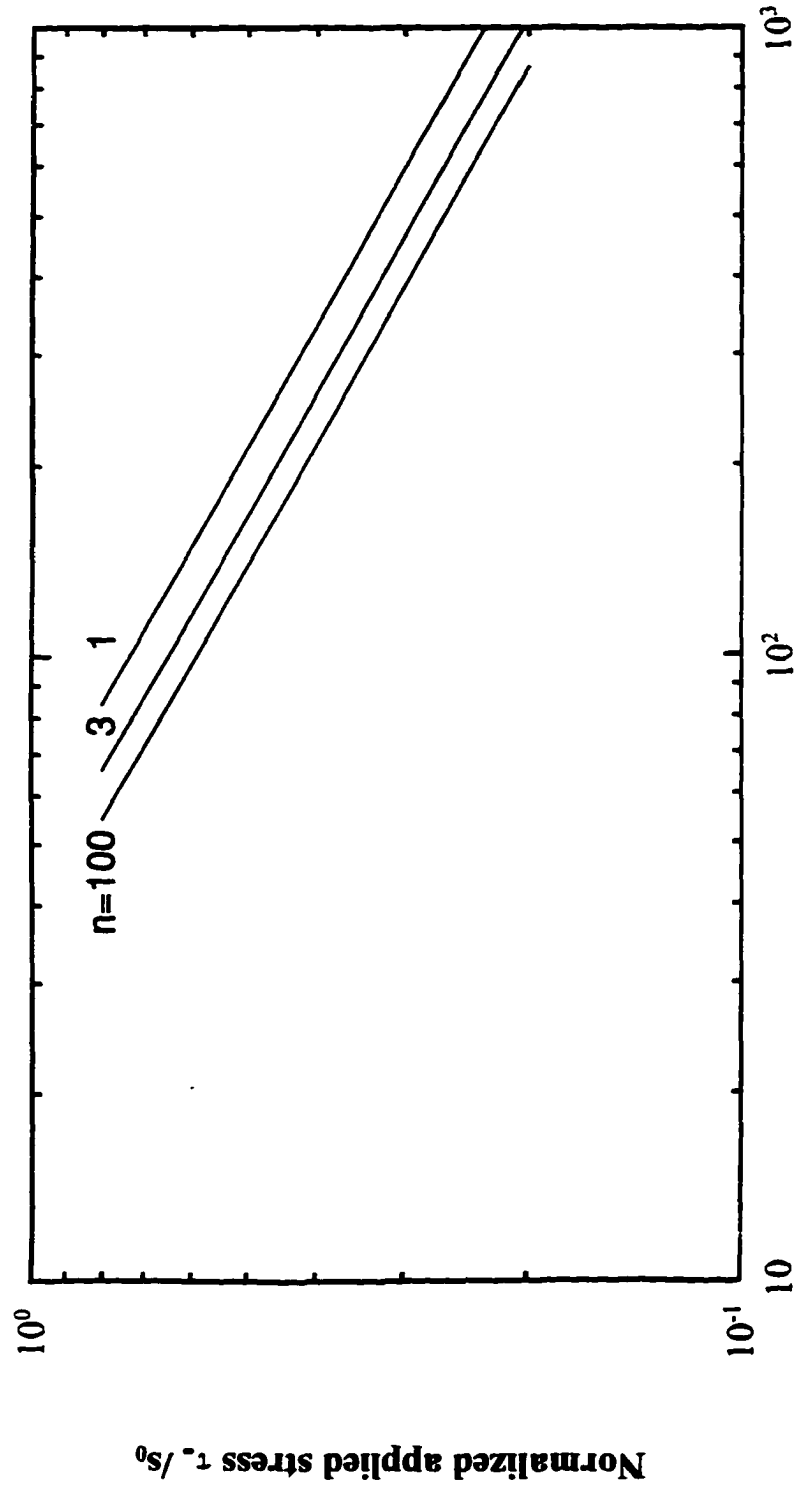

Figure 3.6 Influence of strain hardening exponent on number of cycles to the onset of crack growth at $\eta s_0 a_0 / G = 0.01$.

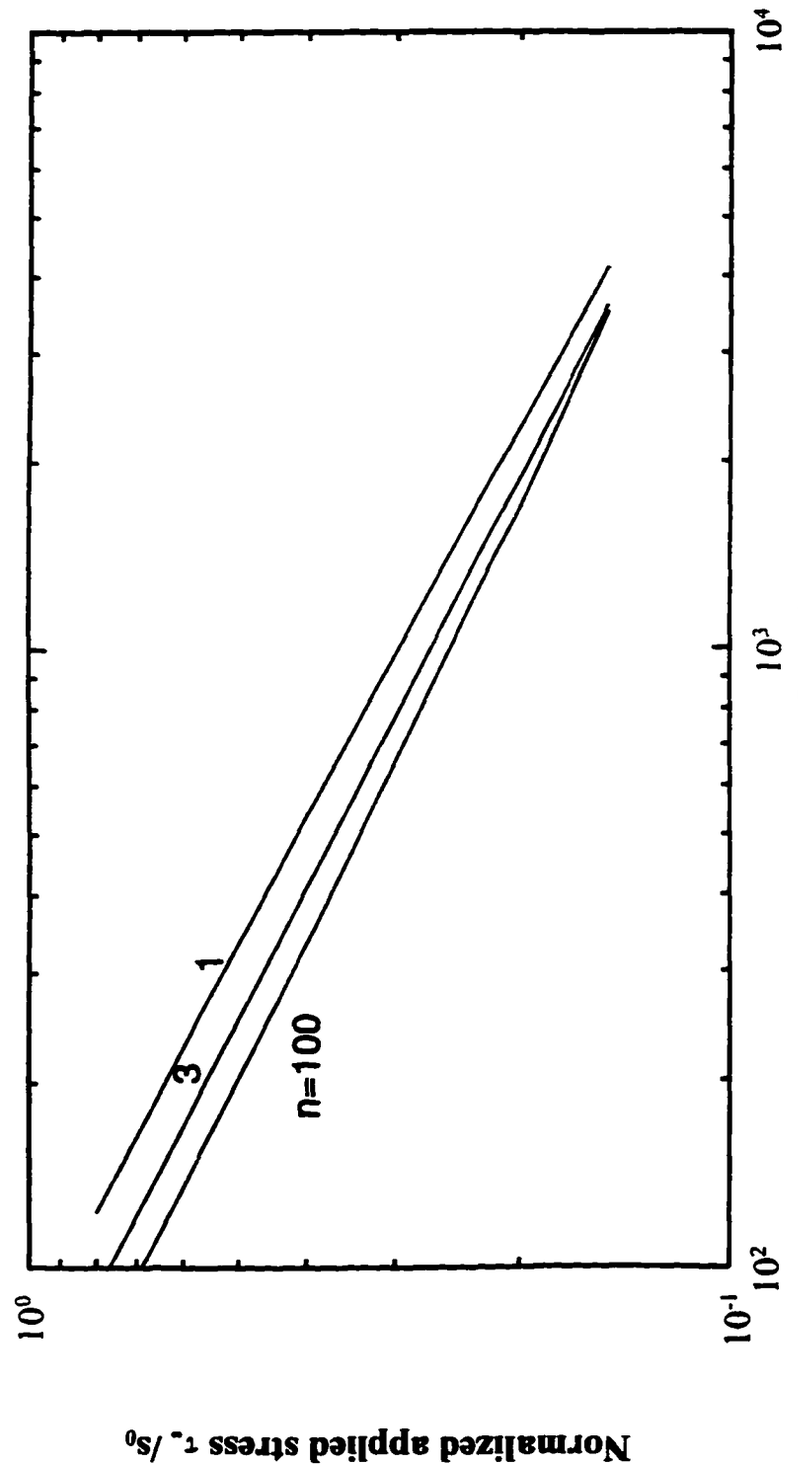

Figure 3.7 Number of cycles to failure versus external stress ratio at $\eta s_0 a_0 / G = 0.01$.

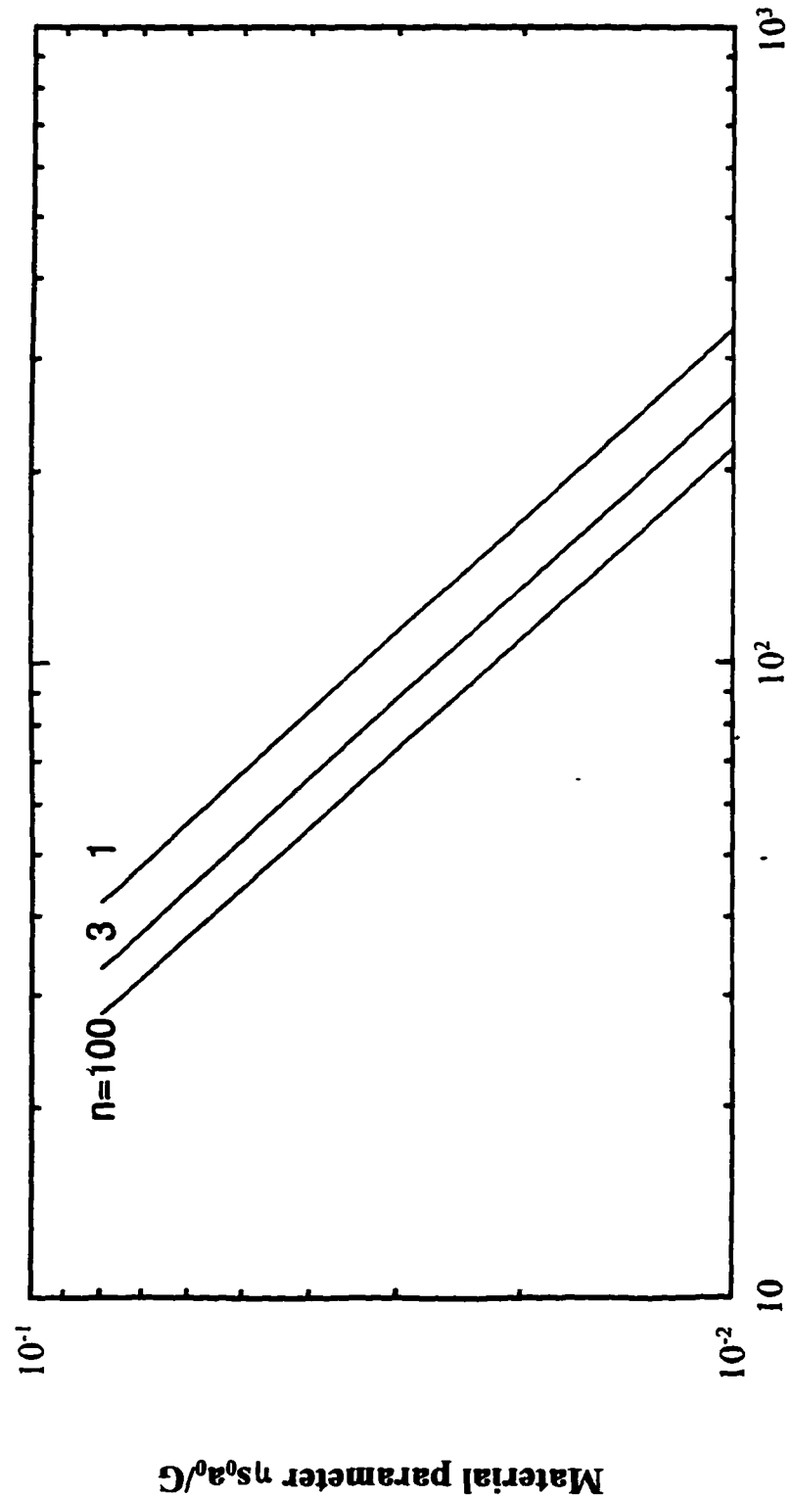

Figure 3.8 Variation of the material parameter, $\eta s_0 a_0 /G$, versus number of cycles to the onset of crack growth at $\tau_-/s_0 = 0.4$.

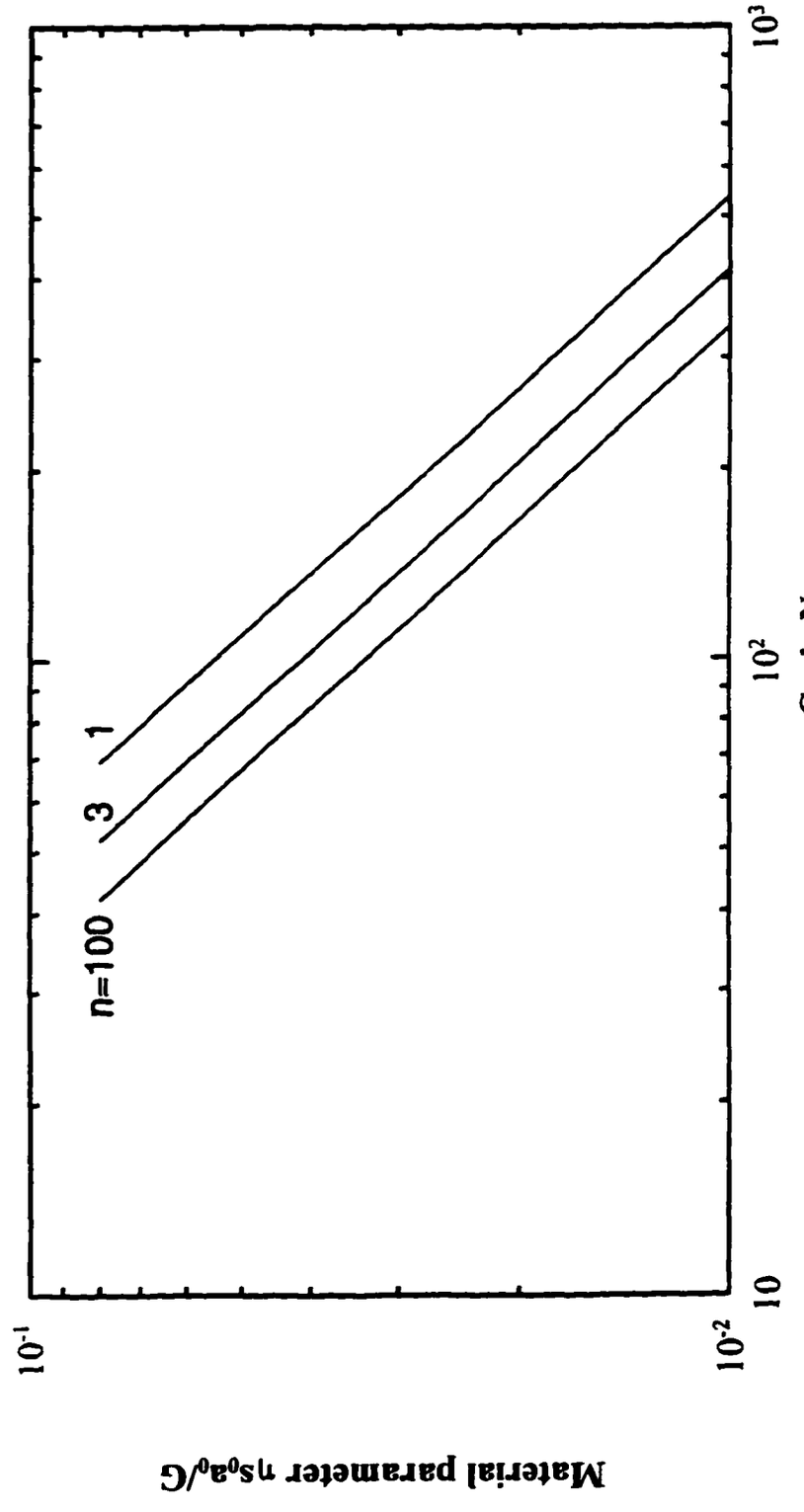

Figure 3.9 Influence of strain hardening exponent on the number of cycles to failure at $\tau_a/s_0 = 0.4$.

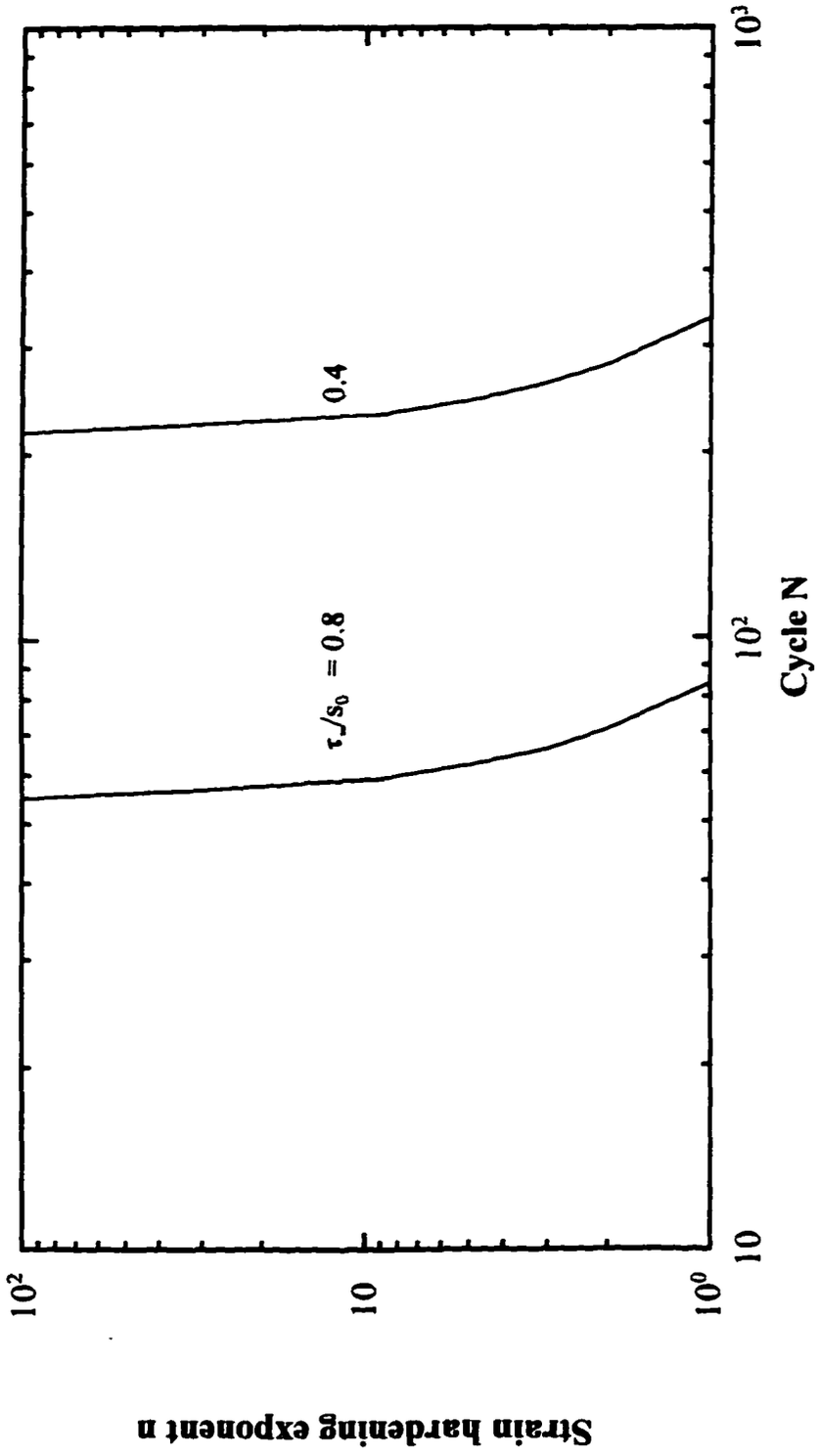

Figure 3.10 Variation of the strain hardening exponent with number of cycles to the onset of crack growth at $\eta s_0 a_0 / G = 0.01$, for $\tau_{\Delta}/s_0 = 0.4$ and $\tau_{\Delta}/s_0 = 0.8$.

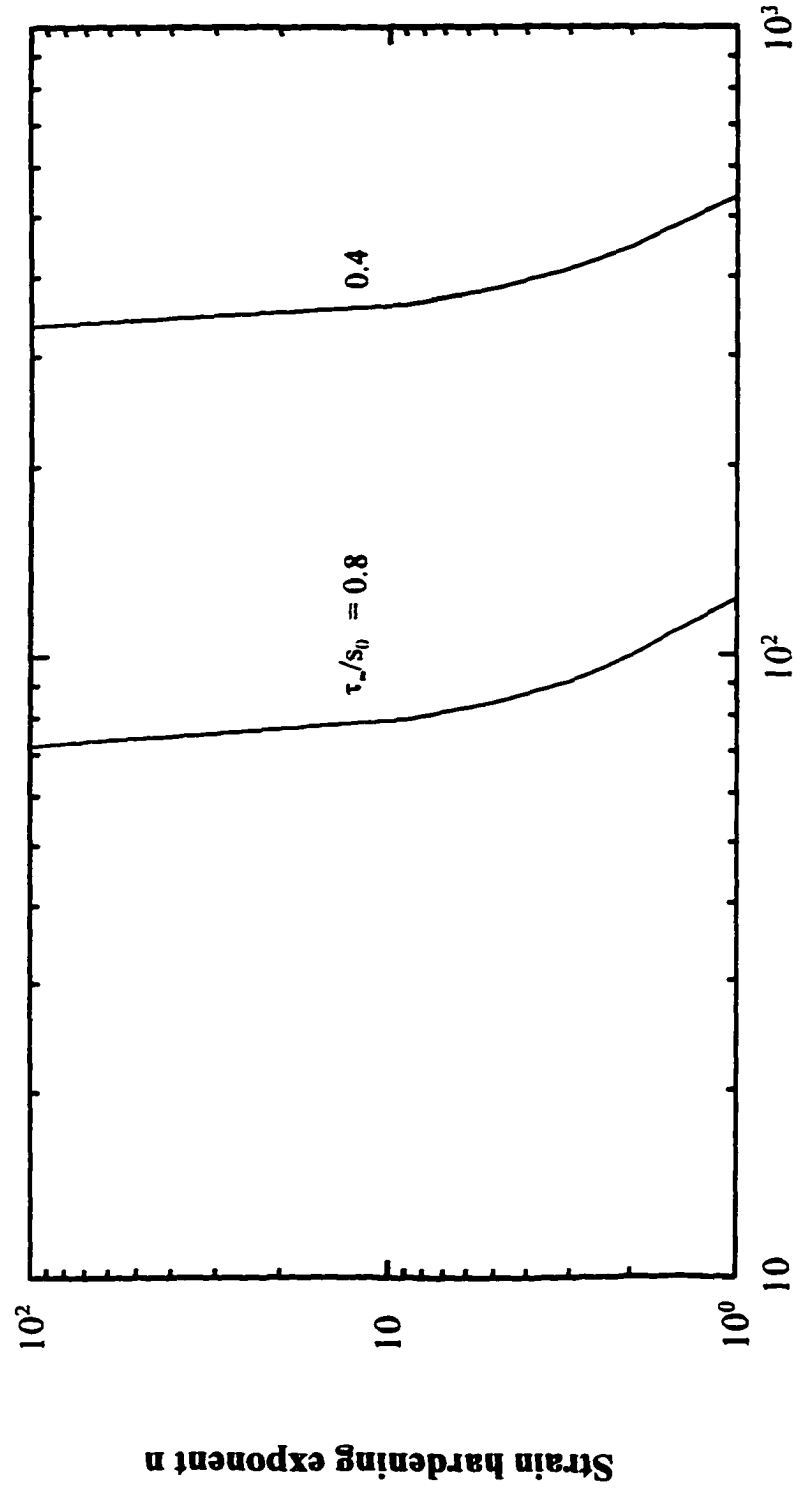

Figure 3.11 Strain hardening exponent versus the number of cycles to failure at $\eta s_0 a_0 / G = 0.01$, for $\tau_a/s_0 = 0.4$ and $\tau_a/s_0 = 0.8$.

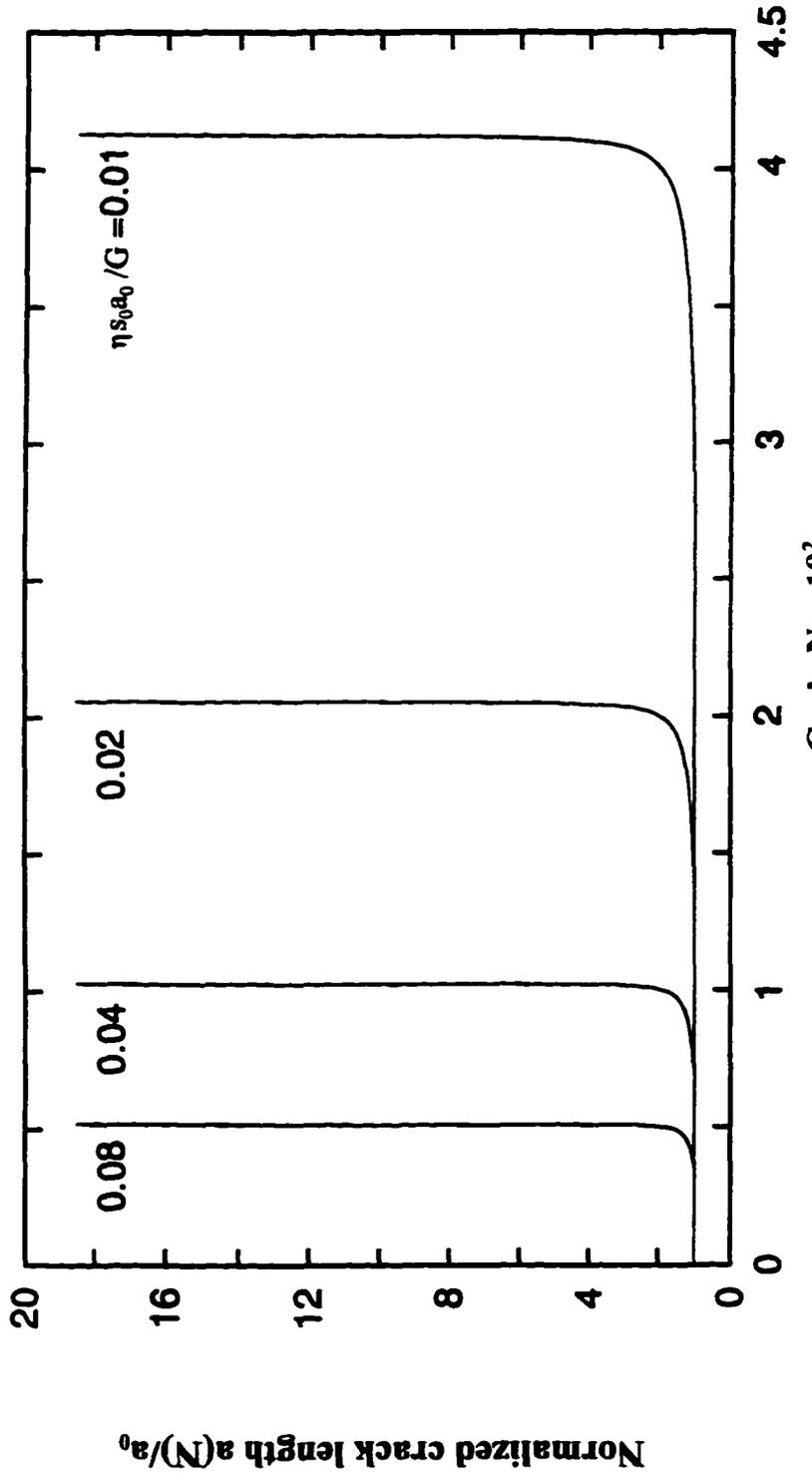

Figure 3.12 Influence of the material parameter, $\eta s_0 a_0 / G$, on fatigue crack growth at $\tau_a / s_0 = 0.4$ for $n = 3$.

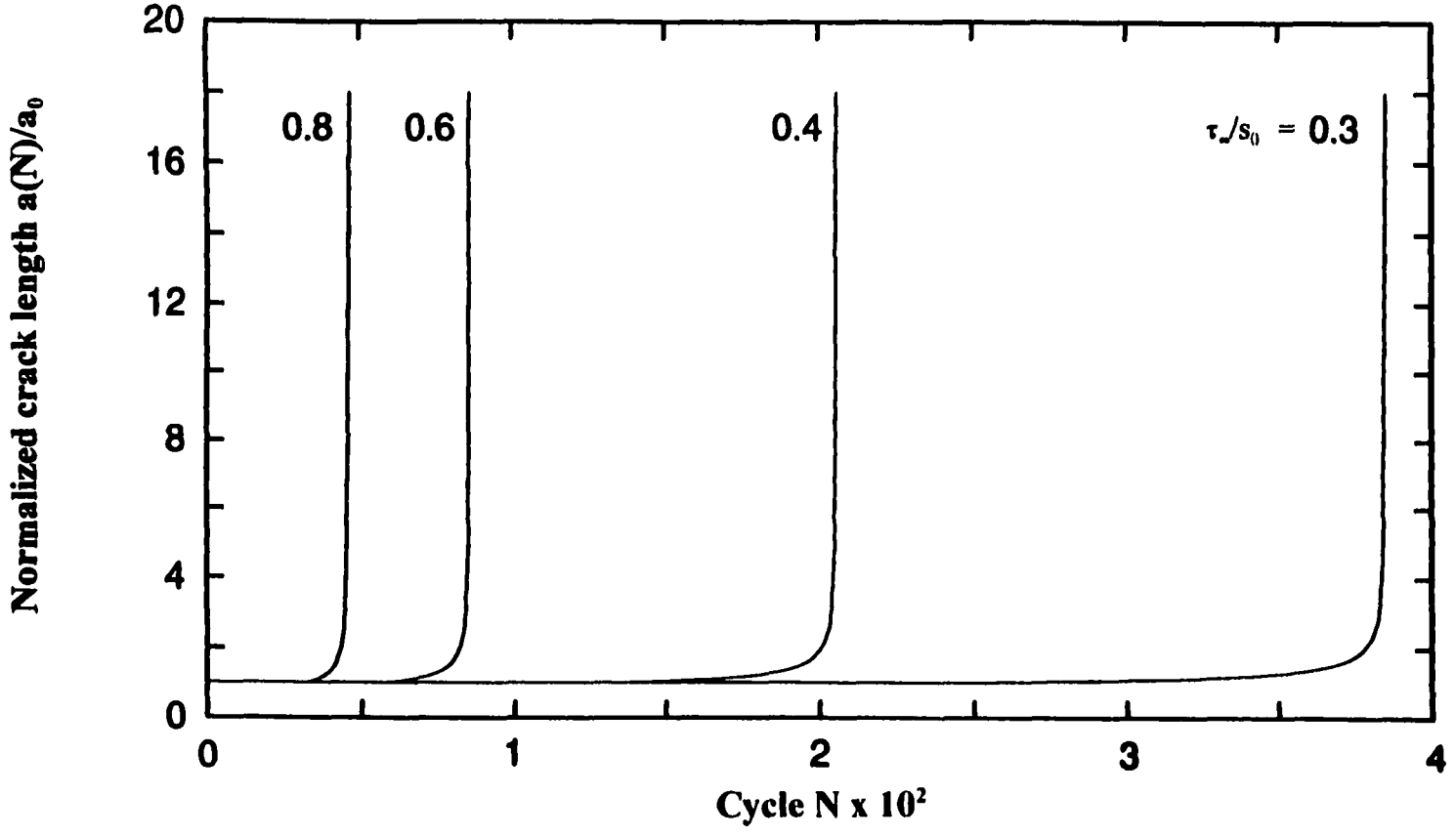

Figure 3.13 Fatigue crack growth at different external stress ratios at $\eta s_0 a_0 / G = 0.02$ for n = 3.

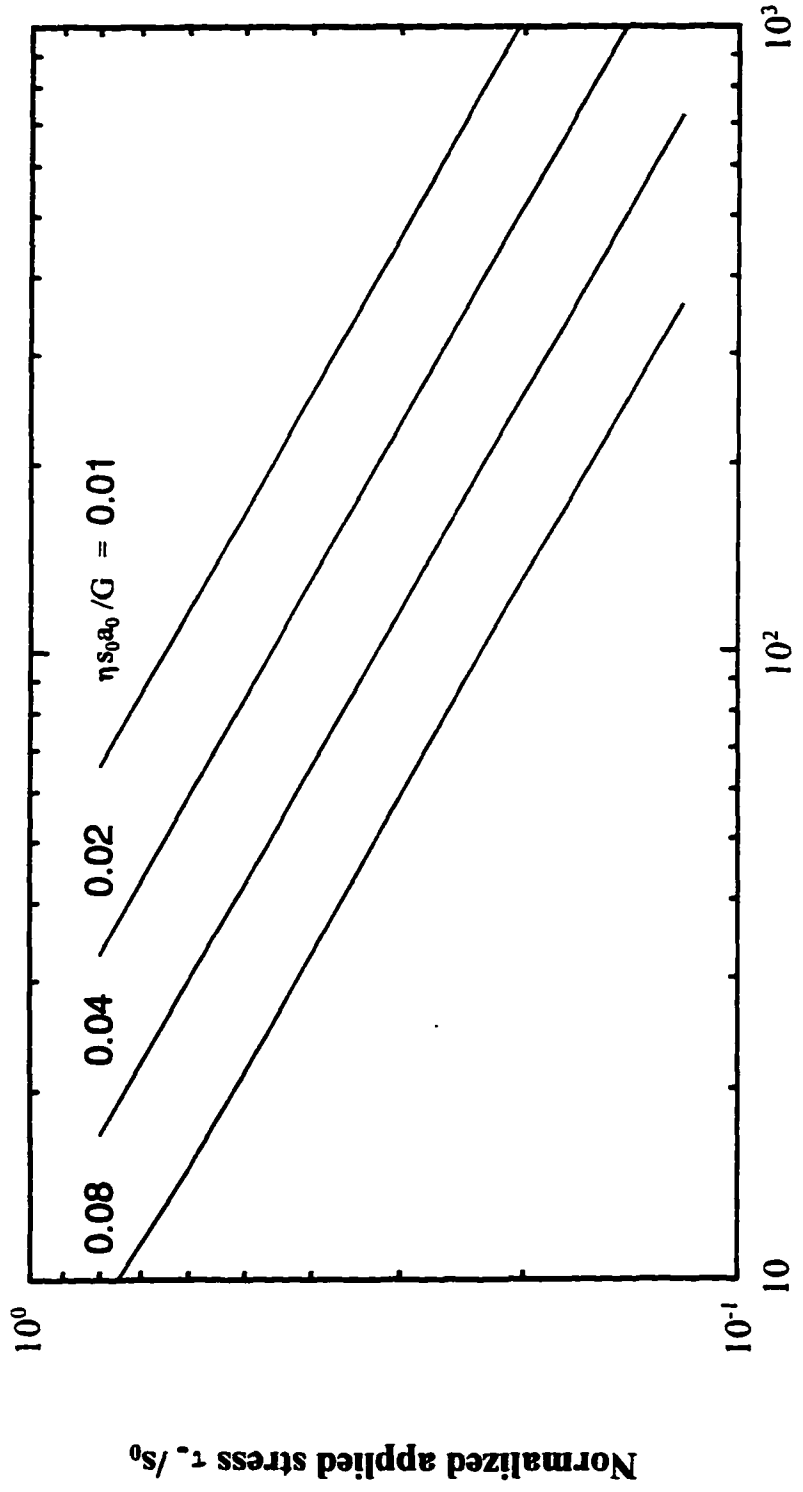

Figure 3.14 Influence of material parameter, $\eta s_0 a_0/G$, on number of cycles to the onset of crack growth for n=3.

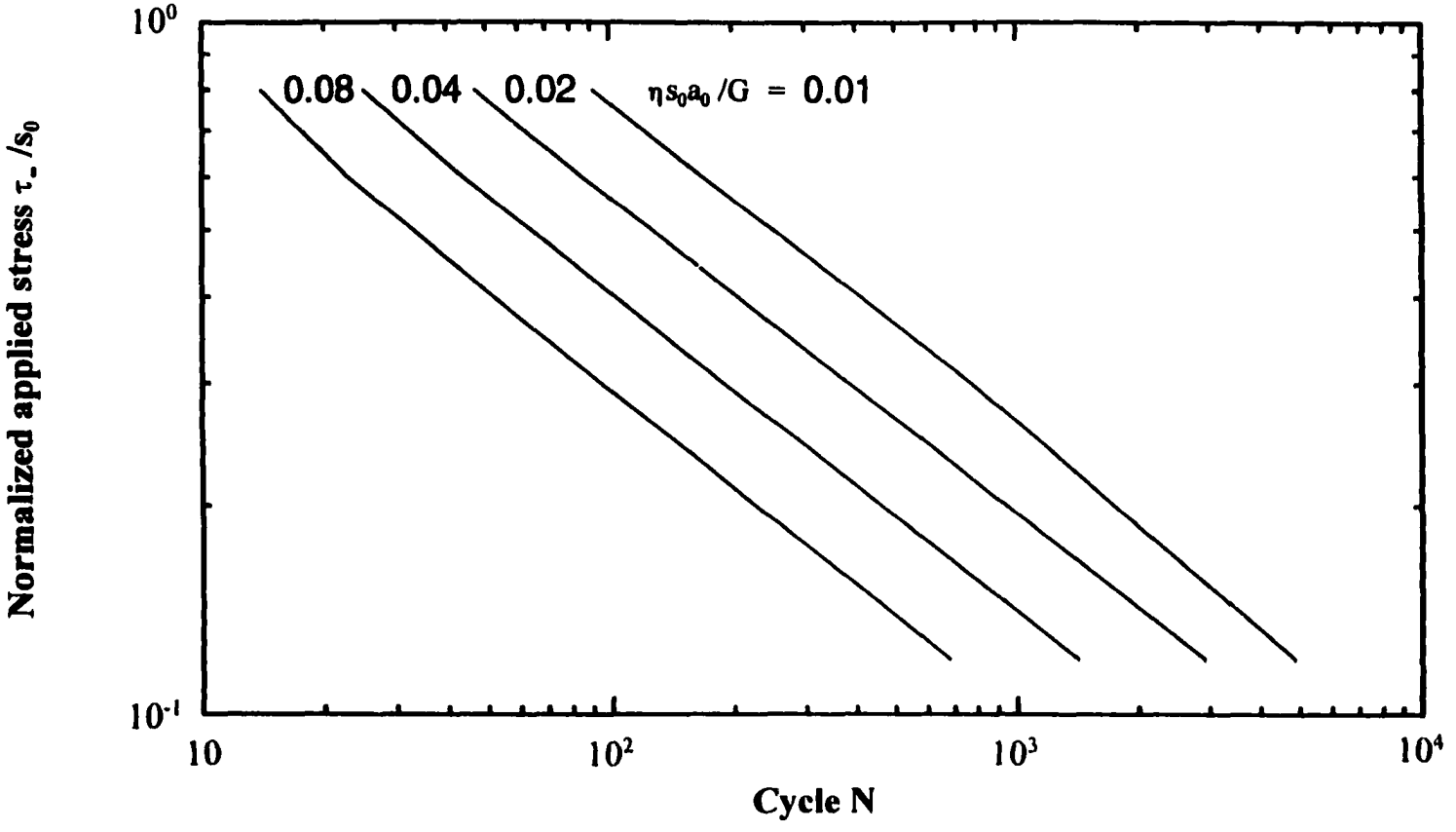

Figure 3.15 Number of cycles to failure versus external stress ratio at different values of the material parameter, $\eta s_0 a_0 /G$, for n=3.

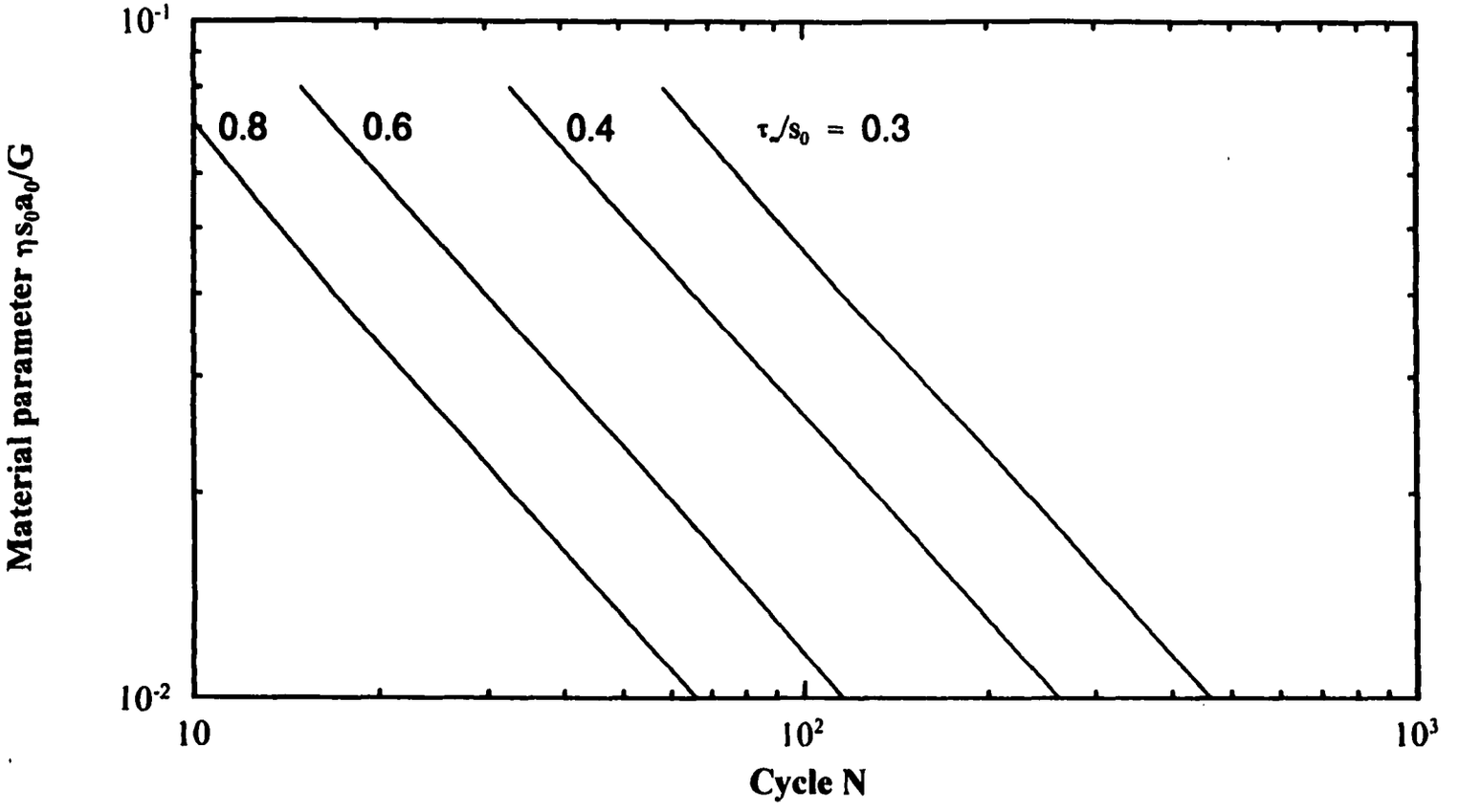

Figure 3.16 Variation of the material parameter, $\eta s_0 a_0 /G$, versus number of cycles to the onset of crack growth at different external stress ratio for n=3.

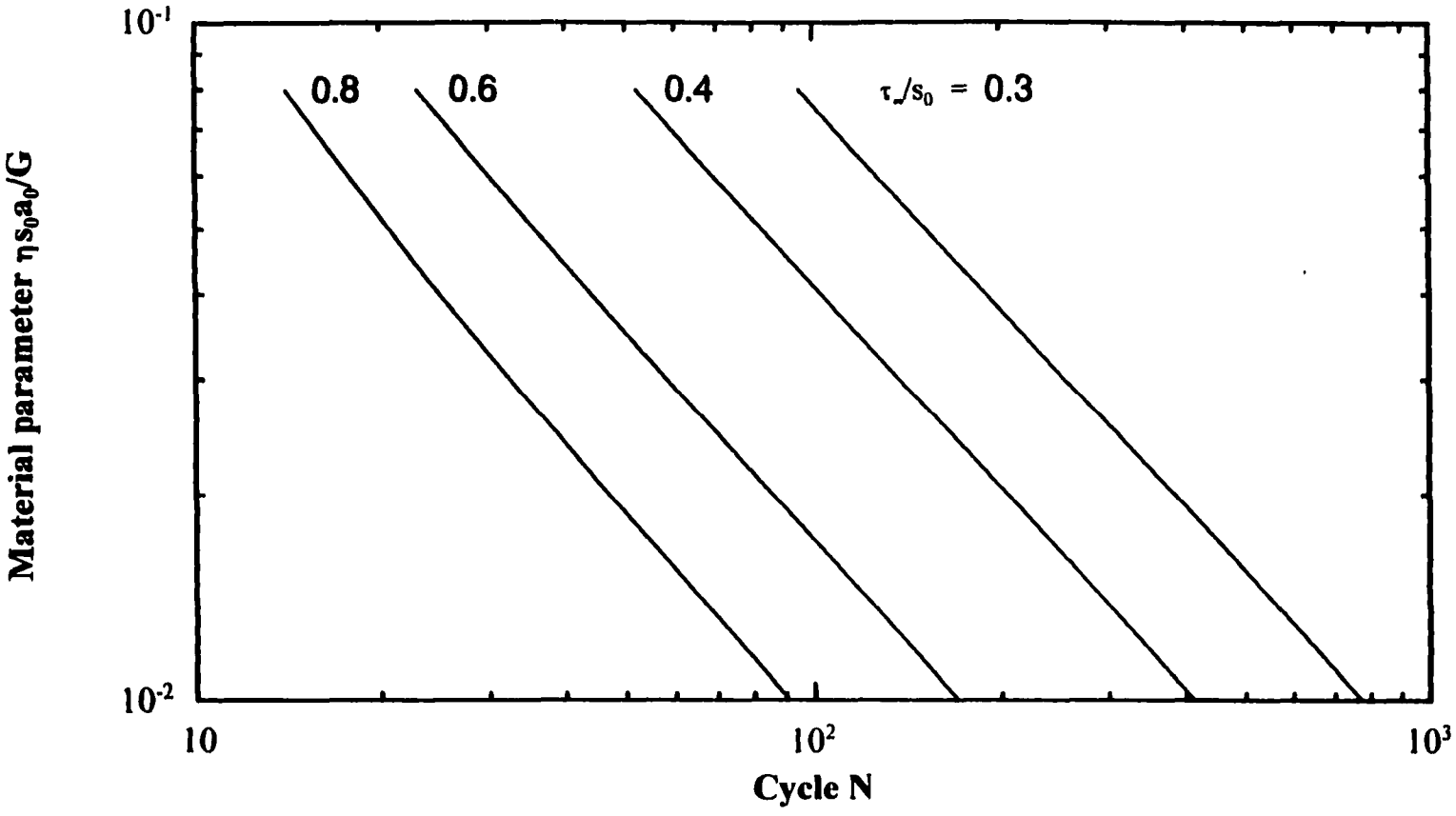

Figure 3.17 Influence of external stress ratio, τ_{-}/s_0, on number of cycles to failure for n=3.

4 TIME-DEPENDENT DAMAGE FIELD FOR A CRACK SUBJECTED TO ANTI-PLANE SHEAR LOADING (MODE III)

4.1 Introduction

The failure of structural components can occur by crack growth in the presence of creep, that is, crack growth due to increasing strain at a constant stress. Metals exhibit creep at temperatures greater than about thirty percent of their absolute melting temperatures. Many components of gas turbines, fossil and nuclear power plants and aerospace structures are required to perform at service temperatures in excess of the creep threshold temperature. On the other hand, substantial creep deformation in polymeric structures; for example, plastic piping components, can be observed at room temperature. Thus, in many situations, the service life of a structural component can be dictated by time-dependent crack growth. Figure 4.1 illustrates the typical creep response of a material subject to constant stress. Creep deformation can be divided into four regimes: instantaneous (elastic) strain, primary creep, secondary (steady-state) creep, and tertiary creep. The elastic strain occurs immediately upon application of the load and is not shown in Figure 4.1. Primary creep, which dominates at short times after application of the load, is characterized by decrease in strain rate with time as the material strain hardens. In the secondary creep stage, the deformation reaches a steady state where strain hardening and strain softening are balanced. The creep rate is constant in the secondary stage. In the tertiary stage, the creep rate accelerates as the material approaches ultimate failure.

During growth of a macroscopic crack, all four types of creep response can occur

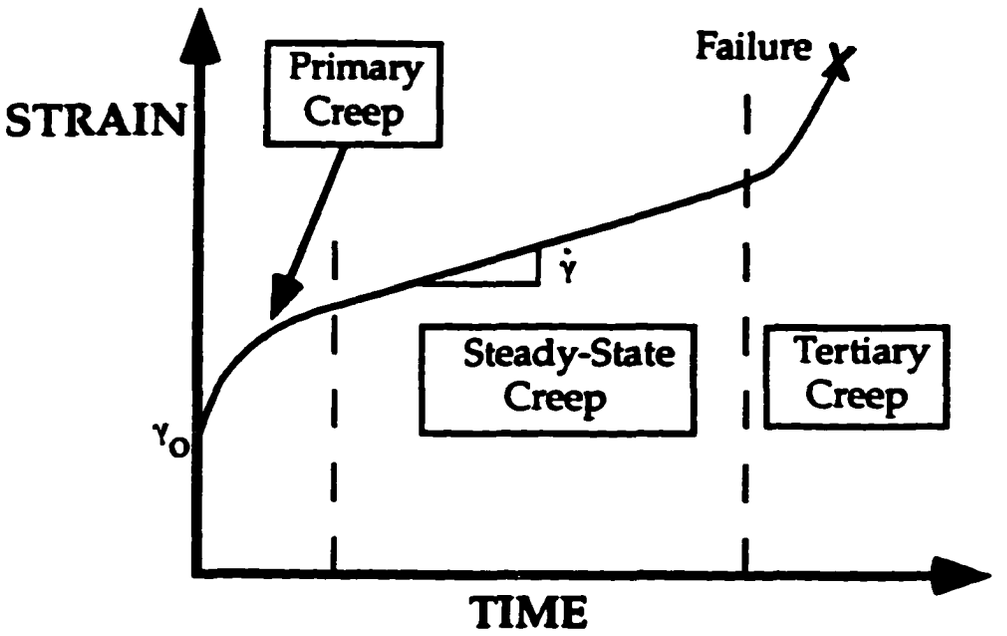

Figure 4.1 Schematic creep behavior of a material subject to a constant stress.

simultaneously in the most general case, see Figure 4.2. The material at the crack-tip is in the tertiary stage of creep since the material is obviously failing locally. At remote distance from the crack-tip, the material may be elastic, and the primary and secondary stages of creep at moderate distances from the crack-tip.

Most analytical treatments of creep crack growth assume limiting cases where one or more of these regimes are not present or are confined to a small portion of the component. If, for example, the component is predominantly elastic, and the creep zone is confined to a small region near the crack-tip, the crack growth can be characterized by the stress-intensity factor [41]. In the other extreme, when the component deforms globally in steady-state creep, elastic strains and tertiary creep can be disregarded. In this latter case, a path-independent energy rate integral (C^*-integral) is the loading parameter that determines the strength of the crack-tip fields in a body undergoing steady-state creep [42,43].

Time-dependent fracture in terms of a damage variable due to creep crack growth is considered in this Chapter. While environmentally-assisted crack growth is important and at times is difficult to separate from creep crack growth, time-dependent fracture due solely to environmental effect is not treated here. In this dissertation, creep is assumed to be artificially confined to a narrow region ahead of the crack-tip, following the idea of the Dugdale crack model [24]. Hence, the structural component is assumed to be predominantly elastic, and the steady-state creep zone and the resulting damage field is confined to a small region near the crack-tip.

By limiting the analysis in this dissertation, to small-scale yielding and to power law creep of the Ramberg-Osgood form, steady-state, or secondary creep is prevalent.

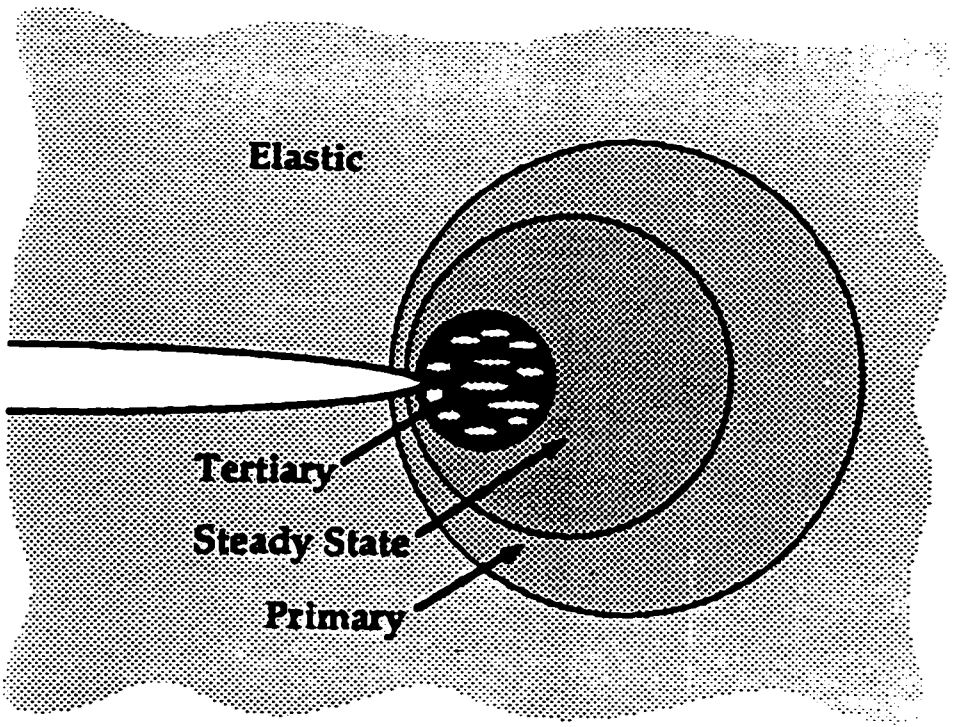

Figure 4.2 Creep zones at the tip of a crack.

Section 4.2 contains a brief summary of the basic mathematical equations required for the analysis of steady-state creep. Section 4.3 deals with creep crack growth under constant load. For given material parameters, the elapsed time required for the onset of crack growth and the elapsed time required to cause failure are determined. Section 4.4 is concerned with the numerical results. For given material parameters, the time required for the onset of crack growth and the time required for failure are determined and graphically exhibited.

4.2 Time-Dependent Basic Equations

The constitutive equations used in the time-dependent case express the rate of growth of deformation and damage for steady-state (or secondary) creep. The time-dependent deformation is characterized by the strain rate. As noted by Goldman and Hutchinson [44], and also following Hoff's analogy [45], for a creep law of the form:

$$\dot{\gamma}/\gamma_0 = (\tau/\tau_0)^n \tag{4.1}$$

the constitutive equations have the same form as the equations governing the rate-insensitive, power law strain hardening material. Thus, the formulas developed in Chapter 2, describing the displacement field and plastic zone extension ahead of the crack-tip all continue to hold if the strain, γ, is replaced by the strain rate, $\dot{\gamma}$, and the displacement, w, is replaced by its rate, $\dot{w}$. Here n is the creep exponent, and the dot indicates differentiation with time.

Introducing Lemaitre's strain equivalence principal to equation (4.1), one can write:

$$\dot{\gamma}/\gamma_0 = (s/s_0)^n \tag{4.2}$$

For time-dependent deformation, the reference stress, τ_0, is related to the reference strain rate, $\dot{\gamma}_0$, for a virgin material, by the relation:

$$\tau_0 = H.\dot{\gamma}_0 \tag{4.3}$$

where H is a time-dependent material parameter.

The deformation is composed of one instantaneous part and one time-dependent part. No damage is assumed to be induced immediately on loading. Thus, introducing the rate of damage of the material, $\dot{D}$, consisting of a uniform component, $\dot{D}_0$, and a component proportional to the crack opening displacement, one can write:

$$\dot{D}(r,\theta;t) = \dot{D}_0 + \beta.w(r,\theta;t) \tag{4.4}$$

where β is a damage parameter and t denotes the time. This equation can be integrated in time to give:

$$D(r,\theta;t) = \int_0^t \dot{D}_0 \, dt' + \beta \int_0^t w(r,\theta;t') \, dt' \tag{4.5}$$

As assumed in the rate-insensitive case (Chapter 2), most damage is confined to a narrow band of large deformation ahead of the crack-tip. Then, as with equation (2.11), the stress in the damage-zone can be expressed as:

$$\tau(r,\theta;t) = s_0 \{ 1 - \int_0^t \dot{D}_0 \, dt' - \beta \int_0^t w(r,\theta;t') \, dt' \} \tag{4.6}$$

In the time-dependent case, both the crack and the damage-zone boundary will grow into the component with time. $\dot{D}_0$ has been assumed to depend on the net stress far from the crack, s_∞. It follows that, using equation (2.11):

$$s_\infty = \tau_\infty / (1 - D_0) \tag{4.7}$$

where $D_0 = \int_0^t \dot{D}_0 \, dt'$.

A power law, commonly used in brittle creep rupture [3], may be used to relate $\dot{D}_0$ to s_∞, such that:

$$\dot{D}_0 = \kappa (s_\infty / s_0)^\vartheta \tag{4.8}$$

where κ and ϑ are material constants independent of stress and time. Combining equations (4.7) and (4.8) yields:

$$\dot{D}_0 = \kappa [\tau_\infty / (s_0 (1 - D_0))]^\vartheta \tag{4.9}$$

Assuming the applied load, τ_∞, is constant in time, equation (4.9) can be integrated in time, using zero initial conditions, to yield:

$$D_0 = 1 - [1 - (\vartheta + 1) \kappa (\tau_\infty / s_0)^\vartheta \, t]^{1/(\vartheta+1)} \tag{4.10}$$

Additional damage due to deformation of the material in the creep-damage-zone is added to

equation (4.10). It is assumed that, at a certain time, every point in the component except for the damage-zone around the crack-tip, has a damage D_0 given by equation (4.10). Because of this uniform damage outside the zone, the stress and net stress distributions will be the same as in the rate-insensitive case, developed in Chapter 2, an important fact for the following analysis. The damage and stress within the damage-zone can now be written using equations (4.5), (4.6) and (4.10) as:

$$D(r,\theta;t) = 1 - [1 - (\vartheta + 1)\,\kappa\,(\tau_- / s_0)^{\vartheta}\, t\,]^{1/(\vartheta+1)} + \beta \int_0^t w(r,\theta;t')\,dt' \tag{4.11}$$

$$\tau(r,\theta;t) = s_0 \{ [1 - (\vartheta + 1)\,\kappa\,(\tau_- / s_0)^{\vartheta}\, t\,]^{1/(\vartheta+1)} - \beta \int_0^t w(r,\theta;t')\,dt' \} \tag{4.12}$$

Assuming $\tau(r,\theta;t) = \Omega(t)\, s_0 =$ constant, the extension of the creep-damage-zone ahead of the crack-tip is obtained from:

$$C(t) = [n / (n+1)][K_{III}^2 / (\pi(\Omega(t)s_0)^2)] \tag{4.13}$$

At a certain time:

$$w(r,\theta;t) = w(r,\theta;0) + \int_0^t \dot{w}(r,\theta;t')\,dt' \tag{4.14}$$

where according to equation (2.33), for small-scale yielding:

$$w(r,\theta;t) = (K_{III}^2 / (G\pi[\Omega(t)]^2 s_0))\,\sin\phi \tag{4.15}$$

and the rate of displacement follows as:

$$\dot{w}(r,\theta;t) = (K_{III}^2 / (H\pi[\Omega(t)]^2 s_0))\,\sin\phi \tag{4.16}$$

In section 4.3, equations (4.2) through (4.16) are used to develop the conditions for time-dependent damage due to steady-state creep. It should be noted that r, in the following calculations, indicates the distance from the crack-tip to the elastic-plastic boundary, given in equation (4.13).

4.3 Time-Dependent Damage

By equating the approximate stress value $\Omega(t)s_0$ and the exact stress value from equation (4.12), at $(r, \pi/4)$, the continuity function, $\Omega(t)$, is given by:

$$\Omega(t) = [1 - (\theta + 1)\,\kappa\,(\tau_- / s_0)^\theta\, t\,]^{1/(\theta+1)} - \beta \int_0^t w(r,\pi/4;t')\,dt' \} \qquad (4.17)$$

where one can solve for $\Omega(t)$ in equation (4.17) at a certain time by iteration. To solve for $D(r,\theta;t)$, one needs to perform an integration in time. This is made approximately by straight-forward calculations at finite time steps as follows: At time $t=0$, there is no damage and $\Omega(0) = 1$. The displacement and displacement rate, $w(r,\theta;0)$ and $\dot{w}(r,\theta;0)$ are determined from equations (4.15) and (4.16), respectively, with $\Omega(0)=1$. At time $t=\Delta t$, assume a linear variation of $w(r,\theta;t)$ during a time step. Then, from equation (4.11), it is readily shown that:

$$D(r,\theta;\Delta t) = 1-[1-(\theta + 1)\kappa\,(\tau_- / s_0)^\theta\, t\,]^{1/(\theta+1)} + \beta[\, w(r,\theta;0)\Delta t + (1/2)\,\dot{w}(r,\theta;0)\,(\Delta t^2) \qquad (4.18)$$

and the crack opening is obtained using:

$$w(r,\theta;\Delta t\,) = w(r,\theta;0) + \dot{w}(r,\theta;0)\,\Delta t \qquad (4.19)$$

As shown in Figure 4.3, if the damage, $D(r,\pi/2\,;\Delta t)$, is less than unity then the crack has not grown during the time interval and, $a(\Delta t) = a_0$, the initial crack length. The damage at $(r,\pi/4)$ is obtained from equation (4.11) and the continuity function from equation (4.17) and the time t is increased to $(t+\Delta t)$ and Ω of this step is used to update the displacements and the displacement rates at $(r,\pi/2)$ and $(r,\pi/4)$. By using equations (4.11) and (4.15)-(4.19), an iterative procedure is repeated until $D(r,\pi/2;t)$ slightly exceeds unity, then the crack has grown during the time interval as indicated schematically in Figure 4.3.

The new crack length is found from the condition:

$$D(r,\pi/2;\Delta t) = 1. \qquad (4.20)$$

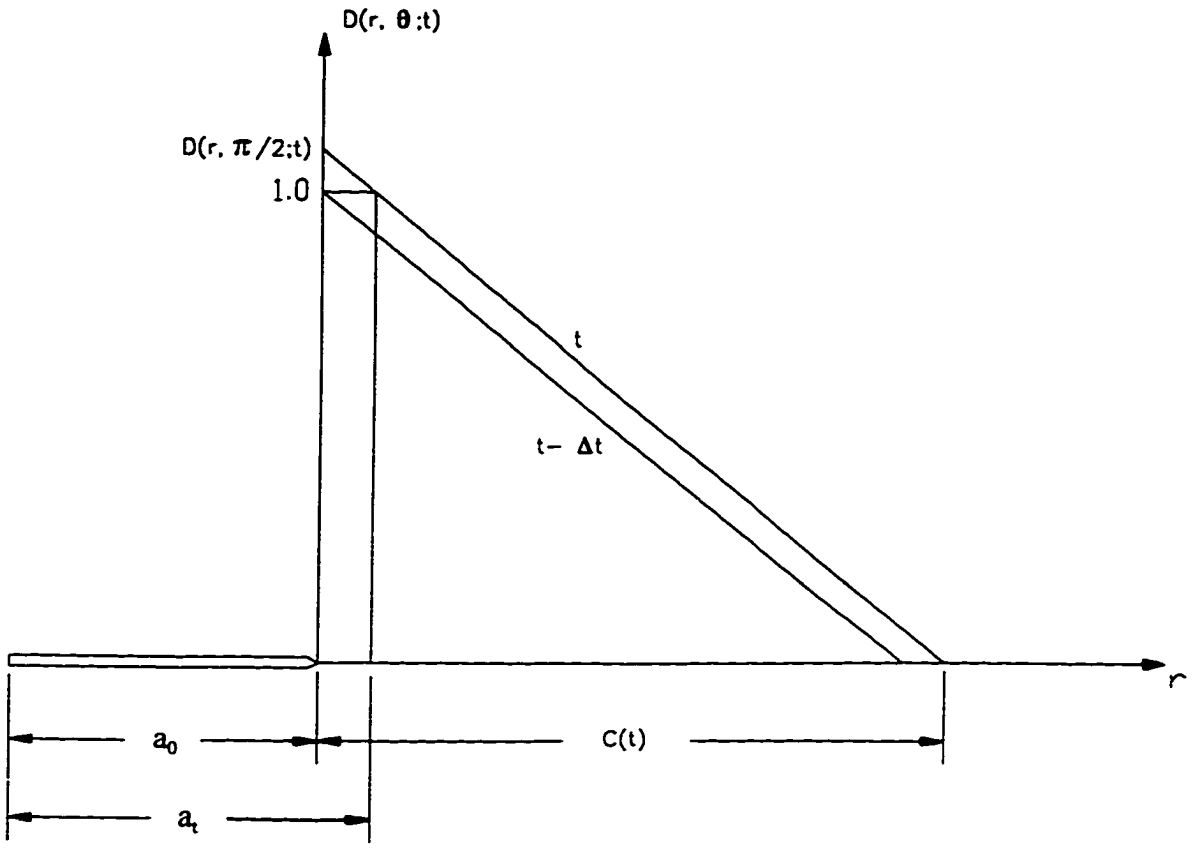

Figure 4.3 Description of creep crack growth criterion.

The new crack length is given by:

$$a_t = a_0 + da_t \tag{4.21}$$

where:

$$da_t = [1-\{1/D(r,\pi/2;t)\}]\, C(t) \tag{4.22}$$

Using the new crack length, the iterative process can be repeated for $t = 2\Delta t, 3\Delta t, \ldots$, etc., until instability is reached, i.e., the critical length of the crack grows to very high values.

The creep crack growth numerical results are dealt with in section 4.4. The influence of creep exponent and material parameters on the variations of the time with the critical crack length are presented and graphically displayed.

4.4 Time-Dependent Crack Growth Numerical Results

In sections 4.2 and 4.3, a circular creep-damage zone in terms of time parameter, engulfing the crack-tip and crack growth under steady state, or secondary, creep was determined. This Chapter presents the numerical discussion of the developed creep crack growth criterion.

The numerical results are presented in two parts. First, the variation of the crack length with time, and the time required for the onset of crack growth as well as the time required for reaching a critical crack length, causing instability are found for various external loads and material parameters and graphically presented in section 4.4.1. Second, the theoretical instability time, which is purely a creep phenomenon, is determined for different external loads and material parameters and graphically displayed in section 4.4.2.

4.4.1 Creep Crack Growth

The course of creep crack growth has been studied numerically for different material parameters and external stress levels. The numerical analysis revealed a somewhat moderate influence of the creep exponent, n=1 to n=100, on the creep process. Figures 4.4 and 4.5 exhibit the relationship between the normalized crack length, $a(t)/a_0$, and time for various creep exponents and material parameter ($\beta s_0 a_0/G$) at constant stress level and modular ratio H/G. Figures 4.6 thru 4.8 exhibit similar relationship between the normalized length of the crack, $a(t)/a_0$, and time for various modular ratio H/G and material parameter. Figures 4.4 through 4.8 reveal a period of incubation, where the damage accumulates with no crack growth, followed by a period of accelerating crack growth resulting in instability at a certain finite time. The crack growth period starts at the end of the incubation period where the damage parameter reaches unity at $(r, \pi/2)$ and the corresponding time is t_i, signifying the elapsed time required for the onset of crack growth. A schematic diagram depicting the appearance of the incubation and growth periods is shown in Figure 4.9.

Upon examining Figures 4.4 through 4.8, it appears that for a fixed stress value, τ_∞/s_0, an increase of the damage parameter, β, and/or a decrease of the ratio, H/G, will lower both the time needed for the onset of crack growth and the time needed for failure. In particular, the effect of initial crack length, a_0, in speeding up the crack growth can be noticed. It is also clear from examination of these Figures that an increase in the stress level, τ_∞/s_0, corresponds to a decrease in the time required for the onset of crack growth and failure. This decrease will be even more pronounced when the increase in the stress level is associated with an increase in the damage parameter, β, (and/or a decrease in H/G), which implies a faster reach

to the onset of crack growth and crack instability.

The variations of the elapsed time required for the onset of crack growth, t_i, and the elapsed time required for failure, t_f, with external stress, τ_∞, are shown in Figures 4.10 and 4.11, respectively. As expected, lower stress level is needed to cause crack growth for decreasing values of the creep exponent n. The variations of t_i and t_f with $(\beta s_0 a_0/G)$ are shown in Figures 4.12 and 4.13, respectively. The curves show how the elapsed time required for the onset of crack growth, t_i, and the elapsed time required for failure, t_f, vary with the damage parameter, β, initial crack length, a_0, external stress level, (τ_∞/s_0), and the creep exponent, n. It is clear that the elapsed time required for the onset of crack growth and the time required for failure increase with reduced values of the material parameter, $(\beta s_0 a_0/G)$, and/or values of the creep exponent, n. Figures 4.14 and 4.15 demonstrate the variation of the creep exponent, n, with the elapsed time required for the onset of crack growth, t_i, and the elapsed time required for failure, t_f, respectively, for stress levels varying in the range, (τ_∞/s_0)=0.3 and (τ_∞/s_0)=0.7. No significant change in the elapsed times t_i and t_f occur for values of n greater than 10.

To demonstrate the effect of material parameters and external stress on a particular creep exponent, Figures 4.16 thru 4.22 are developed for n=3. Figures 4.16 thru 4.18 show the normalized length of the crack, $a(t)/a_0$, versus time for different combinations of material parameters. In Figure 4.16, the effect of material parameter, $(\beta s_0 a_0/G)$, ranging from 2.0 to 16.0, is shown for constant stress level and modular ratio. It is clear that increasing the material parameter corresponds to a decrease in the elapsed time required for failure. Figure 4.17 depicts the influence of the external stress ratio, (τ_∞/s_0), ranging from 0.3 to 0.7, for

constant material parameter and modular ratio. The figure shows that an increase in the stress level will accelerate the damage process and result in a reduced elapsed time. Figure 4.18 demonstrates the effect of the modular ratio, H/G, ranging from 5.0 to 40.0, for constant stress level and material parameter. Contrary to the influence of material parameter and stress level, a decrease of the modular ratio, H/G, corresponds rather to a decrease in the elapsed time, as displayed by Figure 4.18. These findings are reiterated in Figures 4.19 thru 4.22. The variations of the elapsed time required for the onset of crack growth, t_i, and the elapsed time required for failure, t_f, with external stress, $\tau_{\_}$, are depicted in Figures 4.19 and 4.20, respectively. The stress level, $(\tau_{\_}/s_0)$, is shown versus t_i and t_f, for different values of material parameter, $(\beta s_0 a_0/G)$, ranging from 2.0 to 16.0, for H/G=10. The influence of the external stress ratio, $(\tau_{\_}/s_0)$, on the elapsed time to the onset of crack growth, t_i, and the elapsed time to failure, t_f, is demonstrated in Figures 4.21 and 4.22, respectively. The material parameter, $(\beta s_0 a_0/G)$, is shown versus t_i and t_f, for H/G=10.0. Figures 4.16 thru 4.22 reveal that the elapsed time required for the onset of crack growth, t_i, and the elapsed time required for failure, t_f, reduce when there is an increase in the external stress ratio, $(\tau_{\_}/s_0)$, and/or the material parameter, $(\beta s_0 a_0/G)$. On the other hand, when H/G decreases, there will be a faster reach to the onset of crack growth time, t_i, and the elapsed time required to cause failure, t_f.

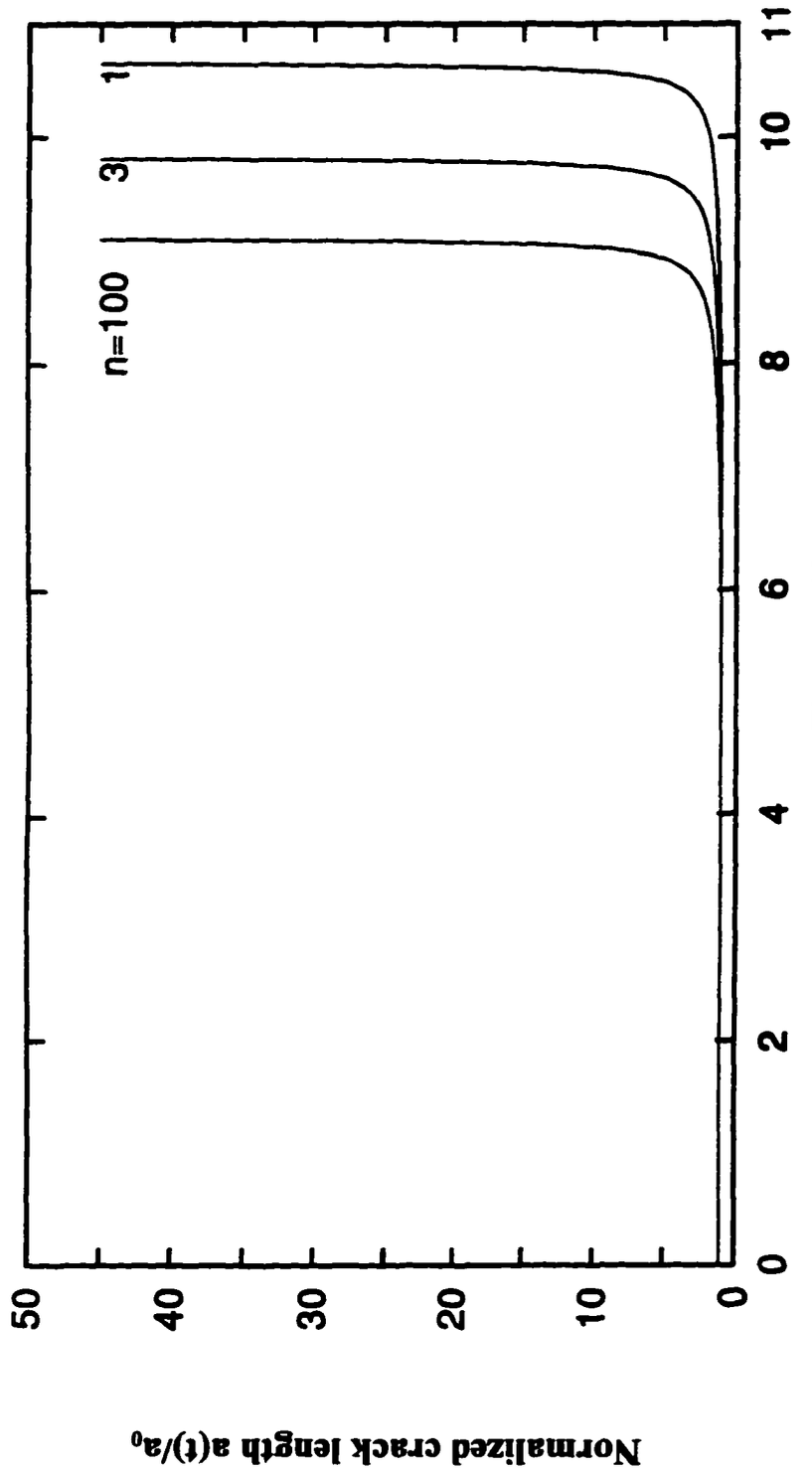

Figure 4.4 Crack growth due to steady-state creep at $\tau_{\infty}/s_0 = 0.4$, H/G = 40 and $\beta s_0 a_0 /G = 8$.

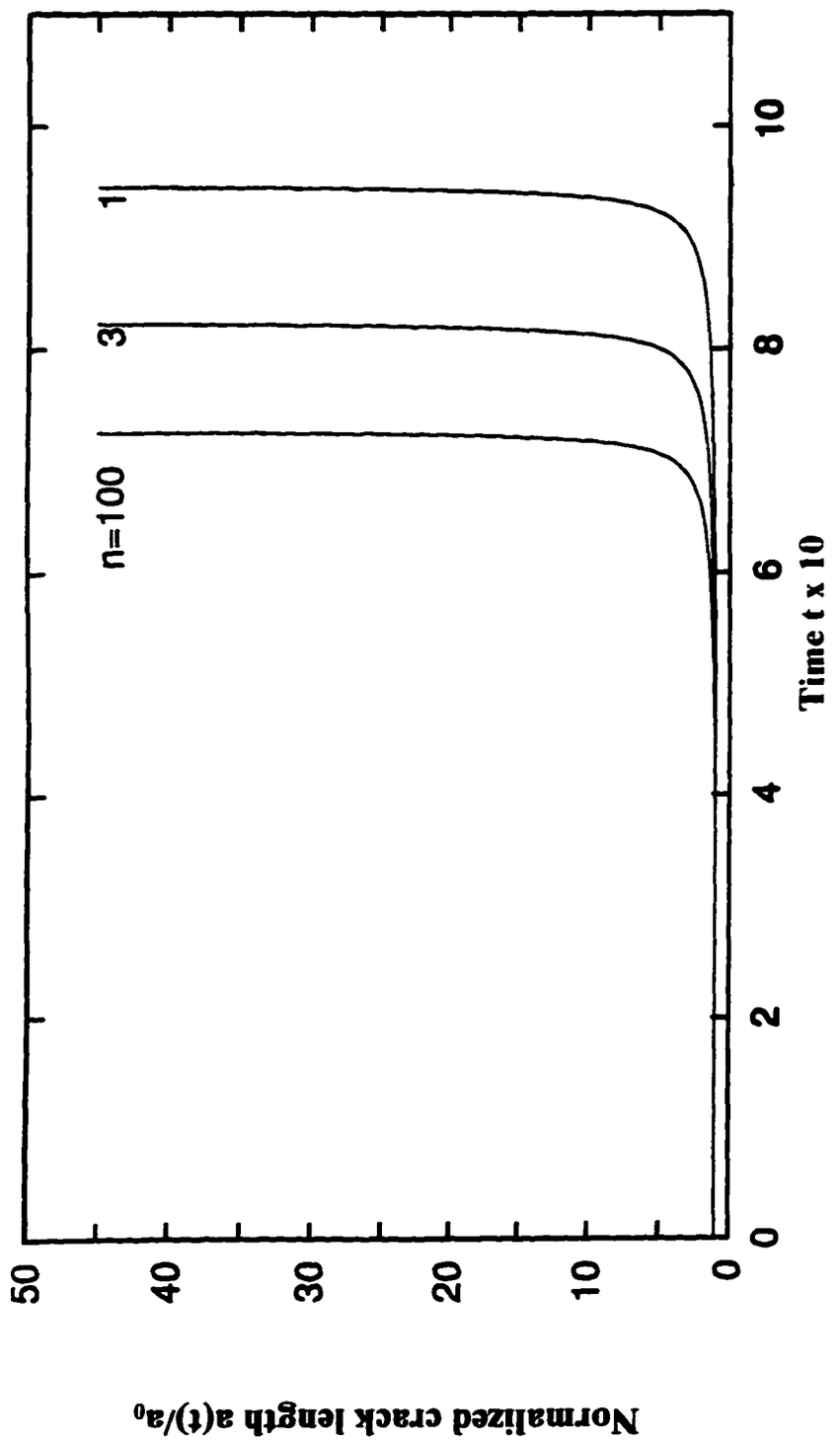

Figure 4.5 Variation of time versus normalized crack length at $\tau_{-}/s_0 = 0.4$, $H/G = 40$ and $\beta s_0 a_0 / G = 16$.

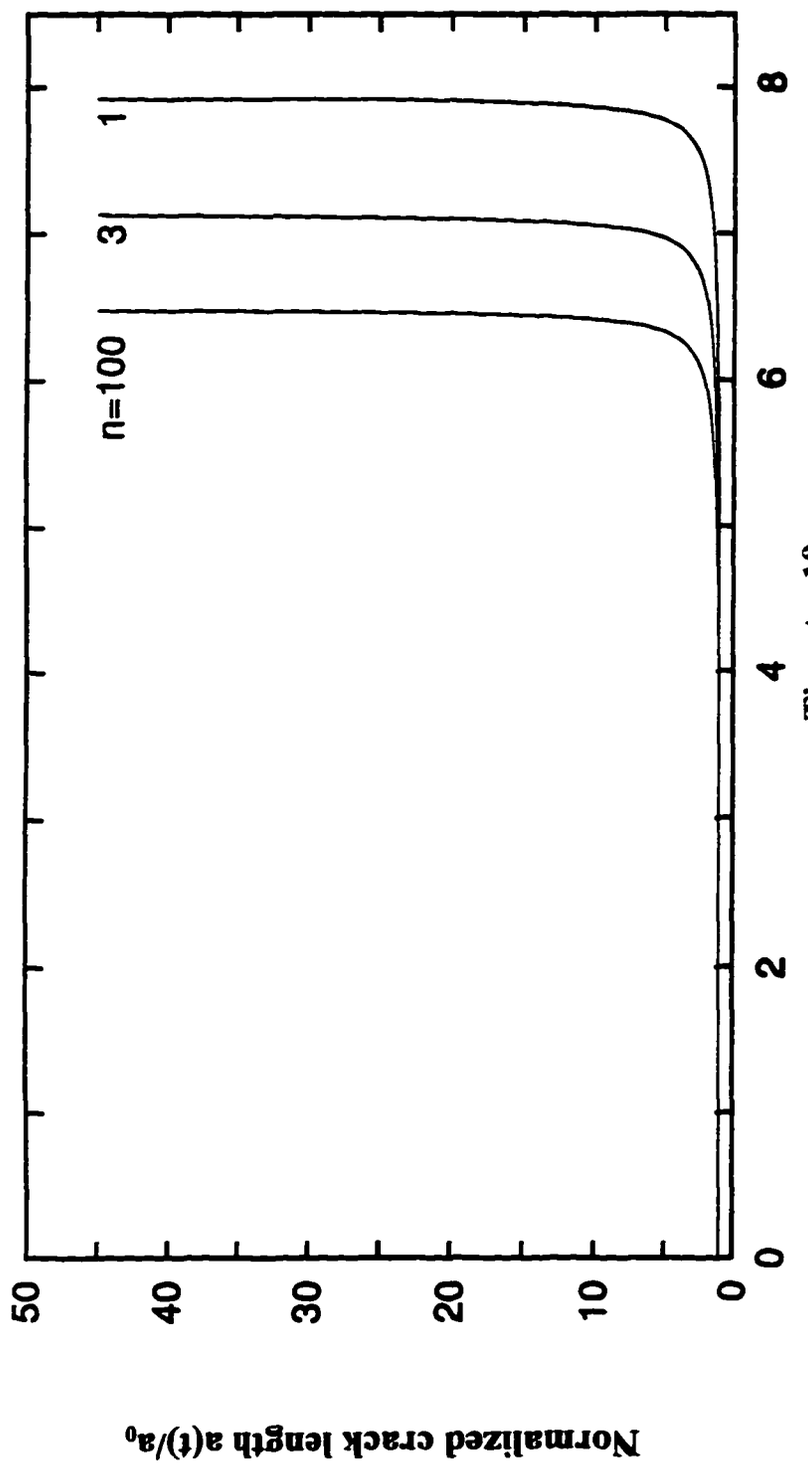

Figure 4.6 Influence of creep exponent on crack growth at $\tau_{\infty}/s_0 = 0.5$, $H/G = 40$ and $\beta s_0 a_0 / G = 8$.

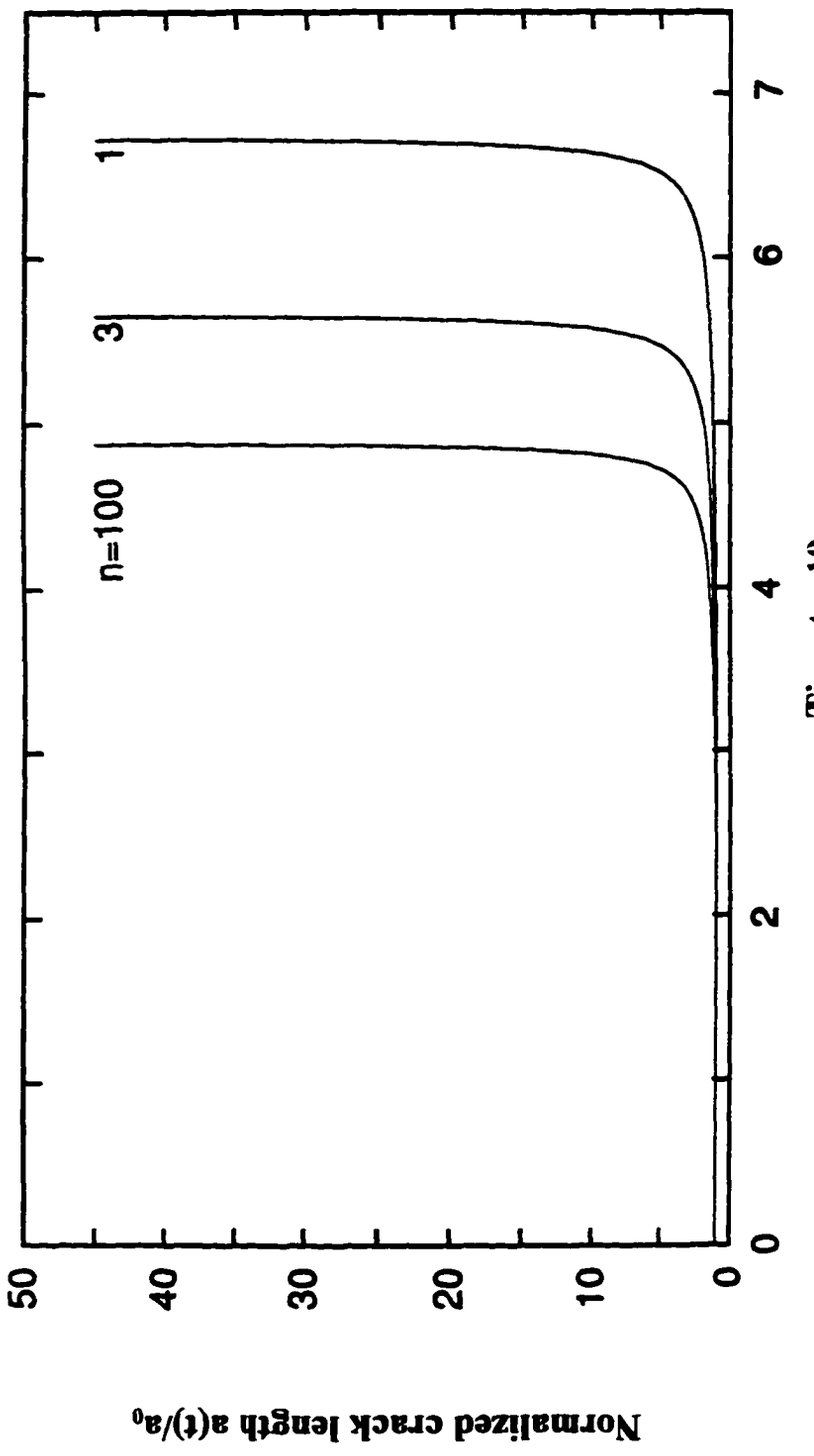

Figure 4.7 Steady-state creep crack growth at $\tau_\infty/s_0 = 0.5$, H/G = 20 and $\beta s_0 a_0 /G = 8$.

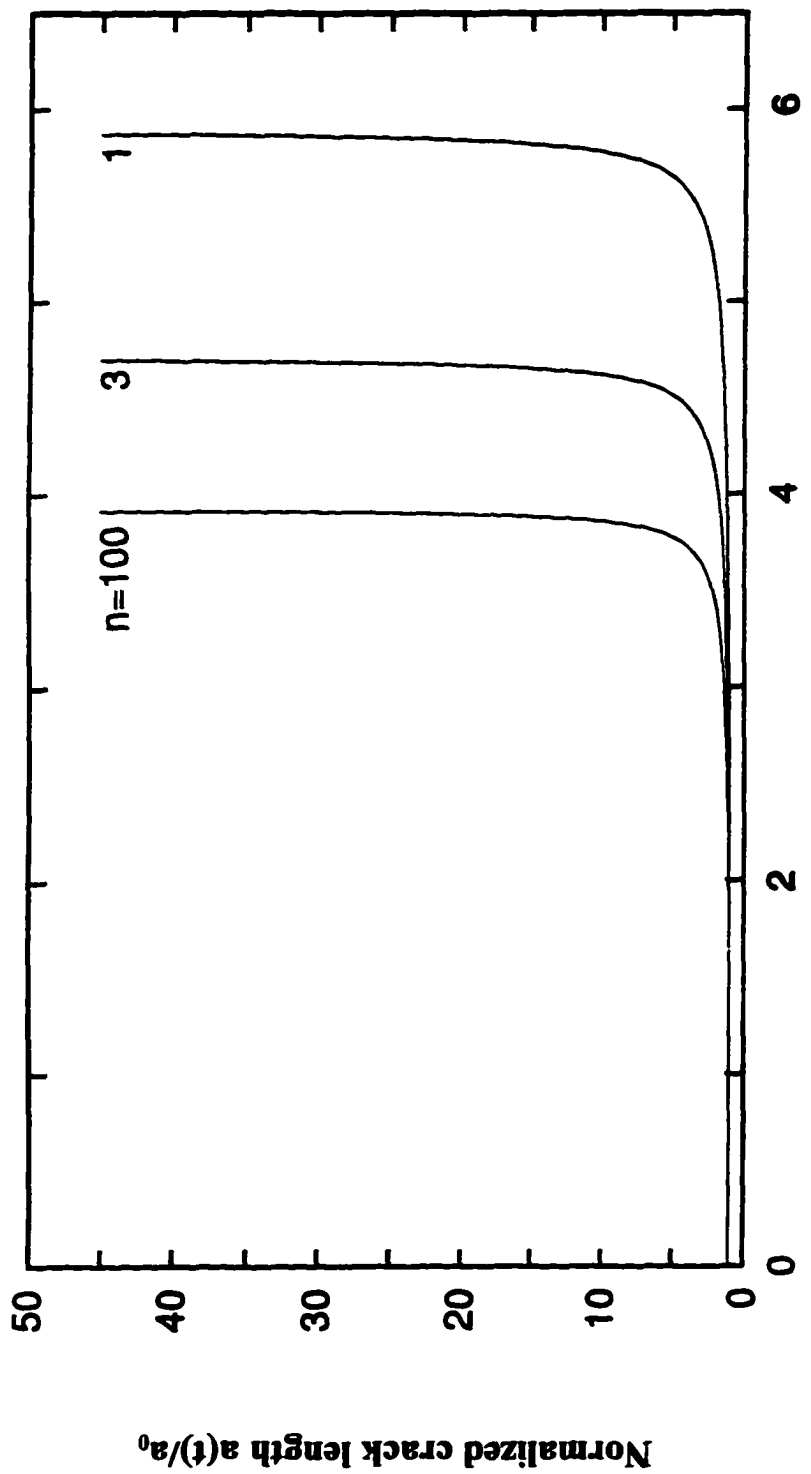

Figure 4.8 Variation of time versus normalized crack length at $\tau_{-}/s_0 = 0.5$, H/G = 10 and $\beta s_0 a_0 /G = 6$.

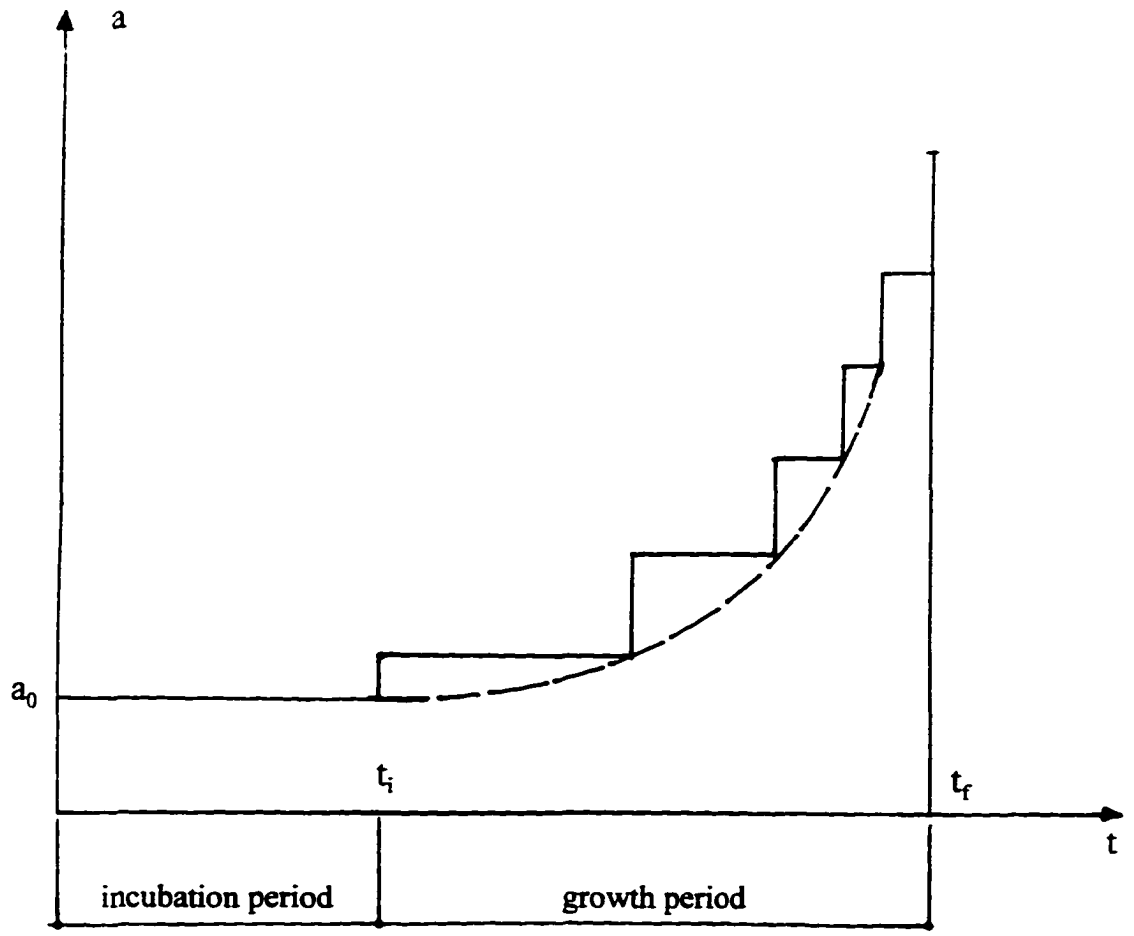

Figure 4.9 Principal appearance of the incubation and growth periods.

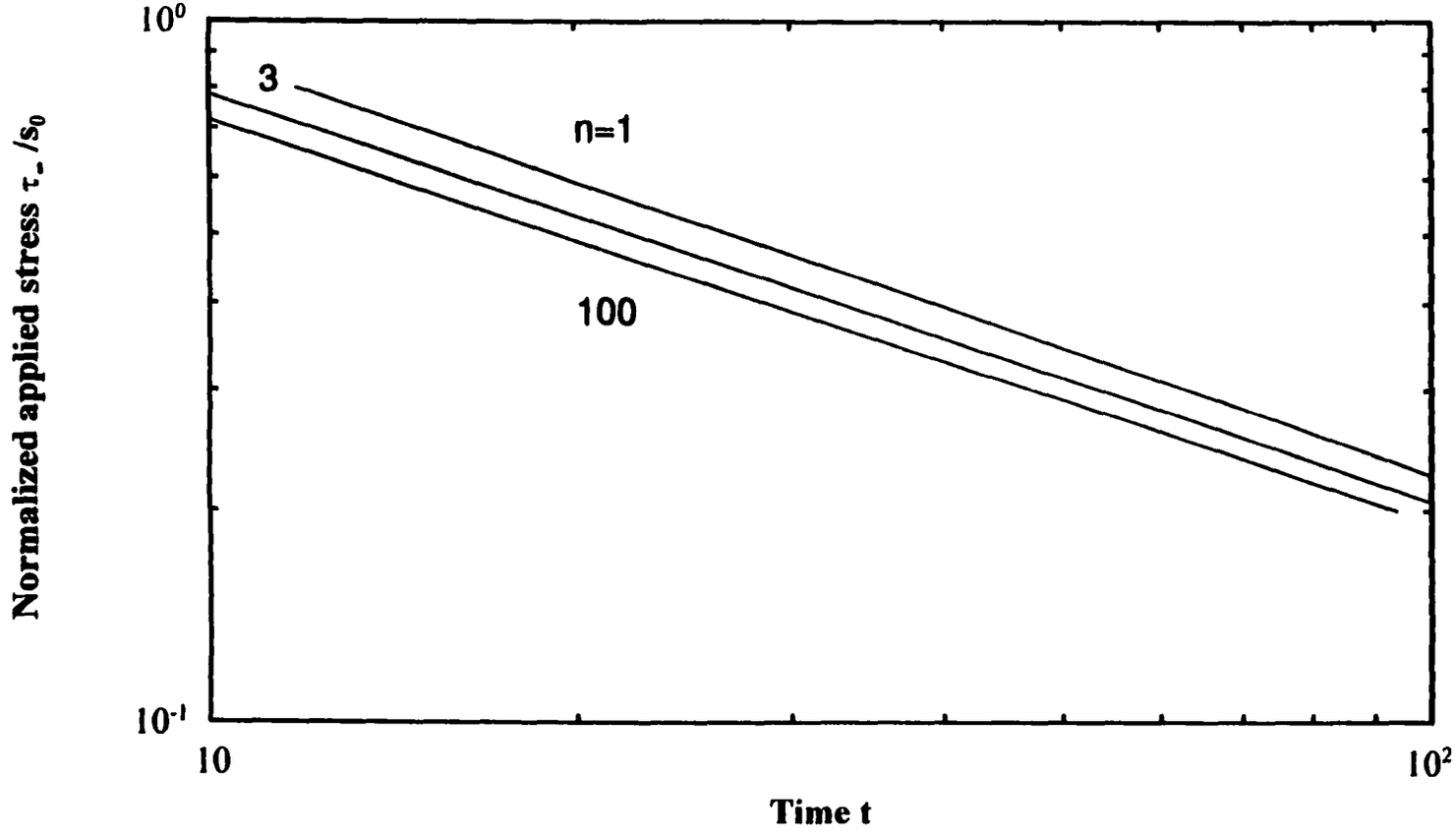

Figure 4.10 Influence of creep exponent on the elapsed time to the onset of crack growth at H/G = 10 and $\beta s_0 a_0 / G = 6$.

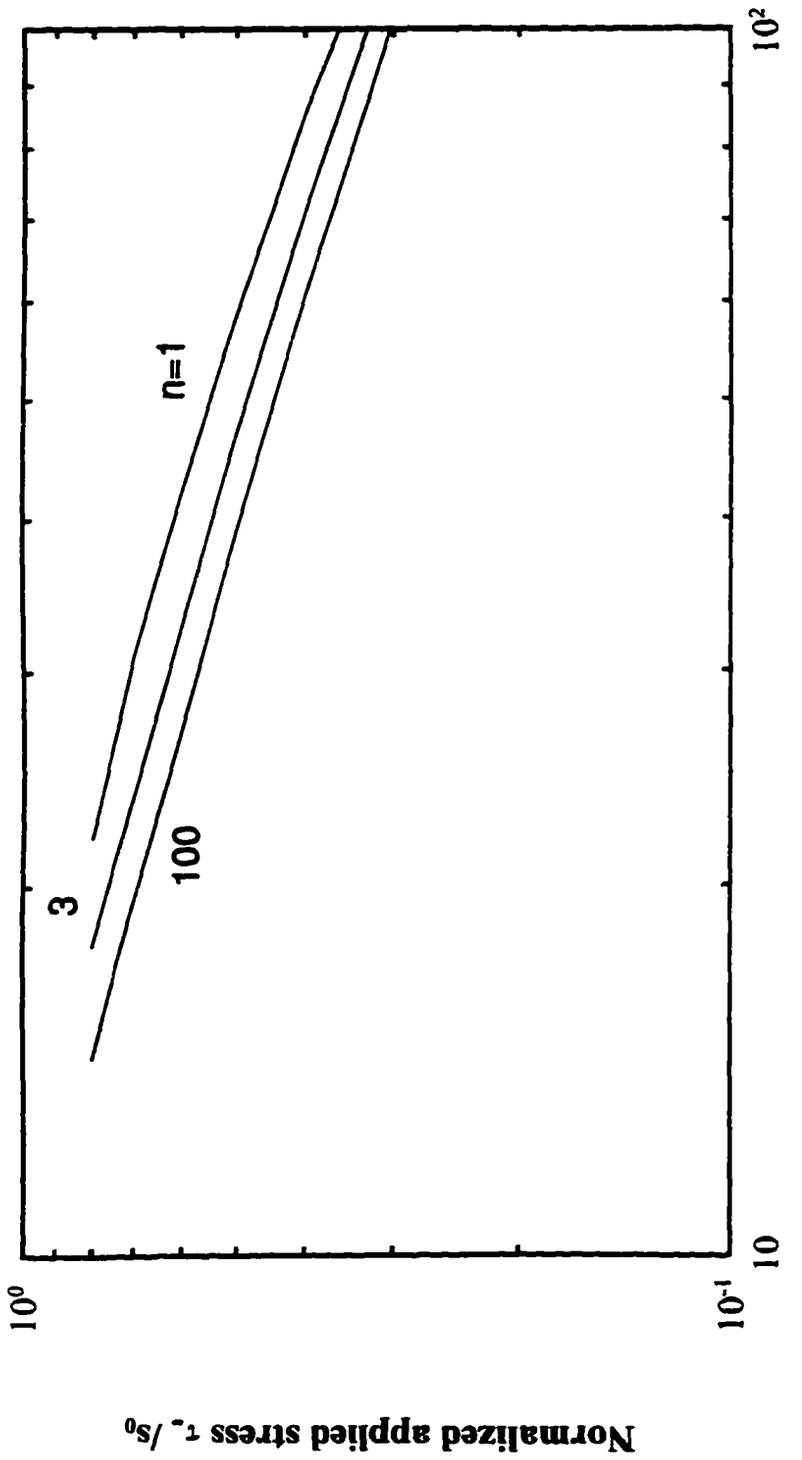

Figure 4.11 Elapsed time to failure versus external stress ratio at H/G = 10 and $\beta s_0 a_0 /G = 6$.

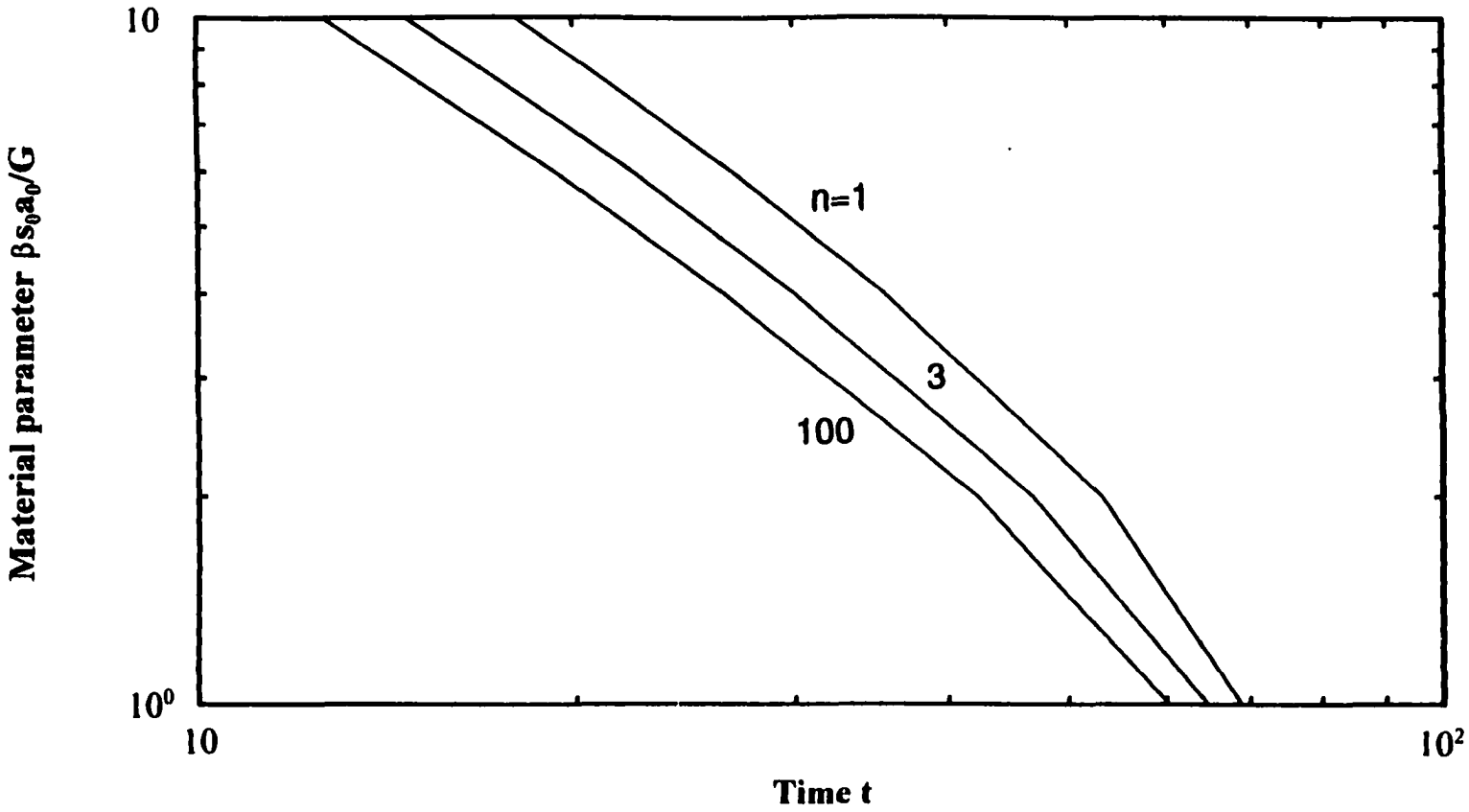

Figure 4.12 Variation of the material parameter, $\beta s_0 a_0 /G$, versus elapsed time to the onset of crack growth at $\tau_{..}/s_0 = 0.5$ and $H/G = 10$.

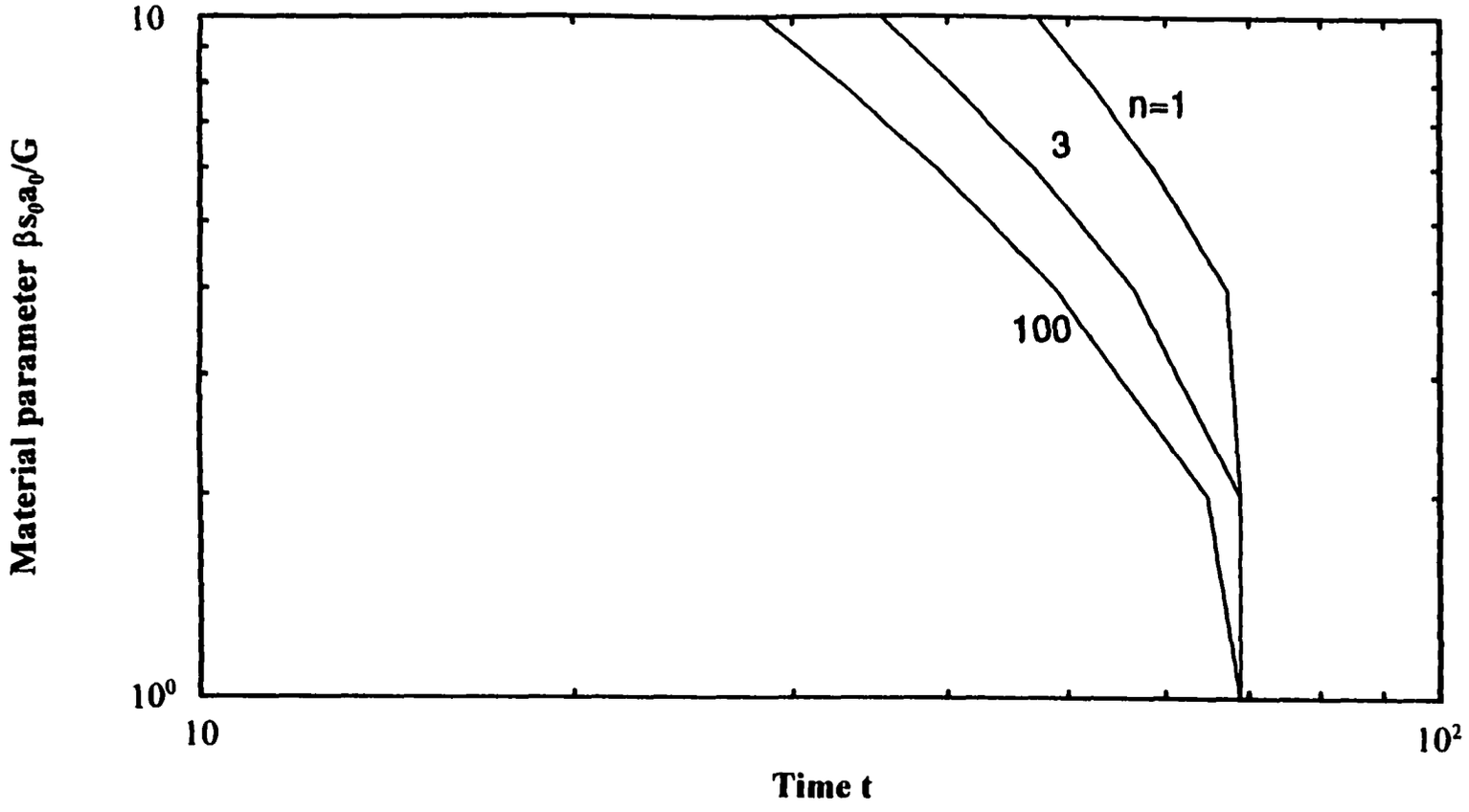

Figure 4.13 Influence of creep exponent on the elapsed time to failure at $\tau_a/s_0 = 0.5$ and H/G = 10.

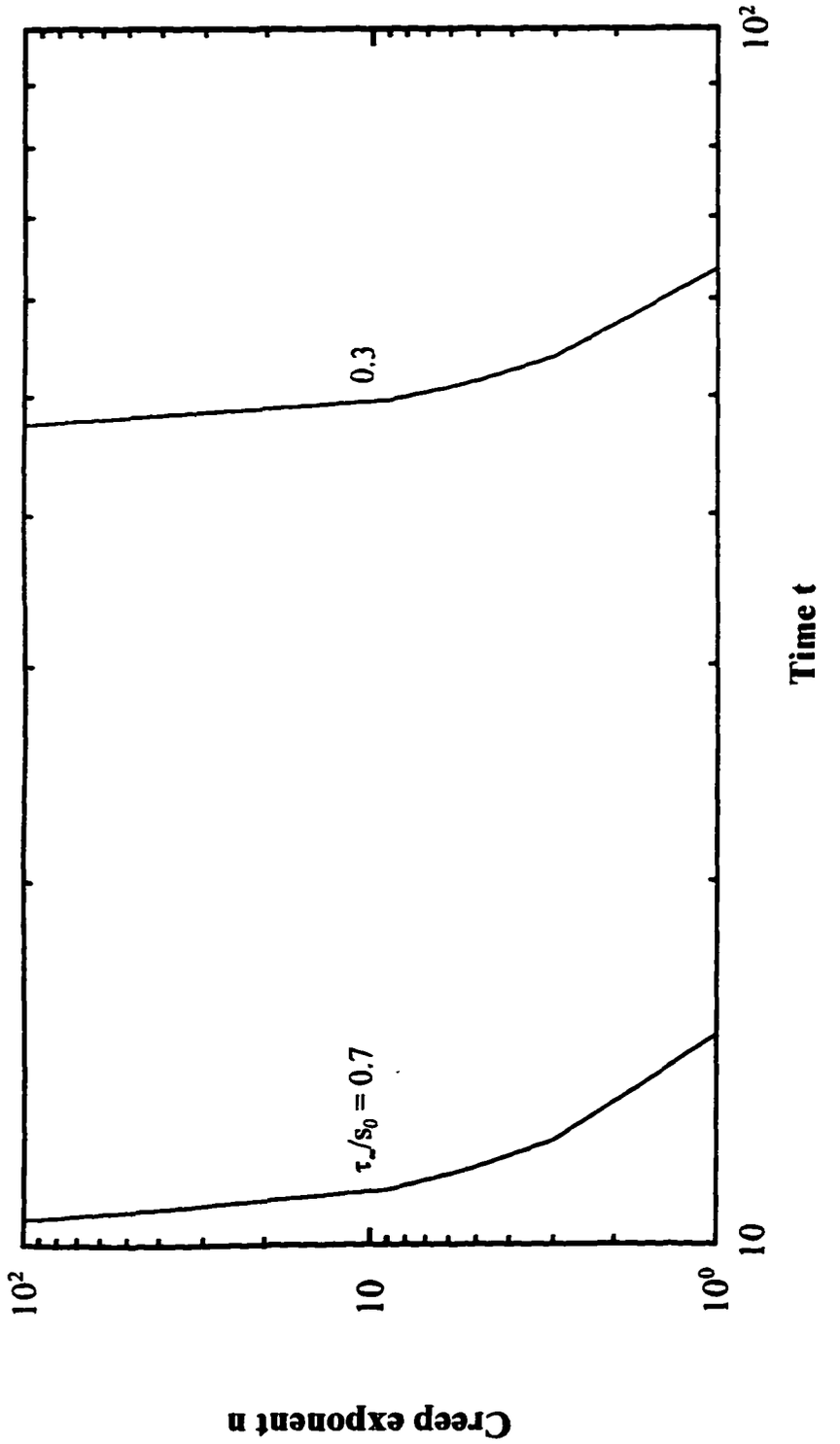

Figure 4.14 Variation of the creep exponent versus time to the onset of crack growth at H/G = 10 and $\beta s_0 a_0$ /G = 6, for $\tau_*/s_0 = 0.3$ and $\tau_*/s_0 = 0.7$.

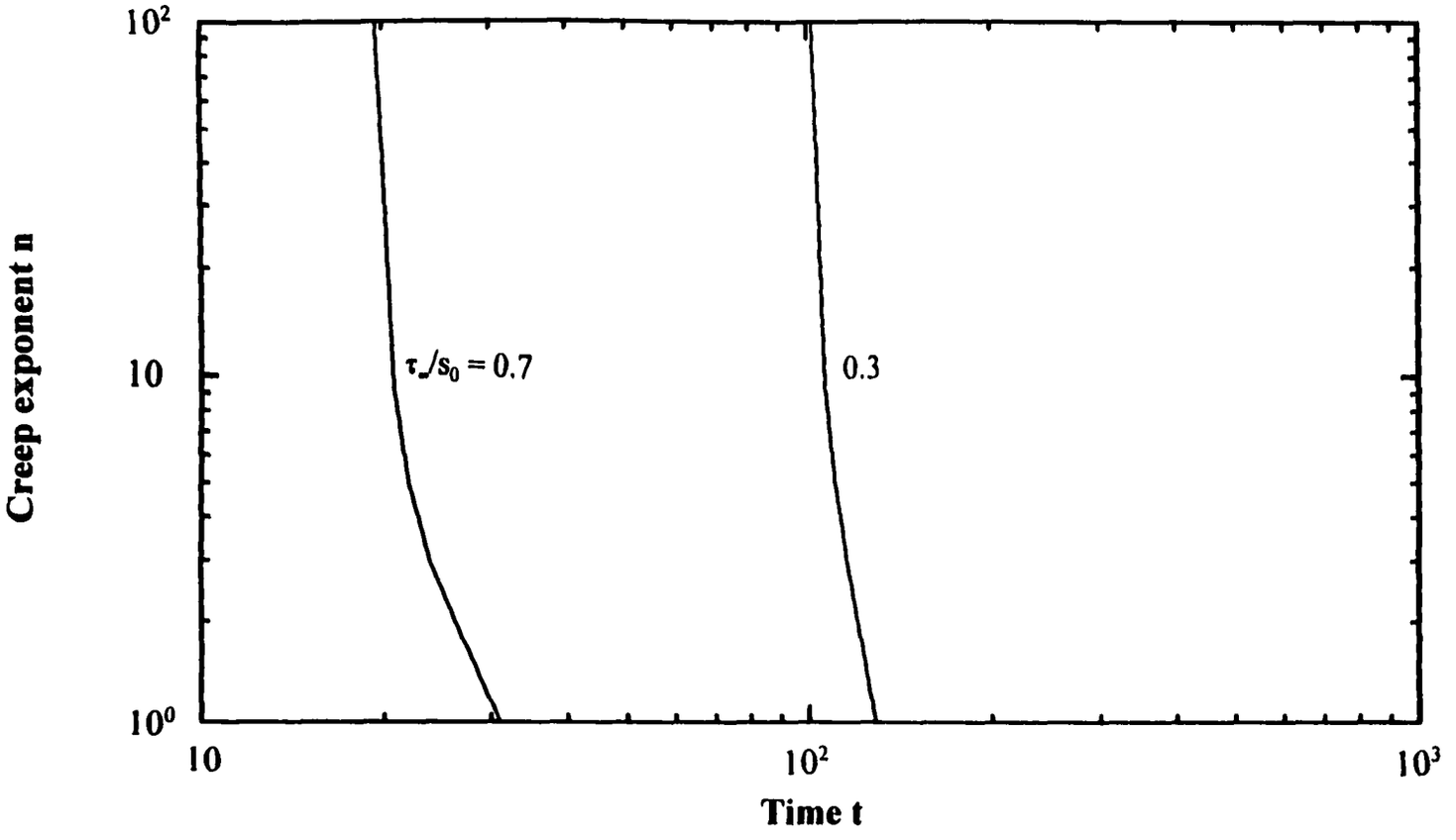

Figure 4.15 Influence of external stress ratio on the variation of creep exponent versus time to failure at H/G = 10 and $\beta s_0 a_0 /G = 6$.

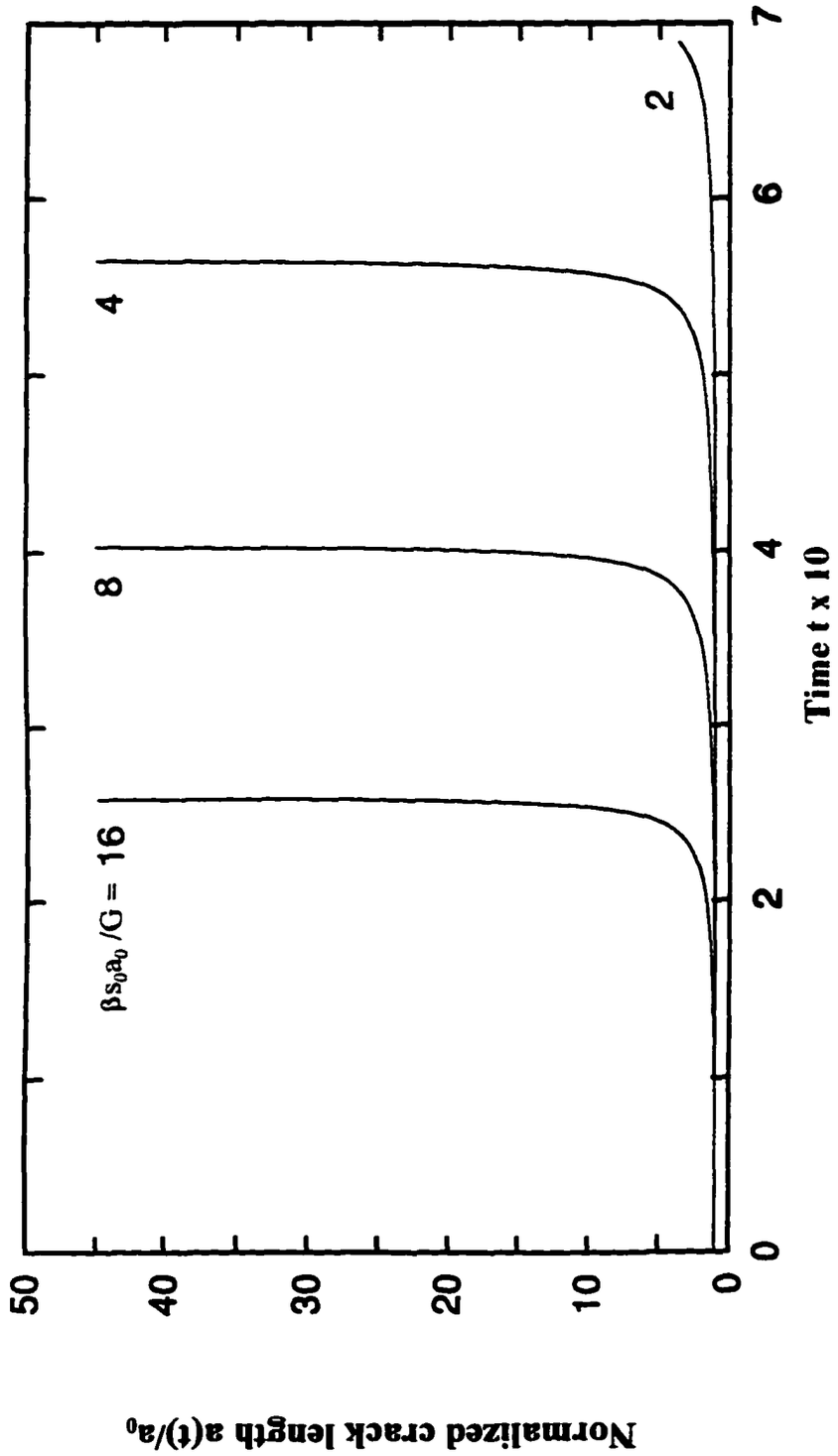

Figure 4.16 Influence of the material parameter, $\beta s_0 a_0 /G$, on creep crack growth at $\tau_\infty/s_0 = 0.5$ and H/G=10, for n = 3.

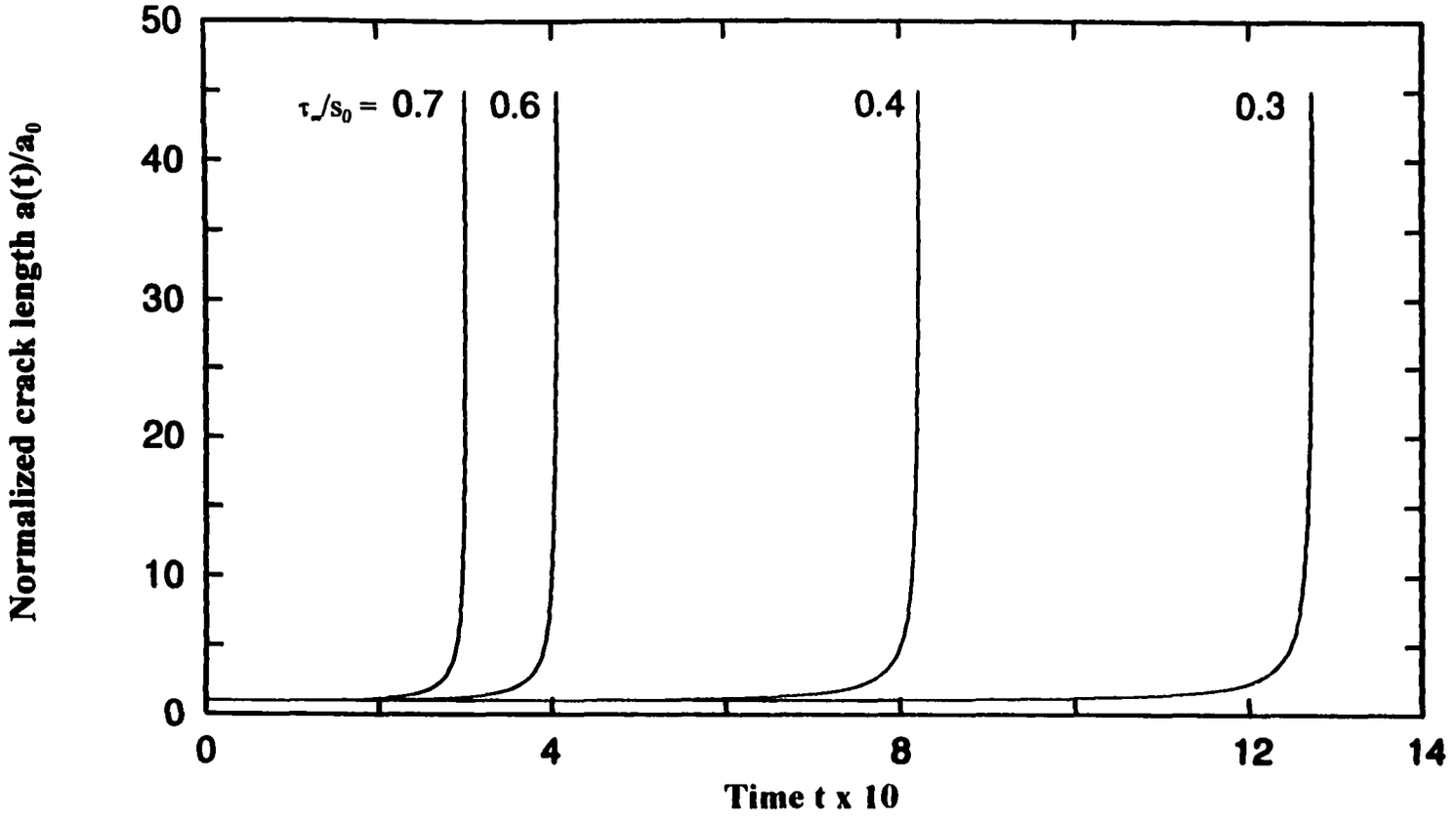

Figure 4.17 Creep crack growth corresponding to different external stress ratios at H/G = 10 and $\beta s_0 a_0 / G = 4$, for n = 3.

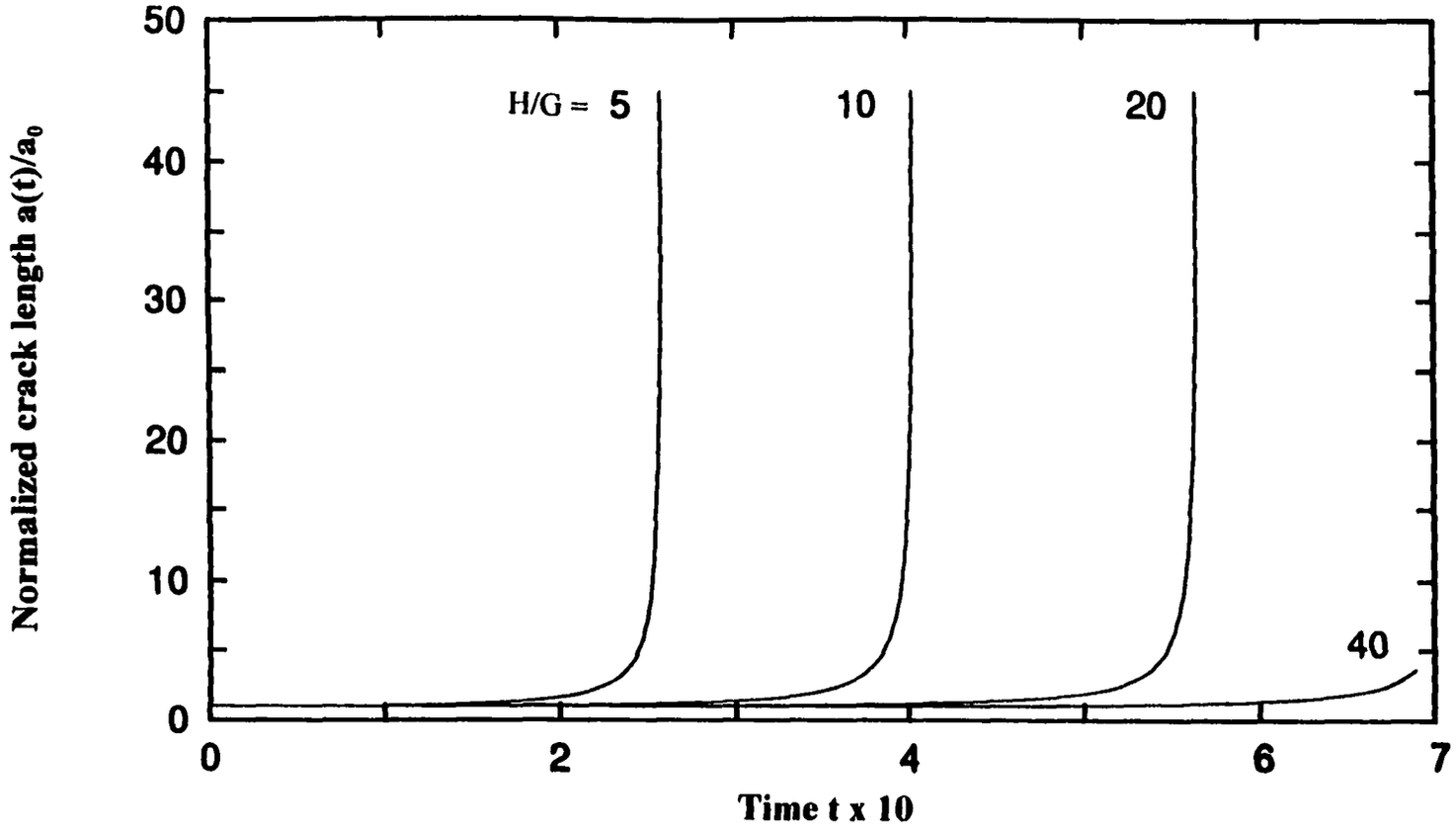

Figure 4.18 Variation of time versus normalized crack length due to different values of H/G at $\tau_{\infty}/s_0 = 0.5$ and $\beta s_0 a_0 / G = 8$, for $n = 3$.

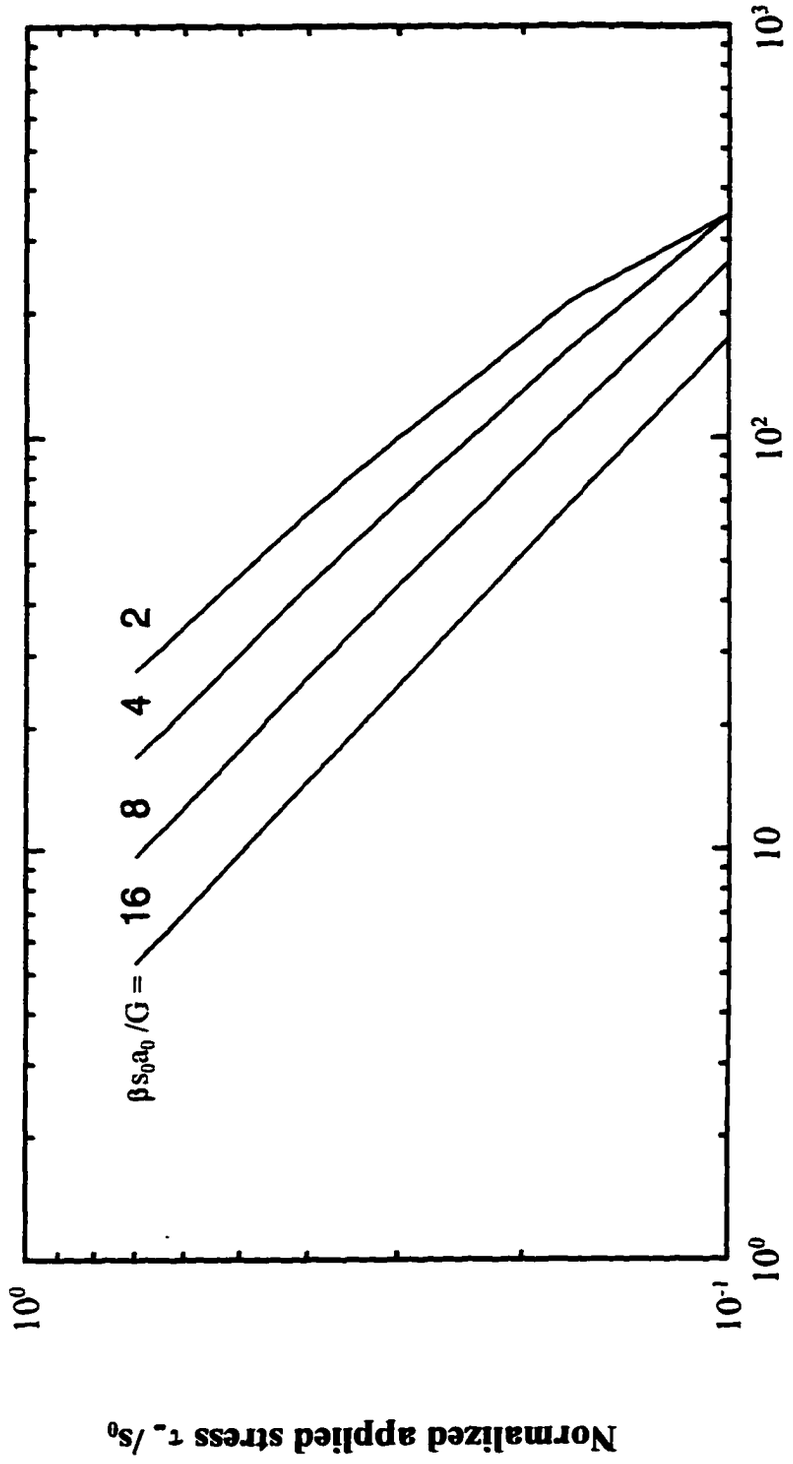

Figure 4.19 Influence of material parameter, $\beta s_0 a_0/G$, on elapsed time to the onset of crack growth at H/G = 10, for n=3.

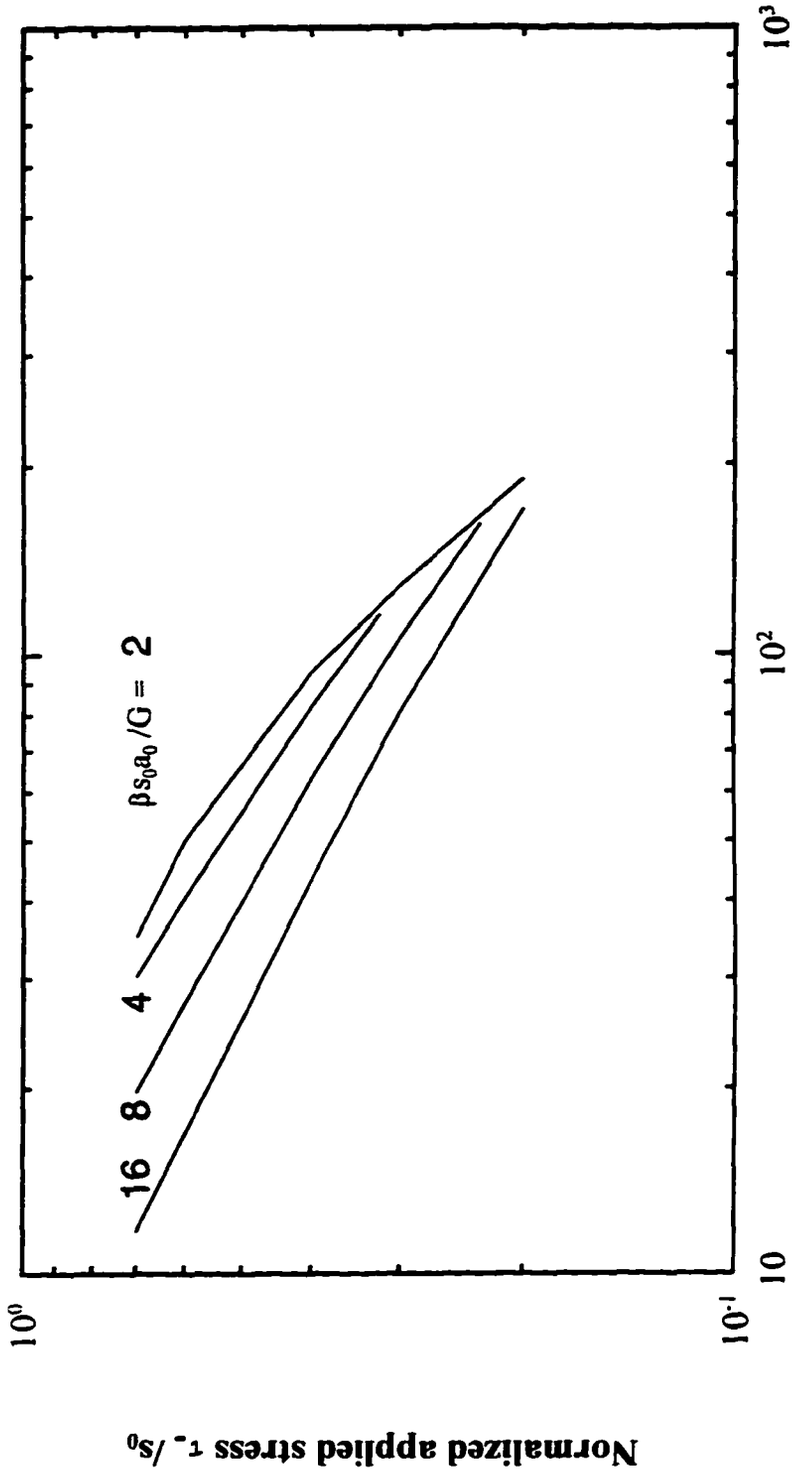

Figure 4.20 Elapsed time to failure versus external stress ratio at different values of the material parameter, $\beta s_0 a_0 /G$, for n=3.

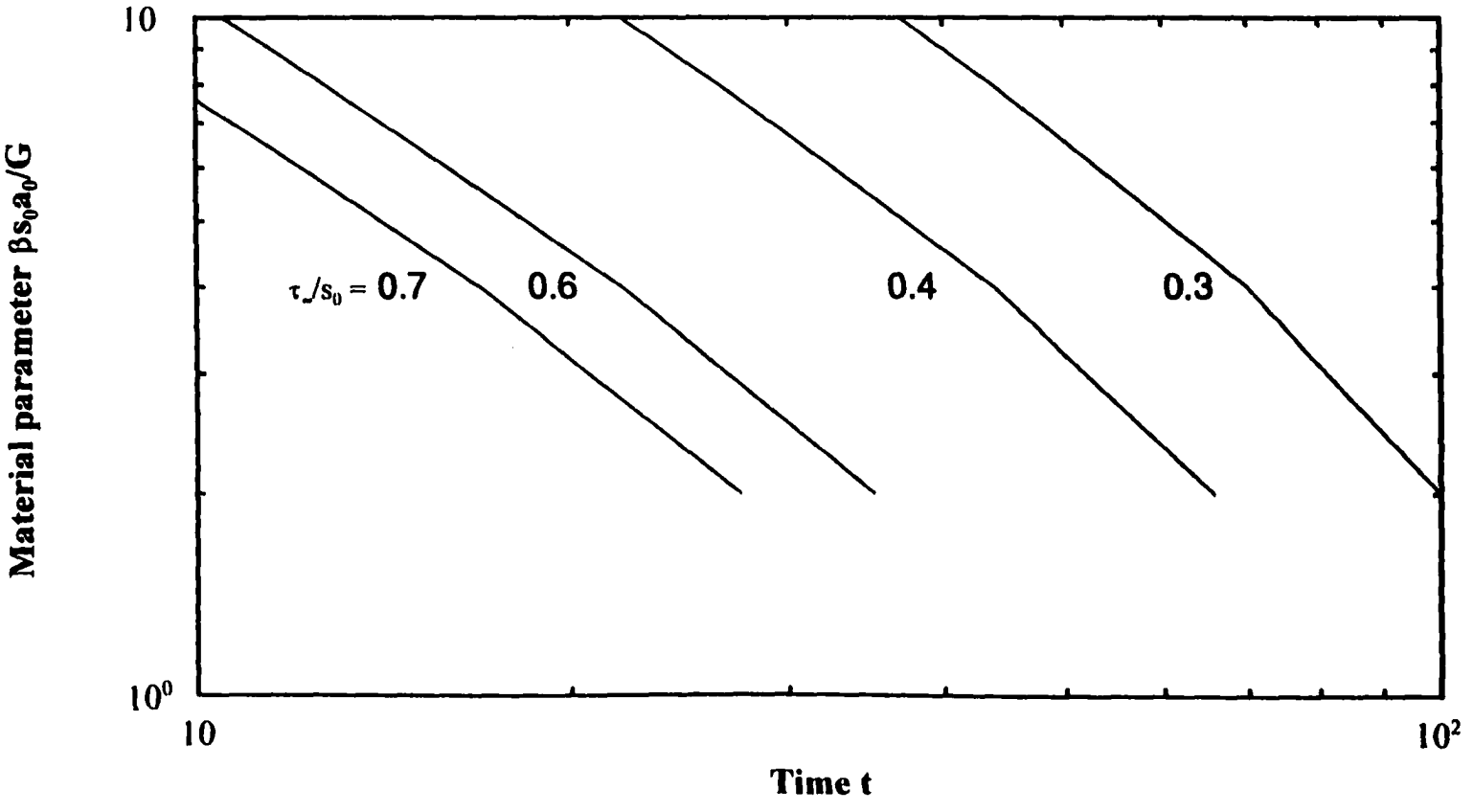

Figure 4.21 Material parameter, $\beta s_0 a_0 /G$, versus time to the onset of crack growth due to different external stress ratios, at H/G = 10, for n=3.

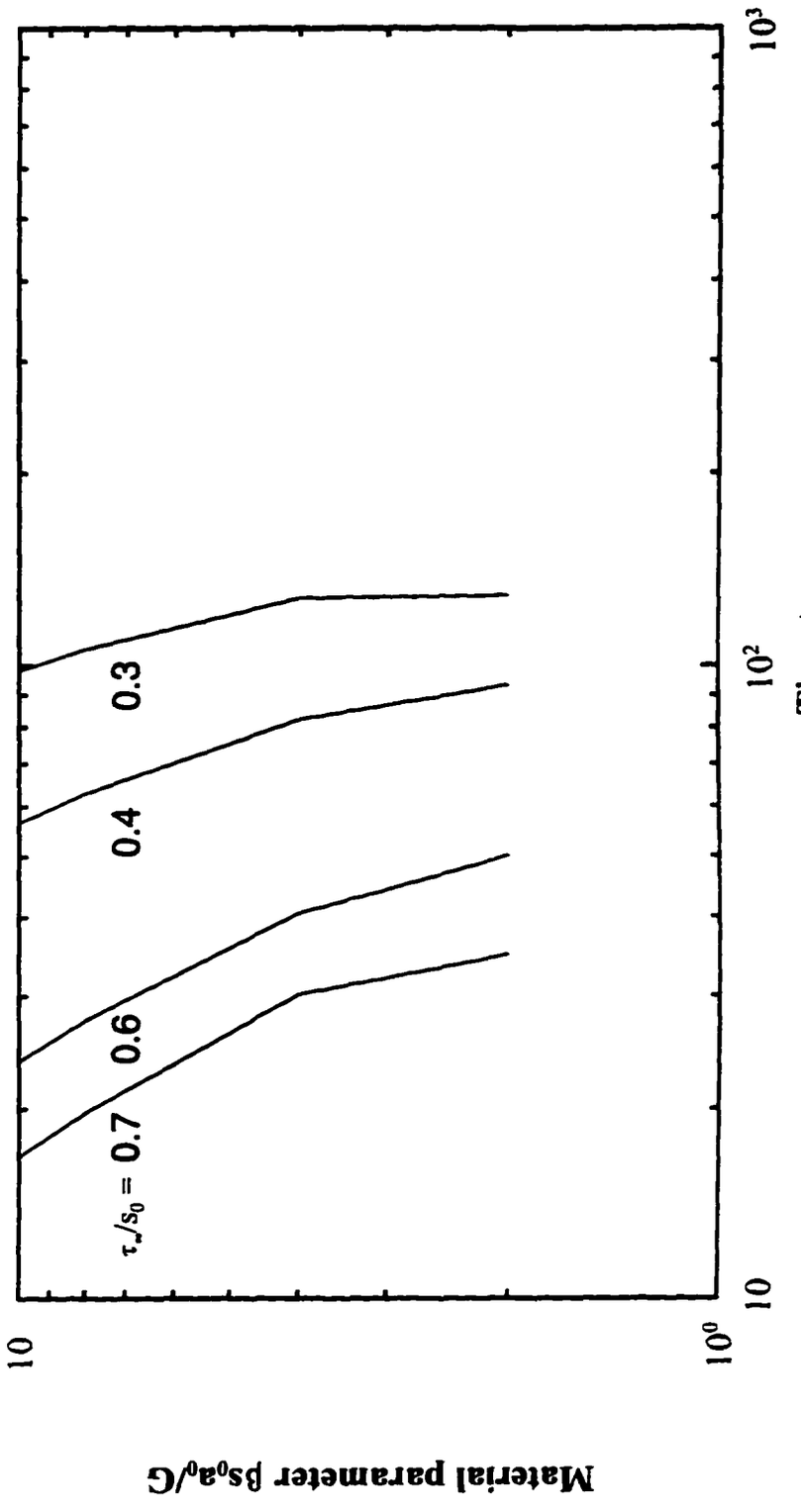

Figure 4.22 Influence of external stress ratio, τ_∞/s_0, on elapsed time to failure at H/G = 10 for n=3.

4.4.2 Theoretical Instability Time

Considering the fact that the crack grows into the material at all the time with damage D_0, the theoretical instability time, t_R, is obtained by setting $s_- = s_0$. Using equations (4.7) and (4.10), it follows that:

$$t_R = [\,1 - (\tau_- / s_0)^{(\theta+1)}\,] / [\,(\theta + 1)\,\kappa\,(\tau_- / s_0)^{\theta}\,] \qquad (4.23)$$

The instability time in equation (4.23), does not depend on the existence of a crack but is purely a creep phenomenon satisfying the assumption that the crack growth is not influencing the external stress. The instability time, t_R, is shown as the top curve in Figure 4.23, where log (τ_-/s_0) is plotted versus log t_R, for material parameters $(\beta s_0 a_0/G) = 6.0$, $H/G = 10.0$, $\kappa = .01$ and $\theta = 0.8$. However, for high values of $(\beta s_0 a_0/G)$, low values of H/G, and/or high external stress, the crack grows to very large size compared with the initial crack length before the theoretical instability time, t_R, is reached. Therefore, t_R is not a relevant measure of the fracture time, because a real, macroscopic crack seldom has the possibility to grow to such large size under a state of constant stress. Considering this fact, log (τ_- / s_0) is plotted versus log t_2, for different values of the creep constant, n=1 to n=100, in Figure 4.23, where t_2 is the time needed to double the initial crack length, i.e., $a(t_2)=2\,a_0$. It is interesting to note that a longer time is required to double the initial crack length for reduced values of the creep exponent, a readily established fact of the previous analysis. It is also clear that the dependence of the time t_2 on the creep exponent, n, is very mild. On the other hand, the theoretical time t_R is independent of the creep exponent, n, as indicated in equation 4.23. It should be noted that the theoretical time curve in Figure 4.23 envelopes the curves corresponding to different values of n. Upon further examination of Figure 4.23, it is worth

noting that at high stresses, the crack growth instability dominates, but at low stresses the creep damage instability prevails.

A theoretical instability time curve and also the time t_2 required to double the initial crack length are plotted versus the external load ratio, (τ_∞ / s_0), to show the influence of different material parameters for a creep exponent, n = 3, in Figure 4.24. An important aspect shown in Figure 4.24, is the influence of the material parameter and the modular ratio. A decrease in the elapsed time is observed corresponding to an increase in the material parameter and/or a decrease in the modular ratio. The theoretical time curve in Figure 4.24 is the envelope of all the time curves generated for different material parameters.

It is interesting to note that the theoretical time curves in Figures 4.23 and 4.24 have an asymptotic slope of $-1/\hat{n}$ in the log-log plot when $t_R \rightarrow \infty$. It can be shown using equation (4.23), when $t_R \rightarrow \infty$, that:

$$d\,[\log(\tau_\infty / s_0)]\,/\,d(\log t_R) = -1/\hat{n} \qquad (4.24)$$

From equation (4.23) this condition is satisfied when $(\tau_\infty / s_0) \rightarrow 0$. In the present calculations the slope of the theoretical time curve is found to be -1.25. In mode I calculations, in Chapter 5, a different value for $\hat{n}$ is used to demonstrate the validity of equation (4.24).

The main conclusion of the analysis is that the continuous damage model considered in this dissertation, predicts creep rupture curves which are well known from creep rupture tests.

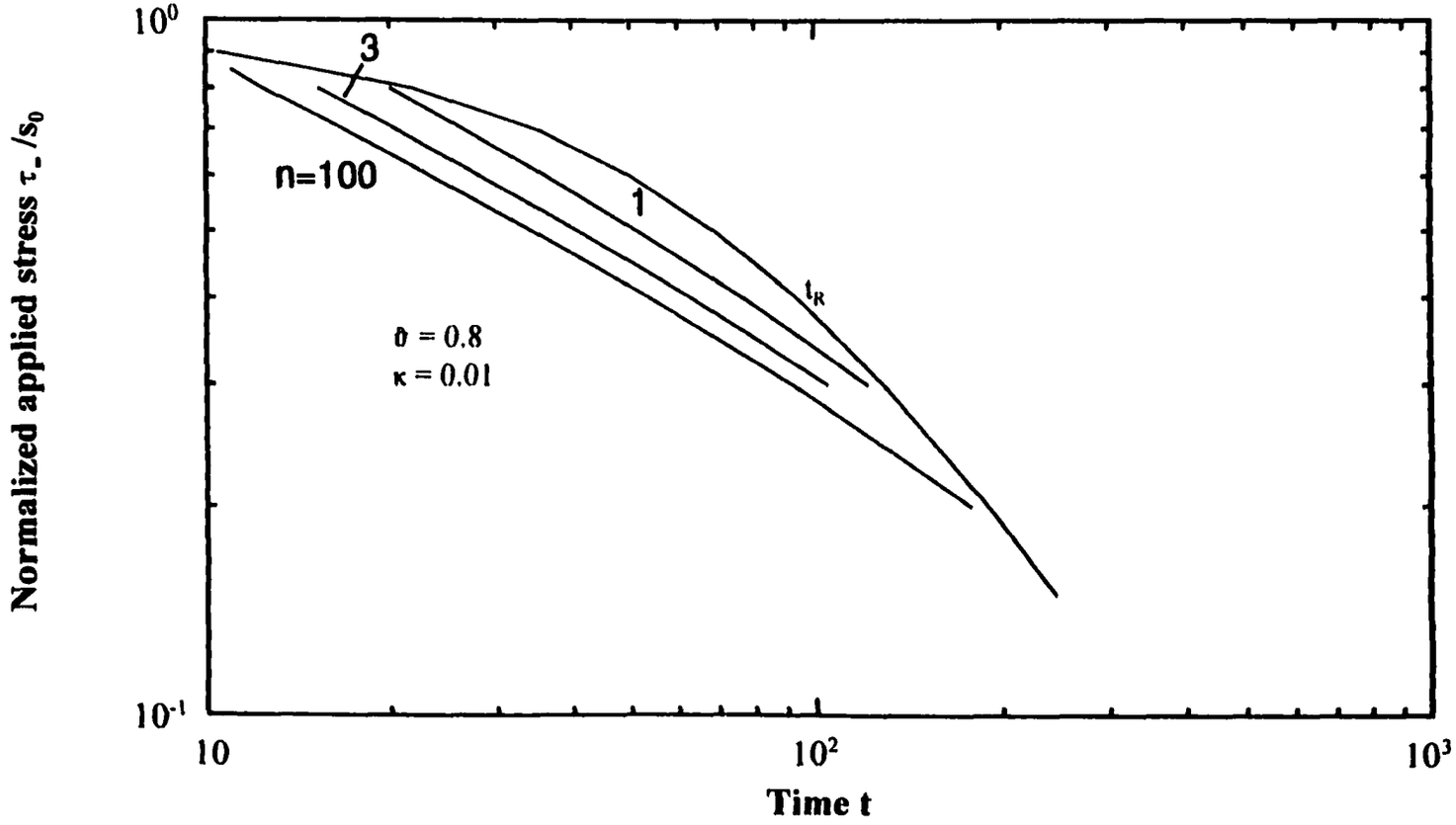

Figure 4.23 Influence of creep exponent on elapsed time needed to double the initial crack length at H/G = 10 and $\beta s_0 a_0 / G = 6$.

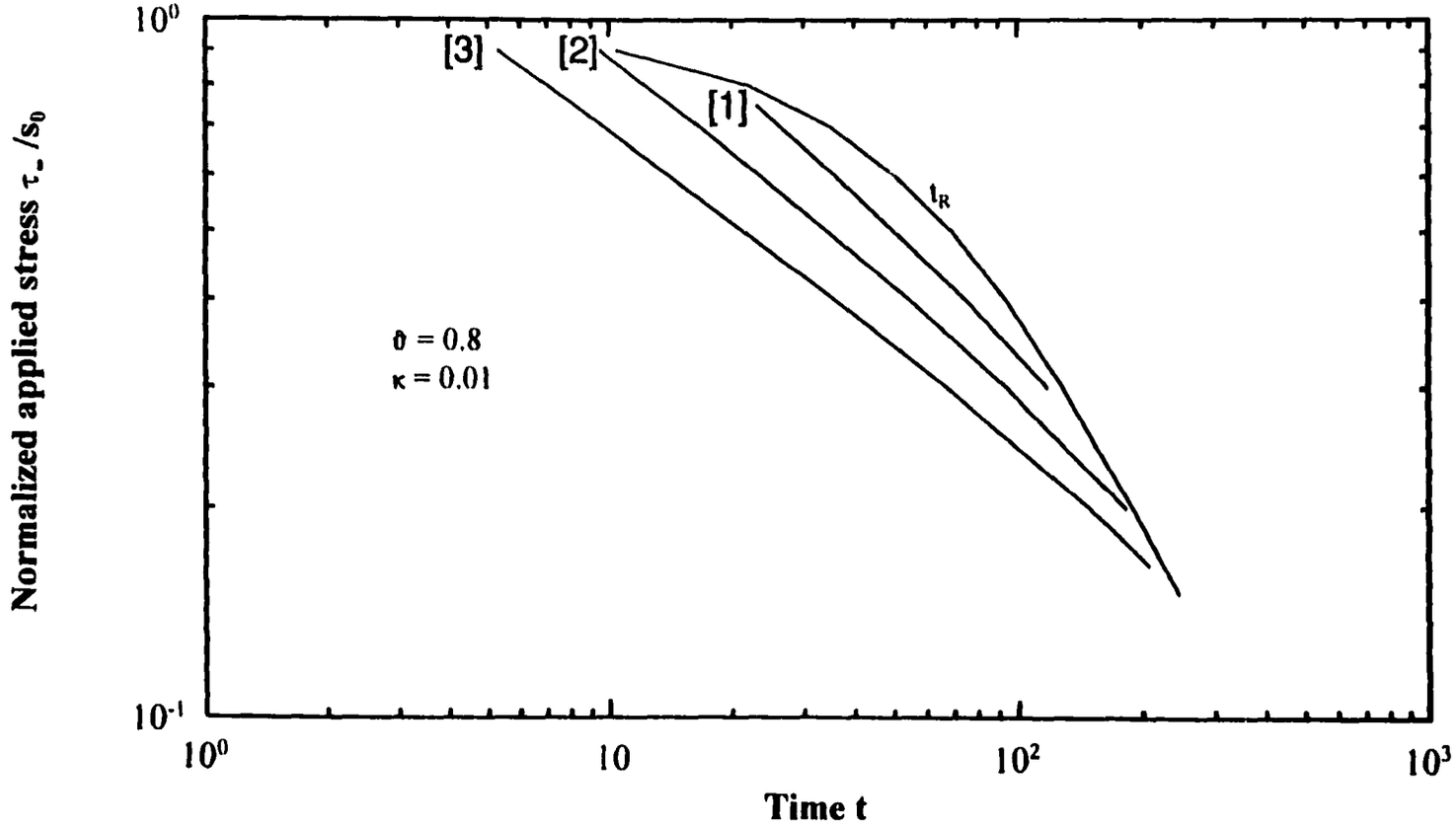

Figure 4.24 Influence of material parameters on elapsed time needed for doubling the initial crack length for n=3.
[1] $(\beta s_0 a_0 / G) = 4.0$ and $H/G = 10$.
[2] $(\beta s_0 a_0 / G) = 16.0$ and $H/G = 20$.
[3] $(\beta s_0 a_0 / G) = 16.0$ and $H/G = 10$.

5 DAMAGE FIELD FOR A CRACK SUBJECTED TO TENSILE LOADING (MODE I)

5.1 Introduction

This Chapter is concerned with the damage field near the tip of a stationary crack subjected to tensile loading under plane strain conditions. A material with a power hardening stress-strain relationship is considered. As mentioned previously, the strain concentration near the tip of a crack leads to nucleation, growth, and coalescence of microcracks or microvoids in the material and may lead to crack instability and growth. Consequently, the constitutive behavior of the material near the crack-tip becomes different from that of the material far away from the crack-tip. A damage variable, which represents the remaining load bearing area of the cross-section, is introduced to describe the mechanical effect of distributed microscopic damage. Damage is assumed to accumulate inside the plastic zone and cause the crack to grow and propagate. The constitutive equations of small-strain deformation theory of plasticity coupled with continuum damage and the appropriate boundary conditions are used to derive the governing equations. Since the governing differential equation is nonlinear, its integration has been performed numerically by treating the problem as an initial value one, and the leading term of the asymptotic expressions for displacement is determined.

Section 5.2 contains a brief summary of the basic mathematical equations required for the analysis. This follows closely the work of Hutchinson [12] and Rice and Rosengren [13]. Section 5.3 is concerned with the damaged material governing equations. In section 5.4, a

damage-zone is postulated as a circle, centered at the crack-tip. Section 5.5 describes the conditions necessary for the onset of crack instability under small-scale yielding and large-scale yielding conditions. A critical stress is determined as a function of crack length and a material parameter. The remotely applied stress, σ_∞, is found to be, like the anti-plane mode case, proportional to $a_0^{-1/(n+1)}$, where a_0 is half of the original crack length, and for n=1, this result reduces to Griffith's classical result. The developed criterion for crack instability is noted to depend on Poisson's ratio, ν. Section 5.6 deals with fatigue crack propagation under cyclic tensile loading. For given material parameters, the number of load cycles required for the onset of crack propagation, N_i, and the number of cycles required for failure, N_f, are determined. Section 5.7 describes time-dependent crack propagation under steady-state creep conditions. For specific material parameters, the elapsed time required to cause onset of crack growth, t_i, and the elapsed time required to cause failure, t_f, are determined.

5.2 Summary of Basic Equations

Consider a homogeneous body containing a traction free crack of length $2a_0$, subjected to a two dimensional deformation field under plain strain conditions, as shown in Figure 5.1, where all stresses depend on x and y only. In terms of polar coordinates, r and θ, measured from the crack-tip, the in-plane strain tensor, ε_{ij}, and the corresponding stress tensor, σ_{ij}, with i, j = r and θ, must satisfy the compatibility and equilibrium equations, namely:

$$r^{-2}(\partial^2 \varepsilon_{rr}/\partial\theta^2) - r^{-1}(\partial\varepsilon_{rr}/\partial r) + r^{-1}(\partial^2/\partial r^2)[r\varepsilon_{\theta\theta}] - 2r^{-2}(\partial/\partial r)[r\,\partial\varepsilon_{r\theta}/\partial\theta)] = 0 \quad (5.1)$$

and;

$$(\partial\sigma_{rr}/\partial r) + (1/r)(\partial\sigma_{r\theta}/\partial\theta) + (\sigma_{rr} - \sigma_{\theta\theta})/r = 0 \quad (5.2a)$$

$$(1/r)(\partial\sigma_{\theta\theta}/\partial\theta) + (\partial\sigma_{r\theta}/\partial r) + (2\sigma_{r\theta}/r) = 0 \quad (5.2b)$$

An elastic-plastic material obeying a linear relation to the yield point $(\sigma_0, \varepsilon_0)$ and a power-hardening law thereafter, namely:

$$\varepsilon/\varepsilon_0 = (\sigma/\sigma_0)^n \quad (5.3)$$

is assumed for the component. The yield stress, σ_0, and yield strain, ε_0, are related by $\sigma_0 = E\,\varepsilon_0$, with E being the Young's modulus and n is the strain hardening exponent. The stress-strain relationship is expressed as:

$$\varepsilon_{ij} = [(1+\nu)\varsigma_{ij}] + [(1-2\nu)\sigma_{kk}\delta_{ij}/3E] \quad , \quad \varepsilon < \varepsilon_0 \quad (5.4a)$$

$$\varepsilon_{ij} = [(1+\nu)\varsigma_{ij}] + [(1-2\nu)\sigma_{kk}\delta_{ij}/3E] + \{[3\varepsilon_0\varsigma_{ij}/(2\sigma_0)][\sigma_e/\sigma_0]^{n-1}\} \quad , \quad \varepsilon > \varepsilon_0 \quad (5.4b)$$

where ς_{ij} and σ_e are the deviatoric stress and the von Mises equivalent stress given, respectively, by:

$$\varsigma_{ij} = \sigma_{ij} - (\sigma_{kk}/3)\,\delta_{ij} \quad (5.5)$$

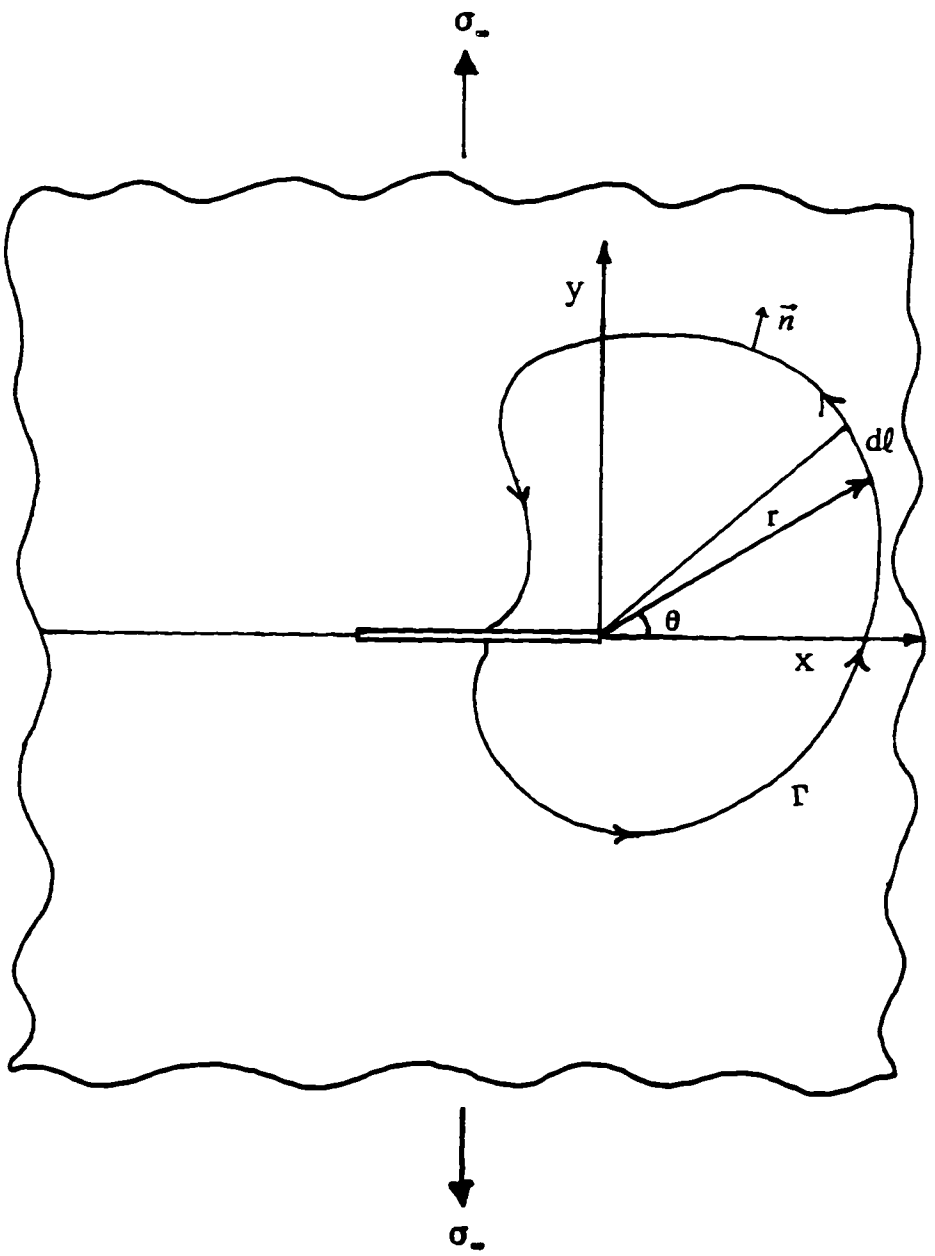

Figure 5.1 Notations at the crack-tip.

$$\sigma_e = \{ [(3/4)(\sigma_{rr} - \sigma_{\theta\theta})^2] + 3\sigma_{r\theta}^2 \}^{1/2} \quad (5.6)$$

where $(\sigma_{kk}/3)$ is the hydrostatic component of the stress tensor, δ_{ij}, is Kronecker delta and ν stands for Poisson's ratio. In the vicinity of the crack-tip, the elastic strain can be neglected and equation (5.4b) reduces to:

$$\varepsilon_{ij} = [3\varepsilon_0 \varsigma_{ij}/(2\sigma_0)][\sigma_e/\sigma_0]^{n-1} \quad (5.7)$$

The equilibrium equations are satisfied by introducing the usual Airy stress function, ω, where:

$$\sigma_{rr} = r^{-2}(\partial^2\omega/\partial\theta^2) + r^{-1}(\partial\omega/\partial r) \quad (5.8a)$$

$$\sigma_{\theta\theta} = \partial^2\omega/\partial r^2 \quad (5.8b)$$

$$\sigma_{r\theta} = (\partial/\partial r)[r^{-1}(\partial\omega/\partial\theta)] \quad (5.8c)$$

The partial differential equation governing the stress function, ω, can be obtained by eliminating the strains from the compatibility equation (5.1) after using equations (5.6) through (5.8). This yields:

$$\nabla^4\omega + \{r^{-2}(\partial^2/\partial\theta^2) - r^{-1}(\partial/\partial r) - r^{-1}[\partial^2(r)/\partial r^2]\}.\{\sigma_e^{n-1}[r^{-1}(\partial\omega/\partial r) + r^{-2}(\partial^2\omega/\partial\theta^2) - (\partial^2\omega/\partial r^2)]\}$$
$$+ 4r^{-2}(\partial/\partial\theta)\{(\partial/\partial r)[r\,\sigma_e^{n-1}(\partial/\partial r)(\partial\omega/\partial\theta)]\} = 0 \quad (5.9)$$

Equation (5.9) is solved over the interval $\theta \in [0, \pi]$, $r \in [0, \infty]$ subject to the boundary conditions which ensure a solution corresponding to symmetrical deformation relative to the crack line. Traction-free crack surfaces require $\sigma_{\theta\theta}$ and $\sigma_{r\theta}$ to vanish at $\theta = \pi$, so that :

$$\omega(\pi) = \omega'(\pi) \quad (5.10)$$

Symmetry of deformation requires that $\sigma_{r\theta}$, $\partial\sigma_{rr}/\partial\theta$, and $\partial\sigma_{\theta\theta}/\partial\theta$ all vanish at $\theta = 0$, leading to further requirements:

$$\omega'(0) = \omega'''(0) \quad (5.11)$$

Here, prime indicates differentiation with respect to the variable θ.

In order to obtain an asymptotic solution of equation (5.9), Hutchinson [12] introduced the following expression for the stress function, ω:

$$\omega = C_1(\theta)\, r^p + C_2(\theta)\, r^q \tag{5.12}$$

where C_1 and C_2 are constants that depend on θ, the angle from the crack plane, and p and q are arbitrary constants. He showed that [12] the dominant term assumes the form:

$$\omega = \varkappa\, \sigma_0 r^p\, \varpi(\theta) \tag{5.13}$$

where $\varkappa$ is the amplitude of the stress function and $\varpi(\theta)$ is a dimensionless function of θ. Except for its amplitude, $\varkappa$, the dominant term is determined entirely by the nonlinear terms in the governing differential equation (5.9). Formally, this follows from a substitution of equation (5.13) into (5.9). With the biharmonic term omitted, equation (5.9) is homogeneous in both ω and r and derivatives with respect to r. For this reason, an exact separation of the nonlinear terms in equation (5.9) is accomplished by the term assumed in (5.13). The resulting equation, which is homogeneous in ϖ and is associated with the homogeneous boundary conditions given is equations (5.10) and (5.11), is in the form of an eigenvalue equation for p:

$$[(\partial^2/\partial\theta^2)-n(p-2)\{n(p-2)+2\}].[\tilde{\alpha}^{n-1}\{p(2-s)\varpi(\theta)+\varpi''(\theta)\}] + 4(p-1)\{n(p-2)+1\}(\tilde{\alpha}^{n-1}\varpi'(\theta))' = 0 \tag{5.14}$$

where:

$$\tilde{\alpha}(\theta) = \{(3/4)[\varpi'' - p^2\varpi]^2 + 3[(1-p)\varpi']^2\}^{1/2} \tag{5.15}$$

and the nonlinear eigenvalue problem given in equations (5.14) and (5.15) is solved numerically to determine ϖ. Hutchinson [12] numerical analysis also indicated that p could

be described quite accurately by a simple formula of the form:

$$p = (2n + 1) / (n + 1) \tag{5.16}$$

This completes the review of the Hutchinson [12] and Rice and Rosengren [13] solution which popularly has entered the literature as the HRR stress-strain field near the crack-tip. Similar formulation will be used in the sequel to determine an asymptotic expression for the displacement in the damage-zone.

5.3 Damaged Material Governing Equations

In this section, the concept of continuum damage mechanics coupled with the basic equations of the previous section are used to obtain an asymptotic expression of the displacement components near the crack-tip using small-scale yielding solution. Introducing Kachanov damage parameter, one can write:

$$\sigma = s\,(1\text{-}D) = \Omega s \tag{5.17}$$

where s is the net stress, Ω is the continuity function, and D is the damage parameter as defined in Chapter 2. In the damaged material near the crack-tip, using Lemaitre's strain equivalent principle, the power-law equation (5.3), the stress-strain relation (5.7) and the stress function equations (5.13) can be written, respectively, as:

$$\varepsilon/\varepsilon_0 = (s/s_0)^n \tag{5.18a}$$

$$\varepsilon_{ij} = [\,3\varepsilon_0 s_{ij}/(\,2\Omega s_0\,)][s_e/\Omega s_0\,]^{n-1} \tag{5.18b}$$

$$\omega = \varkappa\, \Omega s_0 r^p \varpi(\theta) \tag{5.19}$$

where s_0 is the effective (net) yield stress, s_{ij} is the effective deviatoric stress and s_e is the effective von Mises equivalent stress.

The amplitude, $\varkappa$, however, cannot be obtained without connecting the near-tip analysis with the remote boundary conditions. The J-integral provides a simple means for making this connection in the case of small-scale yielding. For a traction free crack in plane strain (or plane stress) with the crack lying along the x-axis, the J-integral is defined as:

$$J = \int_\Gamma [W_e\, dy - \mathbf{T}.(\partial \mathbf{u}/\partial x)\, d\ell] \tag{5.20}$$

where $\mathbf{T}$ is the traction vector on the counterclockwise contour Γ (Figure 5.1), defined

according to the outward normal, $\mathbf{T}_i = \sigma_{ij} n_j$, $\mathbf{u}$ is the displacement vector, ℓ is arc length, and W_e denotes the energy density of an elastic material.

Consider two circular contours of radii r_1 and r_2 around the tip of a crack in small-scale yielding, as illustrated in Figure 5.2. Assume that r_1 is in the region described by the elastic singularity, while r_2 is well inside the plastic zone. Due to the path-independence of J, the near-tip problem for small-scale yielding can be solved by evaluating J at r_2 and relating J to the amplitude, $\varkappa$. Evaluating the J-integral at r_1 leads to:

$$J = \int_{r1} [W_e \, dy - \mathbf{T} . (\partial \mathbf{u}/\partial x) \, d\ell] = K_I^2 (1-\nu^2) / E \tag{5.21}$$

where K_I is the stress-intensity factor for Mode I.

Evaluating the J-integral at the circular contour of radius r_2 leads to:

$$W_e = \Omega s_0 e_0 \varkappa^{n+1} [n/(n+1)] \, r_2^{(n+1)(p-2)} \tilde{\alpha}^{n+1} \tag{5.22}$$

where $\tilde{\alpha}$ is defined in equation (5.15).

The radial and tangential displacements, u_r and u_θ, are readily found using the strain-displacement relations, namely,:

$$\varepsilon_{rr} = \partial u_r / \partial r \tag{5.23a}$$

$$\partial u_\theta / \partial \theta = r \varepsilon_{\theta\theta} - u_r \tag{5.23b}$$

Using equations (5.6), (5.7), (5.8), (5.19) and (5.23), one can write:

$$\mathbf{T} (\partial \mathbf{u}/\partial x) = \Omega s_0 e_0 \varkappa^{n+1} r^{(n+1)(p-2)} \{\sin\theta ([p\varpi(\theta) + \varpi''(\theta)][\tilde{v}_\theta - \tilde{v}'_r] - (1-p)\varpi'(\theta)(\tilde{v}_r + \tilde{v}'_\theta)) + \cos\theta [n(p-2)+1][(p\varpi(\theta) + \varpi''(\theta))\tilde{v}_r + (p(p-1)\varpi(\theta))\tilde{v}_\theta]\} \tag{5.24}$$

where $\tilde{v}_r$ and $\tilde{v}_\theta$ are dimensionless displacement functions, related to the polar components of the displacement, u_r and u_θ, by:

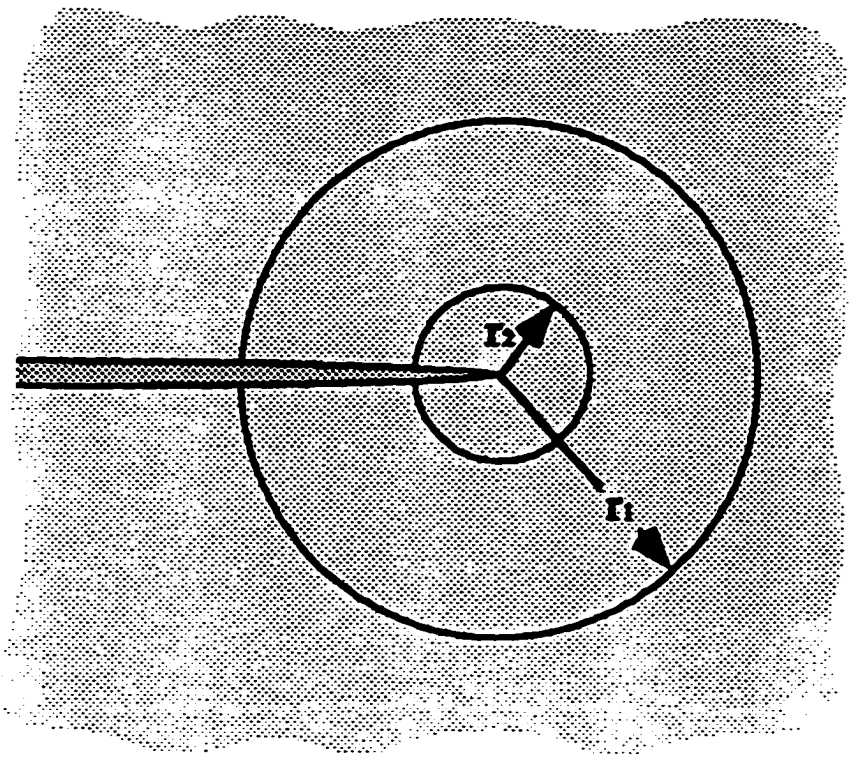

Figure 5.2 Two circular contours around the crack-tip. r_1 is in the zone dominated by the elastic singularity, while r_2 is in the plastic zone where the leading term of the HRR asymptotic expansion dominates.

$$u_r = \varepsilon_0 \varkappa^n r^{n(p-2)+1}\ \hat{v}_r(\theta) \tag{5.25a}$$

$$u_\theta = \varepsilon_0 \varkappa^n r^{n(p-2)+1}\ \hat{v}_\theta(\theta) \tag{5.25b}$$

The quantities $\hat{v}_r$ and $\hat{v}_\theta$ can be derived from the strain displacement relations for ε_{rr} and $\varepsilon_{r\theta}$ as:

$$\hat{v}_r = [(3/4)\,\acute{\alpha}^{n-1} / (2-p)][\varpi'' + p(2-p)\,\varpi] \tag{5.26}$$

$$\partial \hat{v}_\theta / \partial\theta = [p-3]\hat{v}_r \tag{5.27}$$

Evaluating the J-integral at r_2 gives:

$$J = \varepsilon_0 \Omega s_0 \varkappa^{n+1}\ r_2^{(n+1)(p-2)+1}\ I_n \tag{5.28}$$

where I_n is an integration constant given by:

$$I_n = \int_{-\pi}^{\pi} \{[n/(n+1)]\,\acute{\alpha}^{n+1} \cos\theta - [\sin\theta\,([p\varpi(\theta) + \varpi''(\theta)][\hat{v}_\theta - \hat{v}'_r] - (1-p)\varpi'(\theta)\,(\hat{v}_r + \hat{v}'_\theta))$$

$$+ \cos\theta\,[n(p-2)+1][(p\varpi(\theta) + \varpi''(\theta))\hat{v}_r + (p(p-1)\,\varpi(\theta))\hat{v}_\theta]]\}\,d\theta \tag{5.29}$$

The J-integral in equation (5.28) must equal the value obtained from the r_1 integration according to equation (5.21), in order for J to be path independent, thus:

$$\varepsilon_0 \Omega s_0 \varkappa^{n+1}\ r_2^{(n+1)(p-2)+1}\ I_n = K_I^2 (1-\nu^2) / E \tag{5.30}$$

and this condition can only be met (as $r_2 \to 0$) if:

$$p = (2n+1)/(n+1) \tag{5.31}$$

which is identical to equation (5.16), obtained numerically, also by Hutchinson [12].

Thus the amplitude of the stress function is given by:

$$\varkappa = [K_I^2 (1-\nu^2) / (E\varepsilon_0 \Omega s_0\ I_n)]^{1/(n+1)} \tag{5.32}$$

Substituting equation (5.32) into equations (5.25a) and (5.25b), the leading terms of the displacement components, for a damaged material, are obtained, in terms of J-integral as:

$$u_r = \varepsilon_0 [J / (\varepsilon_0 \Omega s_0\ I_n)]^{n/(n+1)}\ r^{1/(n+1)}\ \hat{v}_r(\theta) \tag{5.33a}$$

$$u_\theta = \varepsilon_0 [\, J / (\varepsilon_0 \Omega s_0 \, I_n)]^{n/(n+1)} \; r^{1/(n+1)} \; \tilde{v}_\theta(\theta) \qquad (5.33b)$$

The numerical values of $\tilde{u}_r(\theta)$, $\tilde{v}_\theta(\theta)$ and I_n for different strain hardening exponents are given by Shih [46].

In the sequel, equations (5.33) will be used to describe the damage law assumed in this dissertation and the criterion for the onset of crack instability for the small-scale yielding and the fully-plastic solutions. Also, based on the small-scale yielding solution, the criteria for fatigue crack growth and steady-state creep crack growth are investigated.

5.4 Determination of Damage-Zone

Precise estimates of the size of the plastic zone ahead of the tip of a crack subjected to mode I are difficult to make. In this section, a review of the efforts of estimating the plastic zone size in the literature is presented, and plastic zone shape and size are then postulated and used as the damage-zone.

It is clear from equation (5.33a) and (5.33b) that the intensity of the crack-tip fields in the J-dominant region depends only on the parameter J. Interpreting J not as an energy release rate but as a measure of the intensity of the HRR fields forms the basis of plastic fracture mechanics. Let R in Figure 5.3 denote the radius of the zone of dominance of the HRR field, and R_l denote the characteristic size of the fracture process zone where nonproportional loading, large strains, and other phenomena associated with fracture occur, but are not properly accounted for in a small strain deformation theory of plasticity. If R_l is small compared to R, it can be argued that any event that occur within the process zone must be controlled by the deformation in the surrounding "J-dominant" region. Therefore, where J-dominance exists, the initiation and growth of a crack can be expected to be governed by a critical value of J. In the discussion that follows the crack opening displacement plays an important role. Attention is focused, first, on a virgin material, and the conclusion is then extended to the damaged material. Except for the limiting case of perfect plasticity ($n = \infty$), the displacements tend to zero with r at $\theta = 0$. Due to this property, the definition of an effective crack-tip opening displacement is somewhat arbitrary. Tracey [47] used the definition, as illustrated in Figure 5.4, that the crack-tip opening displacement, δ_t is the crack opening at the intercept of the two symmetric 45° lines from the deformed crack-tip and the

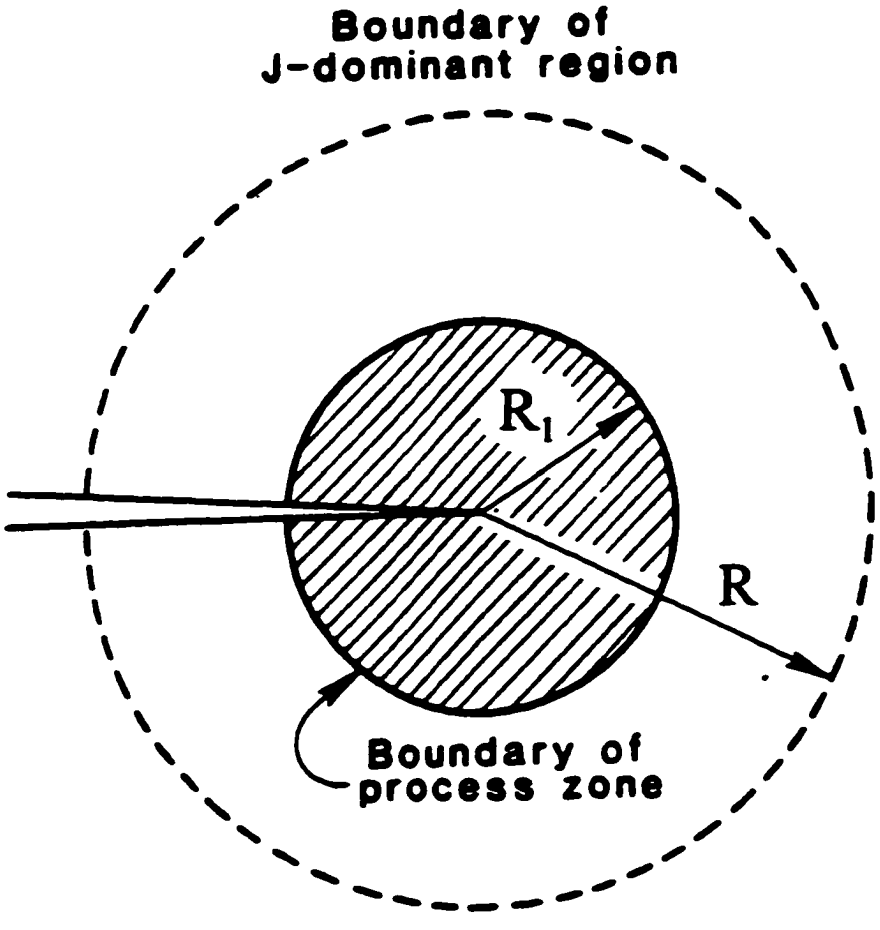

Figure 5.3 Schematic of near-tip behavior under J-dominance conditions.

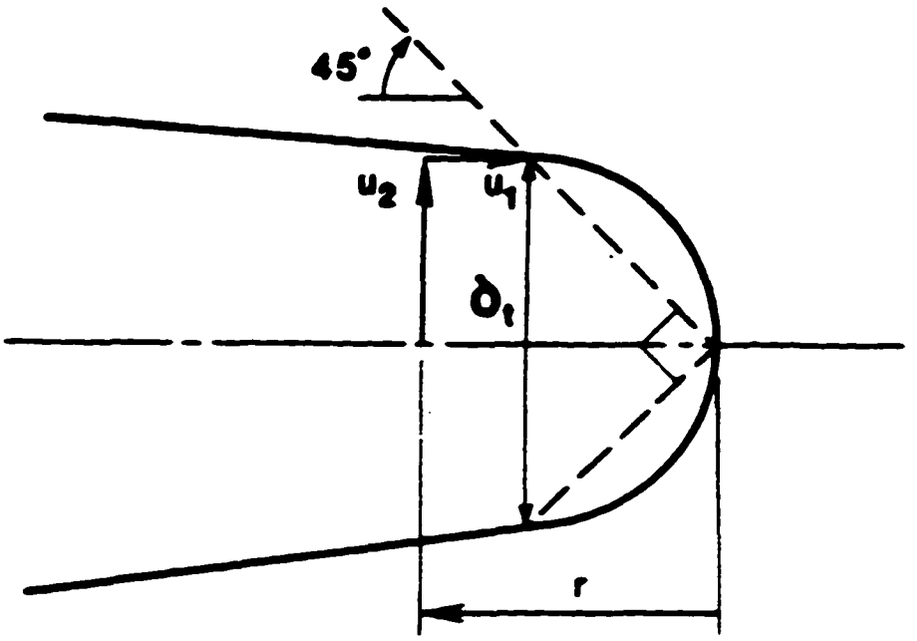

Figure 5.4 Definition of crack-tip opening displacement [47].

crack profile. Shih computed this value and the result is [20]:

$$\delta_t = d_n J / \sigma_0 \tag{5.34}$$

with values of d_n ranging from about 0.8 for large n to about 0.3 for n=3. The crack-tip opening displacement provides a measure of the size of the zone in which finite strains are important. Finite element studies based on finite strain incremental plasticity formulations have been performed for the plane strain small-scale yielding problem [48,49]. For distances from the crack-tip that are greater than 2 or 3 times δ_t, the deviations from small-strain theory become unimportant.

Hutchinson [50] postulated that two conditions are required for J-dominance. First:

$$R > 3\,\delta_t \tag{5.35}$$

Second, the radius R should be greater than the fracture process zone in which the microscopic separation processes occur. The fracture process zone extent is typically on the order of δ_t for ductile rupture [51]. The predominant ductile fracture mechanism is void nucleation, growth, and coalescence. Since hole growth is itself a finite strain process, the fracture process zone for this mechanism is roughly comparable to the zone of finite strains, and therefore equation (5.35) again serves to ensure J-dominance.

The characteristic size R of the zone of dominance of the HRR singularity field depends strongly on hardening as shown by Rice and Rosengren [13]. From the expressions of the Mises equivalent shear stress, τ, and shear strain, γ, they determined the approximate distance from the crack-tip to the elastic-plastic boundary $R(\theta)$ as:

$$\tau = \tau_0 [R(\theta) / r]^{1/(n+1)} \quad , \quad \gamma = \gamma_0 [R(\theta) / r]^{1/(n+1)} \tag{5.36}$$

where $R(\theta) = R(\theta;J,n)$. From equation (5.36), one immediately sees that $R(\theta)$ gives the shape

of constant equivalent strain lines very near the crack-tip and that $R(\theta)$ can be interpreted as an approximate indication of the distance from the crack-tip to the elastic-plastic boundary (approximate since HRR solution gives the singular term only, and not of necessity the complete solution in the plastic region).

Figure 5.5 shows the nondimensional distance $[\ \gamma_0\tau_0 R(\theta) / J\ ]$ for different values of n. One noteworthy feature of this figure is the strong dependence of $R(\theta)$ on the strain hardening. It also indicate that the plastic zone engulfing the crack-tip in plane strain mode I cracking is elongated in shape and not a circular zone like that of the anti-plane case (mode III), even for small-scale yielding. Additional details are available in Rice [52].

Numerical solutions in small-scale yielding indicate that the HRR singularity fields provide a fairly good approximation out to a distance ahead of the tip of roughly [50]:

$$R = (0.2 \text{ to } 0.25)\ r_p \tag{5.37}$$

where r_p is the distance to the elastic-plastic boundary for linear-elastic fracture mechanics. Expressing r_p in terms of the J-integral, for plane strain, yields:

$$r_p = (1/3\pi)\ [\ J / (\sigma_0)^2\ ]\ [\ E / (1 - \nu^2)\ ] \tag{5.38}$$

It is recognized that the extension of the plastic zone ahead of the tip of a crack, subject to mode I in plane strain, is of elongated oval shape. However, for convenience of calculations, the damage-zone in this dissertation is postulated as a circle of radius $(0.25\ r_p)$, centered at the crack-tip. This assumption is substantiated by equation (5.37) introduced by Hutchinson. Therefore, for a virgin material, the plastic zone size, C, is given as:

$$C = (1/12\pi)\ [\ J / (\sigma_0)^2\ ]\ [\ E / (1 - \nu^2)\ ] \tag{5.39a}$$

In the damaged material, it follows that the distance C becomes:

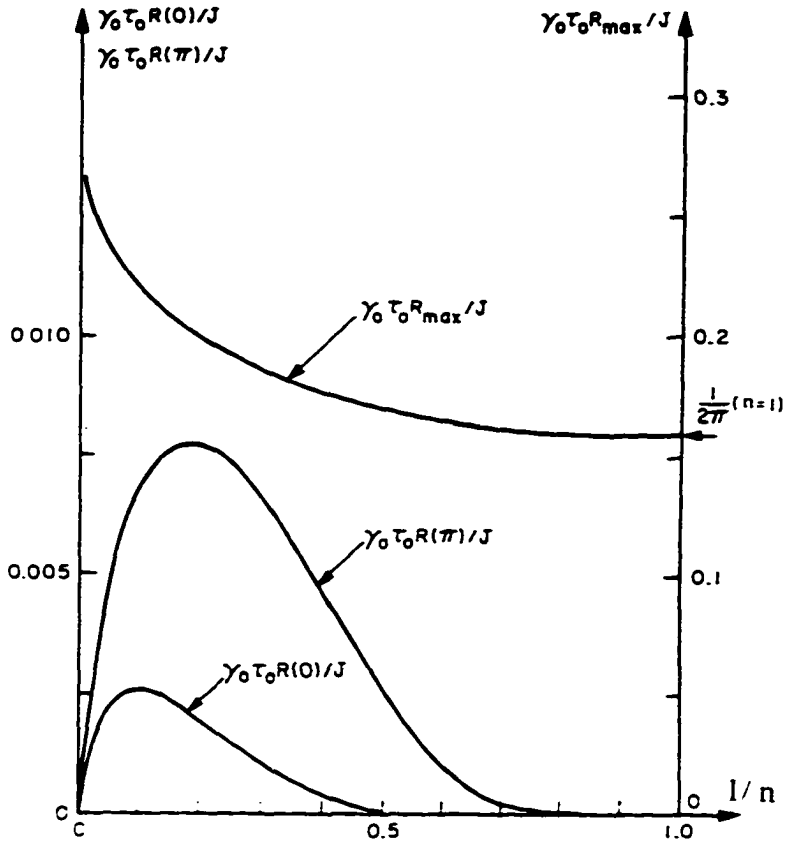

Figure 5.5 Approximate extensions of elastic-plastic boundary ahead, R(0), and behind, R(π), the crack-tip and also maximum size of approximate plastic zone, R_{max}, for plane strain of a power hardening material [13].

$$C = (1/12\pi s_0)(J/s_0)[E/(1-\nu^2)]\Omega^{-2} \qquad (5.39b)$$

where s_0 is the net yield stress of the material. It should be noted that the size of the damage-zone given in equation (5.39b) is not dependent on the strain hardening exponent for the small-scale yielding solution. The effect of this independence will be addressed in the discussion of numerical results of crack instability criterion in Chapter 6.

5.5 Criterion for Crack Instability

In this section, the concepts of continuum damage mechanics are applied to the stress and displacement fields derived earlier to determine the conditions required for the onset of crack instability. The damage is confined to the damage-zone postulated in the previous section, whose radius is given by equation (5.39b). Any uniform damage induced outside the zone is neglected. Inside the zone, the continuity function, Ω, is assumed to take constant values. Inside the damage-zone, the tensile stress is given in terms of the net (effective) yield stress:

$$\sigma_i = s_0 [\, 1 - \lambda u_i \,] \tag{5.40}$$

where u_i is the HRR displacement given by equations (5.33a) and (5.33b), for i = r and i = θ, respectively, and λ is the damage parameter defined in section 2.3. In particular, equating the value of the exact tensile stress given by equation (5.40) to the approximate stress, Ωs_0, at (r, $\pi/4$), with r set equal to C in equation (5.39b), yields:

$$(1 - \Omega) = (\lambda s_0 / E) .[J / s_0]\, \Omega^{-[(n+2)/(n+1)]}\, \xi(n) \tag{5.41}$$

where,

$$\xi(n) = \varepsilon_0^{-1} .[\, I_n \,]^{-n/(n+1)}\, [12\, \pi\, (1 - \nu^2)]^{-1/(n+1)}\, [\hat{v}_r(\pi/4) + \hat{v}_\theta(\pi/4)] \cos(\pi/4) \tag{5.42}$$

The measure of damage, D, is computed from the crack-tip opening displacement, 2 u_r(r, $\pi/2$), with setting r = C, which yields:

$$D = (\lambda s_0 / E) .[J / s_0]\, \Omega^{-[(n+2)/(n+1)]}\, \zeta(n) \tag{5.43}$$

where,

$$\zeta(n) = 2.\, \varepsilon_0^{-1} .\, [\, I_n \,]^{-n/(n+1)}\, [12\, \pi\, (1 - \nu^2)]^{-1/(n+1)}\, [\hat{v}_r(\pi/2)] \tag{5.44}$$

The criterion for the onset of crack instability is established by requiring D(r,$\pi/2$) in equation (5.43) to approach unity and using equation (5.41) to eliminate the continuity function, Ω.

The result is:

$$(\lambda s_0 / E) .[J / s_0] = \{1 - [\xi(n)/\zeta(n)]\}^{(n+2)/(n+1)} / \zeta(n) \qquad (5.45)$$

A noteworthy feature demonstrated by equation (5.45), combined with equations (5.42) and (5.44), is the effect of Poisson's ratio, ν, on the onset of crack instability criterion. This dependence will be further discussed in Chapter 6.

In the remaining part of this section, equation (5.45) is used to predict the onset of crack instability for external loading characterized by the small-scale yielding and the fully plastic solution.

5.5.1 Small-Scale Yielding Solution

For small-scale yielding, the J-integral is replaced by the elastic stress-intensity factor, namely, $J = (1 - \nu^2) K_I^2 / E = \pi (1 - \nu^2) \sigma_\infty^2 a_0 / E$. Substituting in equation (5.45), the following condition for the onset of crack instability is obtained:

$$(\lambda s_0 a_0 / E) .[\pi (1 - \nu^2) \varepsilon_0] (\sigma_\infty / s_0)^2 = \{1 - [\xi(n)/\zeta(n)]\}^{(n+2)/(n+1)} / \zeta(n) \qquad (5.46)$$

In order for small-scale yielding to be valid, (σ_∞ / s_0) has to be less than about 0.5. It is clear that equation (5.46) confirms Griffith's classical result, namely, σ_∞ is proportional to $a_0^{-.5}$. The constant of proportionality in equation (5.46) is a material parameter. It is worthy to note that the same result was obtained in section 2.4.1 for the small-scale yielding solution for the anti-plane case (mode III), where equation (2.42) which describes the criterion for crack instability in mode III, resembles equation (5.46) for mode I.

5.5.2 Large-Scale Yielding Solution

The analysis that leads to the HRR singularity does not consider the effect of the blunted crack-tip on the stress fields, nor does it take account of the large strains that are present near the crack-tip. As mentioned earlier, this analysis is based on small-strain theory, which is the multi-axial equivalent of engineering strain in a tensile test.

McMeeking and Parks [53] performed crack-tip finite element analyses that incorporated large strain theory and finite geometry changes. Some of their results are shown in Figure 5.6, which is a plot of stress normal to the crack plane versus distance. The HRR singularity is also shown on this plot. Note that both axes are nondimensionalized in such a way that both curves are invariant, as long as the plastic zone is small compared to specimen dimensions. The solid curve in Figure 5.6 reaches a peak when the ratio $x\sigma_0 / J$ is approximately unity, and decreases as $x \rightarrow 0$. This distance corresponds approximately to twice the crack-tip opening displacement, δ_t. The HRR singularity is invalid within this region, where the stresses are influenced by large strains and crack blunting. However, Shih finite element analysis [20] uses the HRR solution to evaluate displacements well within the large strain region. Crack-tip finite element analyses [20] are in general agreement with equation (5.34). Thus the displacement fields predicted from the HRR theory are reasonably accurate, despite the large plastic strains at the crack-tip.

The extension to large-scale yielding involves using the fully plastic solution for Rice's J-integral in equations (5.41) and (5.43). For convenience, the damage-zone extension in large-scale yielding is assumed to be the same as that postulated in the previous section for

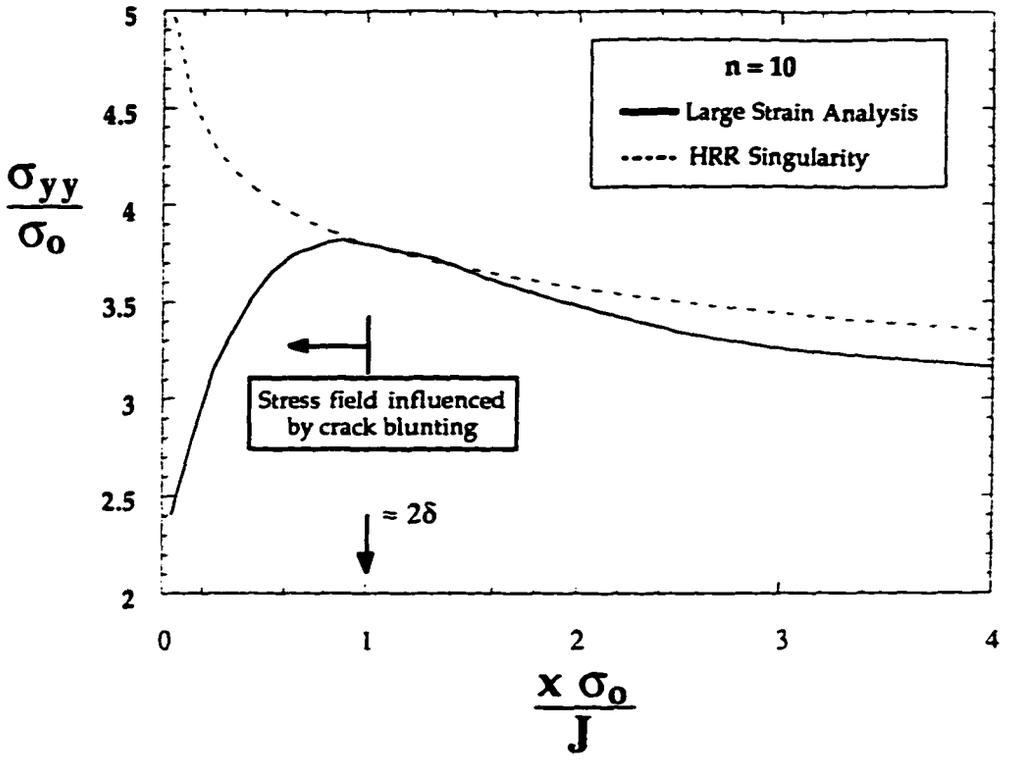

Figure 5.6 Large-strain crack-tip finite element results of McMeeking and Parks [53].

small-scale yielding. The fully plastic J for the damaged material can be obtained along the same lines developed by Kumar et al. [19]. For a crack of length $2a_0$, in an infinite strip of width, 2W, subjected to a constant stress, σ_∞, at the remote boundary, under fully-plastic conditions, when the plastic zone has reached across the entire uncracked ligament, b, it can be shown that:

$$J / s_0 = (s_0 a_0 / E) (\sigma_\infty / s_0)^{n+1} (b/w) h_1 (n) \Omega^{-n} \quad (5.47)$$

where h_1 (n) is a function of the strain hardening exponent and geometry [19], whose numerical values are given in Table 5.1, for $(a_0/W) = 0.125$.

Table 5.1

Numerical values of the function h_1 (n) in equation (5.47)

n	h_1 (n)
1	2.8
2	3.61
3	4.06
5	4.35
7	4.33
10	4.02
13	3.56
16	3.06
20	2.46

Substituting equation (5.47) into equation (5.43) and setting the damage parameter, D, to unity, the following relation is reached:

$$\Omega = \{(\lambda s_0 a_0 / E) (\sigma_\infty / s_0)^{(n+1)} \varepsilon_0 (b/w) h_1 (n) \zeta(n)\}^m \quad (5.48)$$

where the superscript, m, is given by: $m = (n+1) / (n^2 + 2n + 2)$.

Setting the exact and approximate stress equal at $\theta = \pi/4$, one can write:

$$\Omega = 1 - (\lambda s_0 a_0/E) (\sigma_-/s_0)^{(n+1)} . \varepsilon_0 (b/w) h_1 (n).\xi(n) \ \Omega^{-m} \qquad (5.49)$$

Eliminating Ω from equations (5.48) and (5.49) results in:

$$(\lambda s_0 a_0/E) (\sigma_-/s_0)^{(n+1)} [\varepsilon_0 (b/w) h_1 (n)] = \{1 - [\xi(n)/\zeta(n)]\}^m / \zeta(n) \qquad (5.50)$$

Equation (5.50) shows that σ_- is proportional to $a_0^{-1/(n+1)}$, which is similar to the result obtained in section 2.4.2 for the anti-plane mode. It is interesting to note that for n=1, this result reduces to Griffith crack, namely, σ_- is proportional to $a_0^{-0.5}$, which was also observed for mode III. Equation (5.50) is valid for values of σ_-/s_0 in the range 0.5 to 1.0.

Numerical evaluations of conditions (5.46) and (5.50) are carried out and discussed in Chapter 6.

5.6 Fatigue Crack Propagation

Based on the small-scale yielding solution, fatigue crack propagation under cyclic tensile loading varying from 0 to σ_∞, is investigated in this section. An instantaneous damage increment is accumulated in the circular damage-zone in each cycle. No damage is caused upon unloading from σ_∞ to 0. Within the postulated damage-zone, the damage increment, ΔD, per each cycle of loading is proportional to the crack opening displacement (displacement components normal to the crack plane). In the following calculations, r is set equal to C given in equation (5.39b).

Denoting by $D(r, \pi/2)$, the damage at a point $(r, \pi/2)$ from the crack-tip, it follows that after N load cycles:

$$D(r, \pi/2; N) = D(r, \pi/2: N-1) + \eta . u_r(r, \pi/2; N) \tag{5.51}$$

where η is the same damage parameter, defined in section 2.5, and $D(r, \pi/2 ; N)$ is a function of the continuity function, Ω.

To obtain a value of the continuity function, Ω, the exact and the approximate principal stresses are set equal at $(r, \pi/4)$, i.e.

$$\Omega(N) = 1 - D(r, \pi/4 ; N) \tag{5.52}$$

where now $D(r, \pi/4 ; N)$ is given by:

$$D(r, \pi/4 ; N) = D(r, \pi/4 ;N-1) + \eta .[u_r(r, \pi/4 ;N) + u_\theta(r, \pi/4 ;N)] (1/\sqrt{2}) \tag{5.53}$$

Combining equations (5.33), (5.52), and (5.53), one can write:

$$\Omega(N) = 1 - (\eta s_0 a_0 / E) .[\pi (1 - \nu^2) \varepsilon_0]^{n/(n+1)} (\sigma_\infty/s_0)^2 \xi(n) .\{[\Omega^{-[(n+2)/(n+1)]} (N-1)] + [\Omega^{-[(n+2)/(n+1)]} (N)]\} \tag{5.54}$$

For N = 0, there is no damage and Ω=1, while corresponding to N = 1, there is instantaneous

damage accumulated in the damage-zone, whereby, the extent of this zone and the crack opening displacement within the zone can be evaluated. The extent of damage-zone ahead of the crack-tip is obtained from equation (5.39b) as:

$$C(N) = (1/12\pi)\,(K_I/\Omega(N)\,s_0)^2 \tag{5.55}$$

For each cycle of loading, $u_r(r, \pi/2)$, $u_r(r, \pi/4)$, $u_\theta(r, \pi/4)$, $\Omega(N)$ and $C(N)$, are calculated using equations (5.33) and (5.52)-(5.55). As previously mentioned, Figure 2.4 depicts a schematic description of the crack growth criterion, where $D(r, \theta; N)$ is shown versus r, the polar distance ahead of the crack-tip. For N=1 and N=2, where $D(r, \pi/2;N)$ is less than unity, $a(N) = a_0$, the initial crack length. Next, the number of cycles is increased by one and $\Omega(N)$ of the previous step is used to update $u_r(r, \pi/2)$, $u_r(r, \pi/4)$ and $u_\theta(r, \pi/4)$. By using equations (5.51)-(5.55), an iterative procedure is repeated until $D(r, \pi/2;N)$ assumes a value slightly above one (1+), then the crack has grown during the actual cycle.

The new crack length, a, which is found from the condition:

$$D(a_N, N) = 1. \tag{5.56}$$

is incrementally computed from:

$$a_N = a_0 + da_N \tag{5.57}$$

where:

$$da_N = [1 - \{1/D(r, \pi/2;N)\}]\; C(N) \tag{5.58}$$

Using the new crack length given by equations (5.57) and (5.58), the iterative process can be repeated to obtain the final values of a(N), C(N), $w(r, \theta;N)$, $D(r, \theta;N)$ and $\Omega(N)$ at which instability is reached, i.e., the critical crack length to cause crack propagation is reached.

Numerical calculations have been carried out and the influence of strain hardening and material parameters on the variations of load cycles with the critical crack lengths are presented in Chapter 6.

5.7 Time-Dependent Crack Propagation

5.7.1 Introduction

Time-dependent fracture in terms of a damage variable due to steady-state creep crack growth, under mode I conditions, is considered in this section. Creep is assumed to be artificially confined to a narrow region ahead of the crack-tip following the idea of Dugdale crack model [24]. Hence, the structural component is assumed to be predominantly elastic, and the steady-state creep zone and the resulting damage field is confined to a small region near the crack-tip. In this case, the crack growth can be characterized by the stress-intensity factor [41]. By limiting the analysis to small-scale yielding and to power law creep of the Ramberg-Osgood form, steady-state or secondary creep is prevalent.

Section 5.7.2 contains a brief summary of the basic mathematical equations required for the analysis of steady-state creep under mode I conditions. Section 5.7.3 deals with creep crack growth under constant load. For given material parameters, the elapsed time required for the onset of crack growth and the elapsed time required for failure are determined.

5.7.2 Time-Dependent Basic Equations

The constitutive equations used in the time-dependent case express the rate of growth of deformation and damage for steady-state, or secondary, creep. The time-dependent deformation is characterized by the strain rate. As noted by Goldman and Hutchinson [44] and adopting Hoff's analogy [45], for a creep law of the form:

$$\dot{\varepsilon} / \varepsilon_0 = (\sigma / \sigma_0)^n \tag{5.59}$$

the constitutive equations have the same form as the equations governing the rate-insensitive, power law strain hardening material. Here, n is the creep exponent of the material and a dot on top of a letter indicates differentiation with respect to time. Thus, the formulas developed in sections 5.3 and 5.4, describing the displacement field and plastic zone extension ahead of the crack-tip, all continue to hold if the strain, ε, is replaced by the strain rate, $\dot{\varepsilon}$, and the displacement, u_i, is replaced by displacement rate, $\dot{u}_i$.

Introducing Lemaitre's strain equivalence principal to equation (5.59), one can write:

$$\dot{\varepsilon} / \varepsilon_0 = (s / s_0)^n \tag{5.60}$$

For time-dependent deformation, the reference stress, σ_0, is related to the reference strain rate, $\dot{\varepsilon}_0$, for a virgin material, by the relation:

$$\sigma_0 = F . \dot{\varepsilon}_0 \tag{5.61}$$

where F is a time-dependent material parameter.

The deformation is composed of one instantaneous part and one time-dependent part. No damage is assumed to be induced immediately on loading. Thus, introducing the rate of damage of the material, $\dot{D}$, consisting of a uniform component, $\dot{D}_0$, and a component proportional to the crack opening displacement, one can write:

$$\dot{D}(r,\theta;t) = \dot{D}_0 + \beta.[u_r(r,\theta;t)\sin\theta + u_\theta(r,\theta;t)\cos\theta] \quad (5.62)$$

where β is the same damage parameter, defined in Chapter 4, and t denotes the time. This equation can be integrated in time to give:

$$D(r,\theta;t) = \int_0^t \dot{D}_0\, dt' + \beta \int_0^t [u_r(r,\theta;t')\sin\theta + u_\theta(r,\theta;t')\cos\theta]\, dt' \quad (5.63)$$

As assumed in the rate-insensitive case, most damage is concentrated to a narrow band of large deformation ahead of the crack-tip, which is called creep-zone. Then, as with equation (5.17), the stress in the creep-damage-zone can be expressed as:

$$\sigma(r,\theta;t) = s_0 \{ 1 - \int_0^t \dot{D}_0\, dt' - \beta \int_0^t [u_r(r,\theta;t')\sin\theta + u_\theta(r,\theta;t')\cos\theta]\, dt' \} \quad (5.64)$$

In the time-dependent case, both the crack and the damage-zone boundary will grow into the component with time. $\dot{D}_0$ has been assumed to depend on the net stress far from the crack, s_∞. It follows that using equation (5.17):

$$s_\infty = \sigma_\infty / (1 - D_0) \quad (5.65)$$

where $D_0 = \int_0^t \dot{D}_0\, dt'$.

A power law, commonly used in brittle creep rupture [3], may be used to relate $\dot{D}_0$ to s_∞, such that:

$$\dot{D}_0 = \kappa (s_\infty / s_0)^{\vartheta} \quad (5.66)$$

where κ and ϑ are material constant independent of stress and time. Combining equations (5.65) and (5.66) yields:

$$\dot{D}_0 = \kappa [\sigma_\infty / (s_0(1 - D_0))]^{\vartheta} \quad (5.67)$$

Assuming the applied load, σ_∞, is constant in time, equation (5.67) can be integrated in time, using zero initial conditions, to yield:

$$D_0 = 1 - [1 - (\vartheta + 1)\kappa(\sigma_\infty / s_0)^{\vartheta} t]^{1/(\vartheta+1)} \quad (5.68)$$

Additional damage due to deformation of the material in the creep-damage-zone is added to equation (5.68). It is assumed that, at a certain time, every point in the component except for the damage-zone around the crack-tip has a damage D_0 given by equation (5.68). Because of this uniform damage outside the zone, the stress and net stress distributions will be the same as in the rate-insensitive case, developed in sections 5.3 and 5.4, an important fact for the following analysis. The damage and stress within the zone can now be written, using equations (5.63), (5.64) and (5.68), as:

$$D(r,\theta;t) = 1 - [1 - (\hat{\upsilon} + 1)\,\kappa\,(\sigma_- / s_0)^{\phi}\, t\,]^{1/(\hat{\upsilon}+1)} + \beta \int_0^t u_i(r,\theta;t')\, dt' \tag{5.69}$$

$$\sigma(r,\theta;t) = s_0 \{ [1 - (\hat{\upsilon} + 1)\,\kappa\,(\sigma_- / s_0)^{\phi}\, t\,]^{1/(\hat{\upsilon}+1)} - \beta \int_0^t u_i(r,\theta;t')\, dt' \} \tag{5.70}$$

Assuming $\sigma(r,\theta;t) = \Omega(t)\, s_0 =$ constant, the extension of the creep-damage-zone ahead of the crack-tip is obtained from:

$$C(t) = (1/12\pi)\,(K_I / \Omega(t) s_0)^2 \tag{5.71}$$

At a certain time:

$$u_i(r,\theta;t) = u_i(r,\theta;0) + \int_0^t \dot{u}_i(r,\theta;t')\, dt' \tag{5.72}$$

where according to equations (5.33a) and (5.33b), for small-scale yielding:

$$u_r(r,\theta;t) = \varepsilon_0 [\, K_I^2\,(1-\hat{\upsilon}^2) / (E\varepsilon_0 \Omega(t) s_0\, I_n)]^{n/(n+1)}\; r^{1/(n+1)}\; \hat{v}_r(\theta) \tag{5.73a}$$

$$u_\theta(r,\theta;t) = \varepsilon_0 [\, K_I^2\,(1-\hat{\upsilon}^2) / (E\varepsilon_0 \Omega(t) s_0\, I_n)]^{n/(n+1)}\; r^{1/(n+1)}\; \hat{v}_\theta(\theta) \tag{5.73b}$$

and the rate of displacement follows as:

$$\dot{u}_r(r,\theta;t) = \varepsilon_0 [\, K_I^2\,(1-\hat{\upsilon}^2) / (F\varepsilon_0 \Omega(t) s_0\, I_n)]^{n/(n+1)}\; r^{1/(n+1)}\; \hat{v}_r(\theta) \tag{5.74a}$$

$$\dot{u}_\theta(r,\theta;t) = \varepsilon_0 [\, K_I^2\,(1-\hat{\upsilon}^2) / (F\varepsilon_0 \Omega(t) s_0\, I_n)]^{n/(n+1)}\; r^{1/(n+1)}\; \hat{v}_\theta(\theta) \tag{5.74b}$$

In the next section, equations (5.60) through (5.74) are used to describe the criterion for steady-state creep crack growth, where r is set equal to C given in equation (5.39b).

5.7.3 Steady-State Creep Crack Growth

By equating the approximate stress value $\Omega(t)s_0$ and the exact stress value from equation (5.70), at $(r, \pi/4)$, the continuity function, $\Omega(t)$, is given by:

$$\Omega(t) = [1-(\hat{\theta}+1)\kappa(\sigma_{-}/s_0)^{\hat{\theta}}t]^{1/(\hat{\theta}+1)} - \beta\int_0^t [u_i(r,\pi/4;t') + u_\theta(r,\pi/4;t')](1/\sqrt{2})\,dt' \qquad (5.75)$$

where one can solve for $\Omega(t)$ in equation (5.75) at a certain time by iteration. To solve for $D(r,\theta;t)$, one needs to perform an integration in time. This is made approximately by straight-forward calculations at finite time steps as follows: At time $t=0$, there is no damage and $\Omega(0)=1$. The displacement and displacement rate components $u_i(r,\theta;0)$ and $\dot{u}_i(r,\theta;0)$ are determined from equations (5.73) and (5.74), respectively, with $\Omega(0)=1$. At time $t=\Delta t$, assume a linear variation of $u_i(r,\theta;t)$ during a time step. Then, from equation (5.69), it is readily shown that:

$$D(r,\theta;\Delta t) = 1-[1-(\hat{\theta}+1)\kappa(\sigma_{-}/s_0)^{\hat{\theta}}t]^{1/(\hat{\theta}+1)} + \beta[u_i(r,\theta;0)\Delta t + (1/2)\,\dot{u}_i(r,\theta;0)(\Delta t^2) \qquad (5.76)$$

and the crack opening is obtained by using:

$$u_i(r,\theta;\Delta t) = u_i(r,\theta;0) + \dot{u}_i(r,\theta;0)\,\Delta t \qquad (5.77)$$

Here, $i = r$ and θ.

As shown in Figure 4.3, if the damage, $D(r,\pi/2;\Delta t)$, is less than unity then the crack has not grown during the time interval and, $a(\Delta t) = a_0$, the initial crack length. The damage at $(r,\pi/4)$ is obtained from equation (5.69) and the continuity function from equation (5.75) and the time t is increased to $(t+\Delta t)$ and Ω of this step is used to update the displacements and the displacement rates at $(r,\pi/2)$ and $(r,\pi/4)$. By using equations (5.69) and (5.73)-(5.77), an

iterative procedure is repeated until $D(r,\pi/2;t)$ slightly exceeds unity, then the crack has grown during the time interval, as indicated schematically in Figure 4.3.

The new crack length is found from the condition:

$$D(r,\pi/2;\Delta t) = 1. \tag{5.78}$$

The new crack length is given by:

$$a_t = a_0 + da_t \tag{5.79}$$

where:

$$da_t = [1-\{1/D(r,\pi/2;t)\}]\, C(t) \tag{5.80}$$

Using the new crack length, the iterative process can be repeated for $t = 2\Delta t, 3\Delta t, \ldots$, etc. until instability is reached, i.e., the critical length of the crack grows to very high values.

The creep crack growth numerical results have been carried out and the influence of creep exponent and material parameters on the variations of elapsed time with the critical crack lengths are presented in Chapter 6.

6 MODE I NUMERICAL RESULTS AND DISCUSSION

6.1 Introduction

In Chapter 5, a circular damage zone engulfing the crack-tip was postulated and used to establish the conditions for the onset of crack instability, crack growth under cyclic loading and crack growth due to steady-state creep, employing the HRR asymptotic solution. This Chapter presents numerical results and discussion of the influence of the strain hardening, creep exponent and material parameters on these criteria.

The numerical results are presented in three parts: First, the onset of crack growth instability for external loading characterized by the small-scale yielding and the fully-plastic solutions are numerically evaluated and displayed graphically. Second, numerical results of the fatigue crack growth are presented to reveal the influence of the strain hardening exponent and material parameters on the relation between the number of load cycles and crack length required for failure. Third, for given material parameters, the time required for the onset of crack growth and the time required for failure are determined and graphically exhibited to show the influence of the creep exponent and material parameters on the creep crack growth process.

6.2 Criterion for Crack Instability

Equations (5.46) and (5.50) give the criterion for the onset of crack instability for the small-scale yielding and the fully-plastic solutions, respectively. These equations are plotted in Figure 6.1 where the variation of the critical external stress, σ_∞/s_0, with the material parameter ($\lambda s_0 a_0 /E$) is shown, for $\nu = 0.3$. When the critical state is reached, the crack will start to grow unstably. The crack instability is followed immediately by crack growth to failure. In order for small-scale yielding to be valid, σ_∞/s_0 has to be less than 0.5. On the other hand, large-scale yielding prevails when σ_∞/s_0 assumes values in the range 0.5 to 1. For the small-scale yielding solution, Figure 6.1 demonstrates a straight line relationship between (σ_∞/s_0) and ($\lambda s_0 a_0 /E$), in which σ_∞ is proportional to $a^{-0.5}$, which is Griffith's classical result obtained by energy criterion [32]. For the large-scale yielding solution, Figure 6.1 also reveals that the critical stress is proportional to $a_0^{-1/(n+1)}$. This reduces to Griffith's classical result for elastic material (n = 1). It is interesting to note that the same order of proportionality between the applied stress and the original crack length is observed for the anti-plane mode, as shown in Chapter 2. This shows the similar characteristics demonstrated by the two basic modes of crack extension and growth.

It is clear from Figure 6.1 that the external load required to cause instability decreases with increasing the strain hardening exponent, n. For small-scale yielding, Figure 6.1 shows insignificant influence of the hardening exponent, n. For the large-scale yielding, the figure reveals somewhat appreciable dependence on the hardening. However, upon comparing the results shown in Figure 6.1 versus those of Figure 3.1 of the anti-plane mode (mode III), one can see that the dependence on the strain hardening exponent is more pronounced in Figure

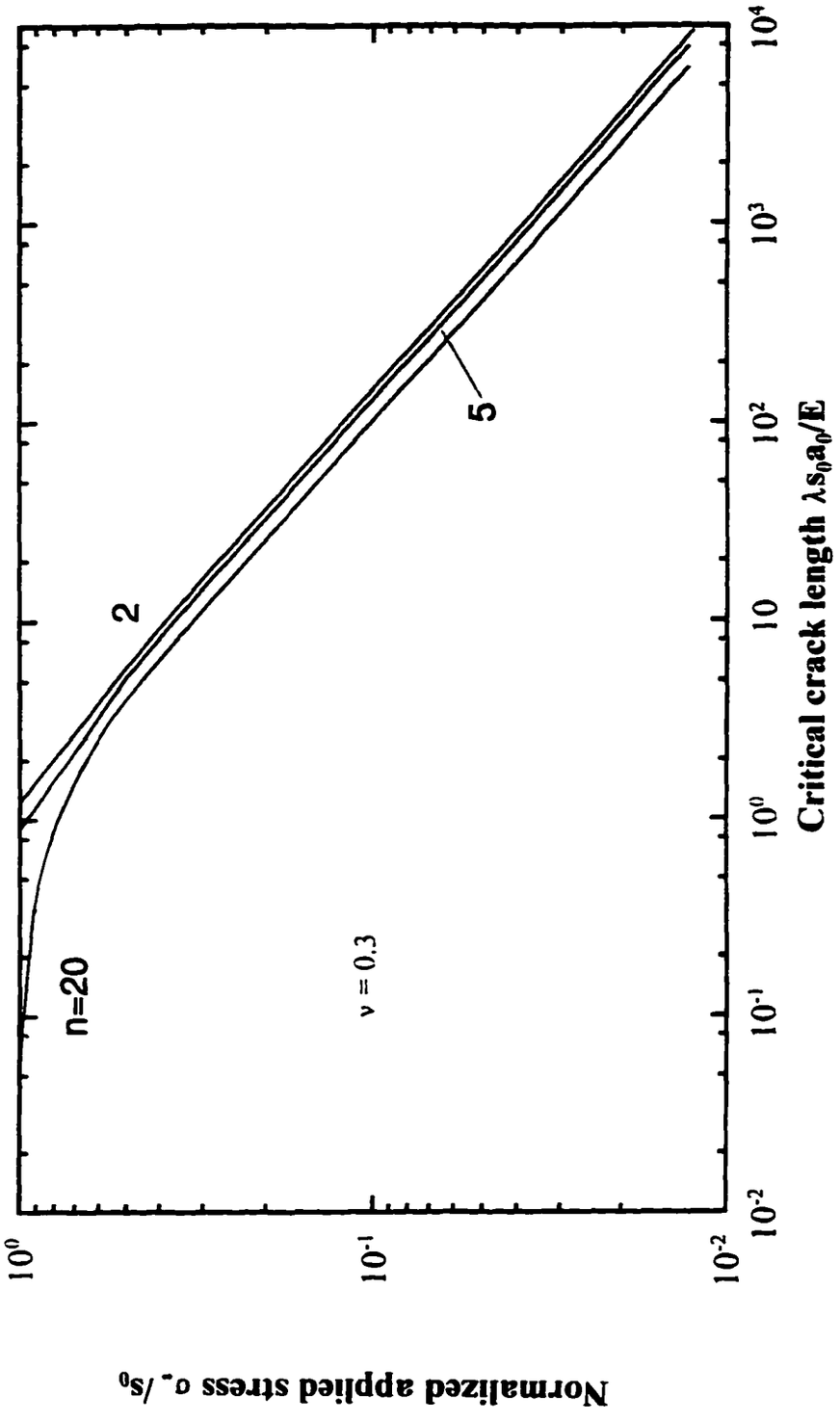

Figure 6.1 Variation of the external stress, σ_∞/s_0, with crack length, a_0.

3.1 (mode III case). This difference may be attributed to the fact that the radius and center of the plastic zone postulated for mode I, given in equation (5.39b), are basically independent on the strain hardening for the small-scale yielding, while the plastic zone size expression derived in Chapter 2 depends on the strain hardening exponent as evident by equation (2.27). It is worthy to note that, as the crack length increases, lower external load is required to cause instability. Another noteworthy feature about the developed criterion is the effect of Poisson's ratio, ν, on the crack instability. Figure 6.2 exhibits the instability curve corresponding to a strain hardening exponent, $n = 20$, for two different values of Poisson's ratio, namely, $\nu = 0.0$ and $\nu = 0.5$. The influence of Poisson's ratio, ν, on the fully-plastic solution is by no means significant. However, Figure 6.2 shows a more pronounced influence of ν on the small-scale yielding range of the curve. It is also clear from the figure that the higher value of Poisson's ratio, namely, $\nu = 0.5$ corresponds to a higher value of the crack length at instability compared with $\nu = 0.0$, for the same load ratio and (hypothetically) the same material parameter. This result is expected, as higher value of Poisson's ratio reflects higher ductility of the material and larger capacity to sustain plastic deformation imposed by the damage process.

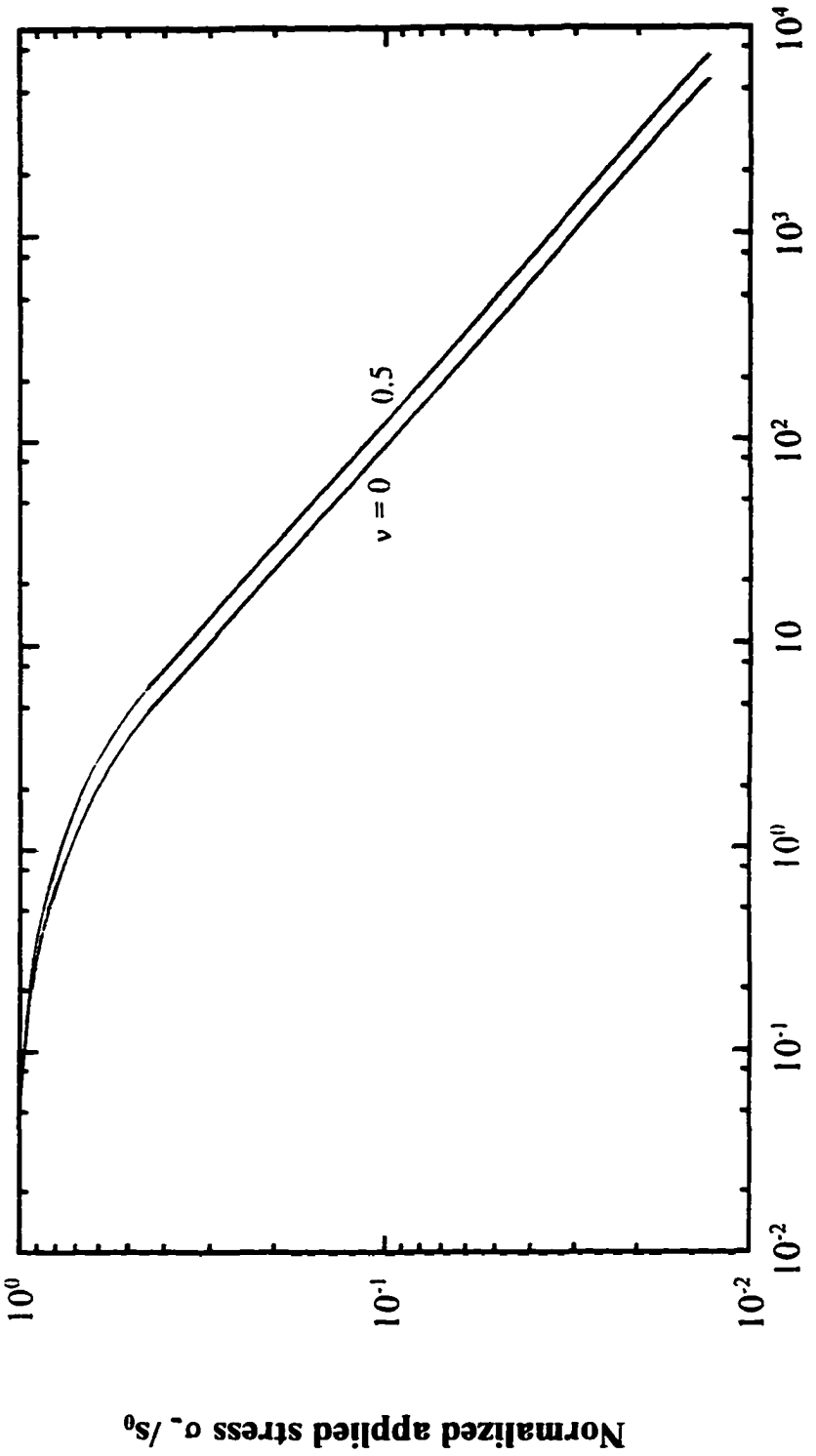

Figure 6.2 Influence of Poisson's ratio on crack instability for n=20.

6.3 Fatigue Crack Propagation

The course of fatigue crack propagation has been studied numerically for different material parameters and external stress levels, σ_∞/s_0. The numerical analysis revealed a strong influence of strain hardening, (n=2 to n=100), on the fatigue process.

Figures 6.3 and 6.4 exhibit the relationship between the normalized crack length, $a(N)/a_0$, and the number of loading cycles, N, with the stress level, σ_∞/s_0=0.4 and different values of material parameter, $\eta s_0 a_0 /E$, namely, 0.8 and 0.4, respectively. Figure 6.5 reveals similar behavior for σ_∞/s_0=0.6. Figures 6.3 through 6.5 show a period of incubation, where the damage accumulates without crack growth, followed by an accelerating crack growth period resulting in instability at certain crack length and number of loading cycles to failure, N_f. The crack growth period starts at the end of the incubation period where the damage parameter reaches unity at (r/2, π/2) and the corresponding number of cycles is N_i, signifying the onset of crack growth. A schematic diagram depicting the appearance of the incubation and the growth periods is shown in Figure 3.5. Comparing Figures 6.3 and 6.4, it is readily obtained that for the same stress level, (σ_∞/s_0=0.4), upon varying the material parameter ($\eta s_0 a_0 /E$) from 0.8 to 0.4, the number of cycles required for the onset of crack propagation, N_i, and for failure, N_f, is doubled for the lower material parameter. Moreover, Figures 6.4 and 6.5 indicate lower load cycles as the external stress ratio is increased from 0.4 to 0.6. This implies faster reach to the onset of crack growth and crack instability as the applied load, (σ_∞/s_0), and/or the material parameter, ($\eta s_0 a_0 /E$), is increased. From Figures 6.4 thru 6.5, one concludes that, the number of load cycles decreases with the increase in the material parameter and/or the increase of the strain hardening exponent. This decrease is more

pronounced if combined with an increase in the external load.

To demonstrate the effect of material parameters and external load on a particular strain hardening exponent, Figures 6.6 and 6.7 are developed for n=2. In these figures, the normalized length of the crack, $a(N)/a_0$, is shown versus the number of load cycles, N. Figure 6.6 shows the influence of material parameter, $(\eta s_0 a_0 /E)$, on the number of load cycles at a fixed external load and $n = 2$. It is clear that increasing the material parameter results in a lower number of cycles for the onset of crack growth and for failure. It is worthy to note that doubling the material parameter reduces the required number of cycles by half. Figure 6.7 exhibits the influence of the external applied load at constant material parameter, $(\eta s_0 a_0 /E)$, and $n = 2$. As expected, for decreasing value of the stress level, the number of load cycles required for failure increases. Figures 6.6 and 6.7 reveal that the number of cycles required for the onset of crack growth, N_i, and for failure, N_f, increase with the reduction of damage parameter, η, initial crack length, a_0, and external stress ratio, (σ_∞/s_0), for a specific strain hardening exponent.

From the results obtained thus far, one can see the same pattern observed in the mode III loading results presented in Chapter 3. This interesting finding confirms the well-known observation that mode III is instrumental in predicting mode I behavior.

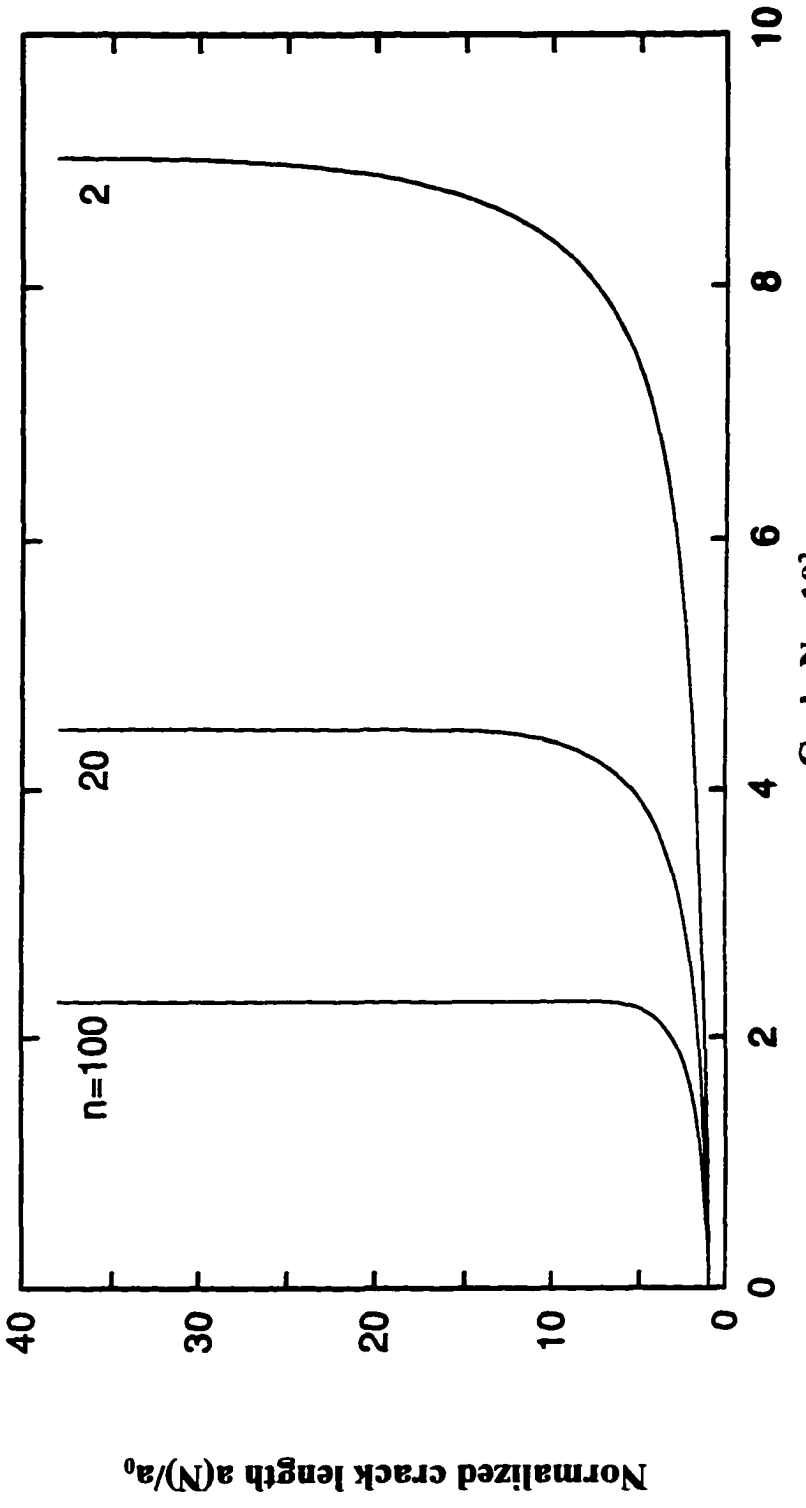

Figure 6.3 Crack growth due to cyclic loading at $\sigma_\infty/s_0 = 0.4$ and $\eta s_0 a_0/E = 0.8$.

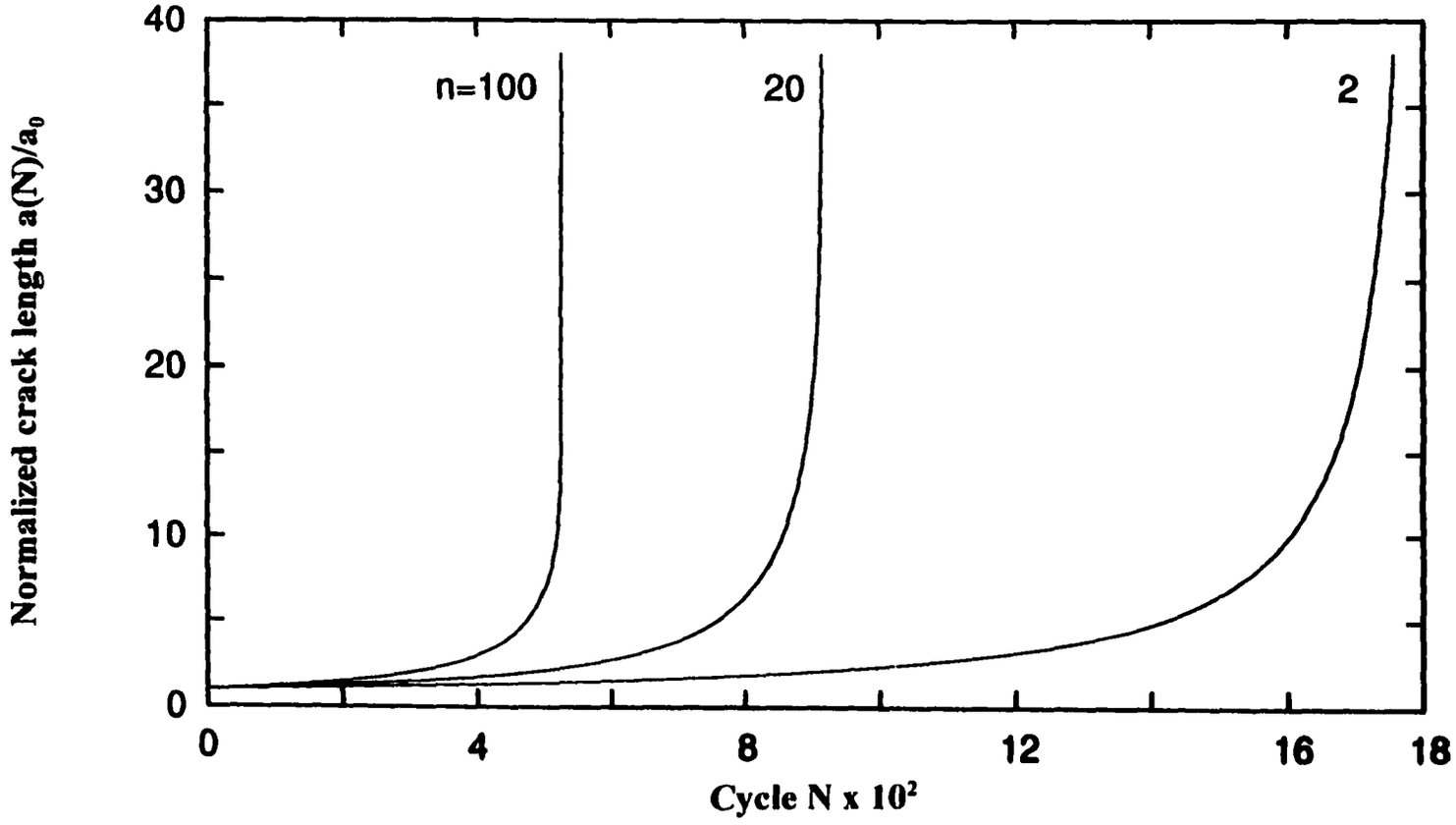

Figure 6.4 Variation of number of cycles versus normalized crack length at $\sigma_\infty/s_0 = 0.4$ and $\eta s_0 a_0 / E = 0.4$.

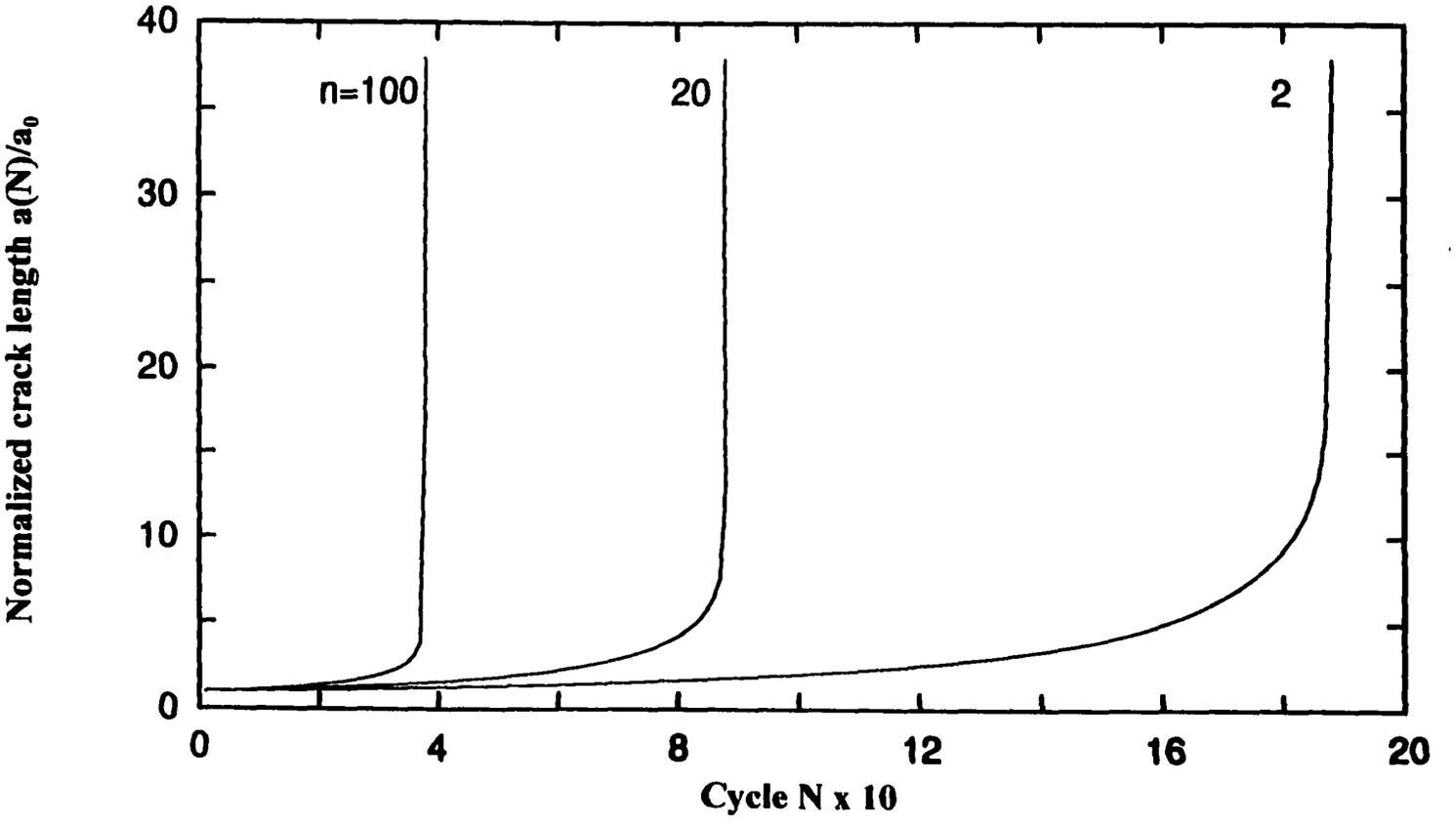

Figure 6.5 Influence of strain hardening on crack growth at $\sigma_{\infty}/s_0 = 0.6$ and $\eta s_0 a_0 / E = 0.8$.

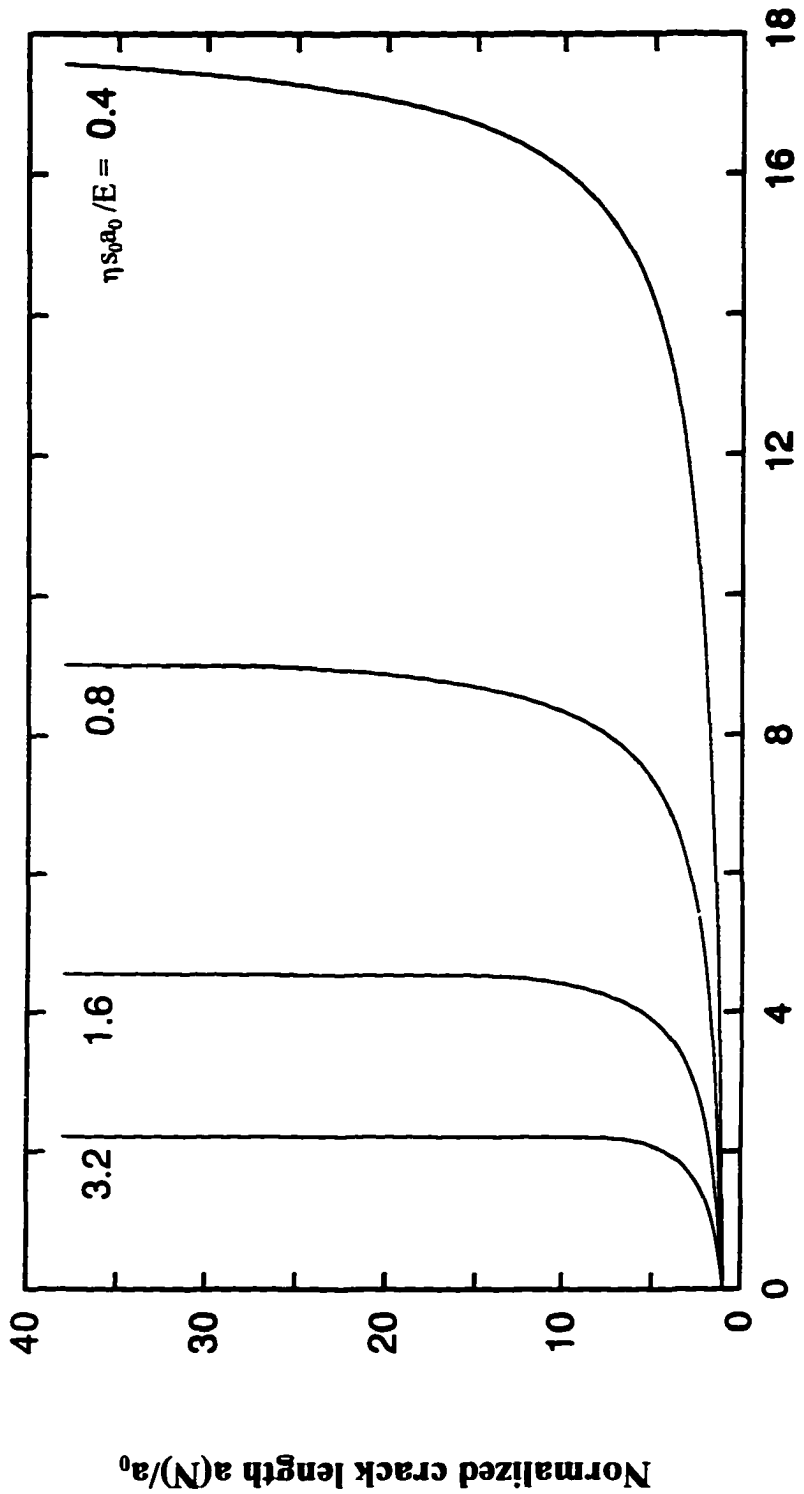

Figure 6.6 Influence of the material parameter, $\eta s_0 a_0 / E$, on fatigue crack growth at $\sigma_\infty / s_0 = 0.4$ for $n = 2$.

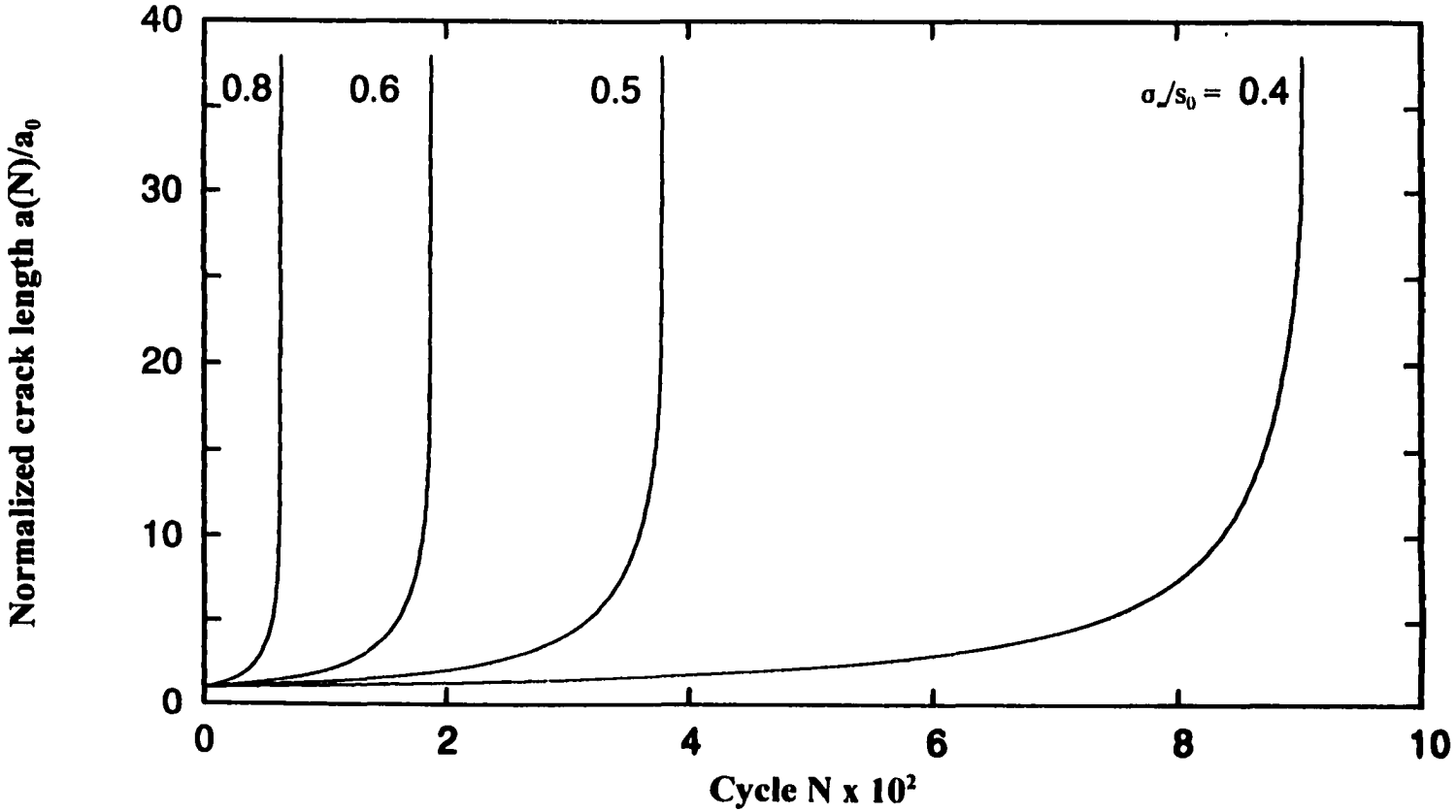

Figure 6.7 Fatigue crack growth at different external stress ratios at $\eta s_0 a_0 / E = 0.8$ for n = 2.

6.4 Time-Dependent Crack Growth

In Chapter 5, a circular creep-damage zone in terms of time parameter centered at the crack-tip was postulated and the crack growth criterion under steady-state, or secondary, creep was determined. This section presents the numerical discussion of the developed creep crack growth criterion. The numerical results are presented in two parts: First, the variation of the crack length with time, and the time required for the onset of crack growth as well as the time required to reach a critical crack length, causing instability are found, for various external loads and material parameters, and graphically exhibited in section 6.4.1. Second, the theoretical instability time, which is purely a creep phenomenon, is determined, for different external loads and material parameters and graphically displayed in section 6.4.2.

6.4.1 Steady-State Creep Crack Growth

The course of creep crack growth has been studied numerically for different material parameters and external stress levels. The numerical analysis revealed a somewhat moderate influence of the creep exponent, n=2 to n=100, on the creep process. Figures 6.8 and 6.9 exhibit the relationship between the normalized crack length, $a(t)/a_0$, and time for various creep exponents and material parameter, $(\beta s_0 a_0/E)$, at constant stress level and modular ratio, F/E. Figures 6.10 and 6.11 exhibit similar relationship between the normalized length of the crack, $a(t)/a_0$, and time for different modular ratios, F/E, at specific material parameter and stress level. Figures 6.8 through 6.11 reveal a period of incubation, where the damage accumulates with no crack growth, followed by a period of accelerating crack growth resulting in instability at a certain finite time. The crack growth period starts at the end of

the incubation period where the damage parameter reaches unity at (r, $\pi/2$) and the corresponding time is t_i, signifying the elapsed time required for the onset of crack growth. A schematic diagram depicting the appearance of the incubation and growth periods is shown in Figure 4.9.

Upon examining Figures 6.8 through 6.11, it appears that for a fixed stress value, σ_∞/s, an increase of the damage parameter, β, and/or a decrease of the ratio, F/E, will lower both the time required for the onset of crack growth and the time required for failure. In particular, the effect of initial crack length, a_0, in speeding up the crack growth can be noticed. It is also clear from examination of these figures that an increase in the stress level, σ_∞/s_0, corresponds to a decrease in the time required for the onset of crack growth and failure. This decrease will be even more pronounced when the increase in the stress level is associated with an increase in the damage parameter, β, (and/or a decrease in F/E), which implies a faster reach to the onset of crack growth and crack instability. As expected, lower stress level is needed to cause crack growth for decreasing values of the creep exponent n. The curves show how the elapsed time required for the onset of crack growth, t_i, and the elapsed time required for failure, t_f, vary with the damage parameter, β, initial crack length, a_0, external stress level, (σ_∞/s_0), and the creep exponent, n. It is clear that the elapsed time required to cause the onset of crack growth and to failure increases with reduced values of material parameter, ($\beta s_0 a_0/E$), and/or values of the creep exponent, n.

To demonstrate the effect of material parameters and external stress on a particular creep exponent, Figures 6.12 thru 6.14 are developed for n=2. Figures 6.12 thru 6.14 show the normalized length of the crack, $a(t)/a_0$, versus time for different combinations of material

parameters. In Figure 6.12, the effect of material parameter, ($\beta s_0 a_0/E$), ranging from 30.0 to 240.0, is shown for constant stress level and modular ratio. It is clear that increasing the material parameter corresponds to a decrease in the elapsed time required for failure. Figure 6.13 depicts the influence of the external stress ratio, (σ_∞/s_0), ranging from 0.3 to 0.8, for constant material parameter and modular ratio. The figure shows that an increase in the stress level will accelerate the damage process and result in a reduced elapsed time. Figure 6.14 demonstrates the effect of the modular ratio, F/E, ranging from 5.0 to 40.0, for constant stress level and material parameter. Contrary to the influence of material parameter and stress level, a decrease of the modular ratio, F/E, corresponds rather to a decrease in the elapsed time, as displayed in Figure 6.14.

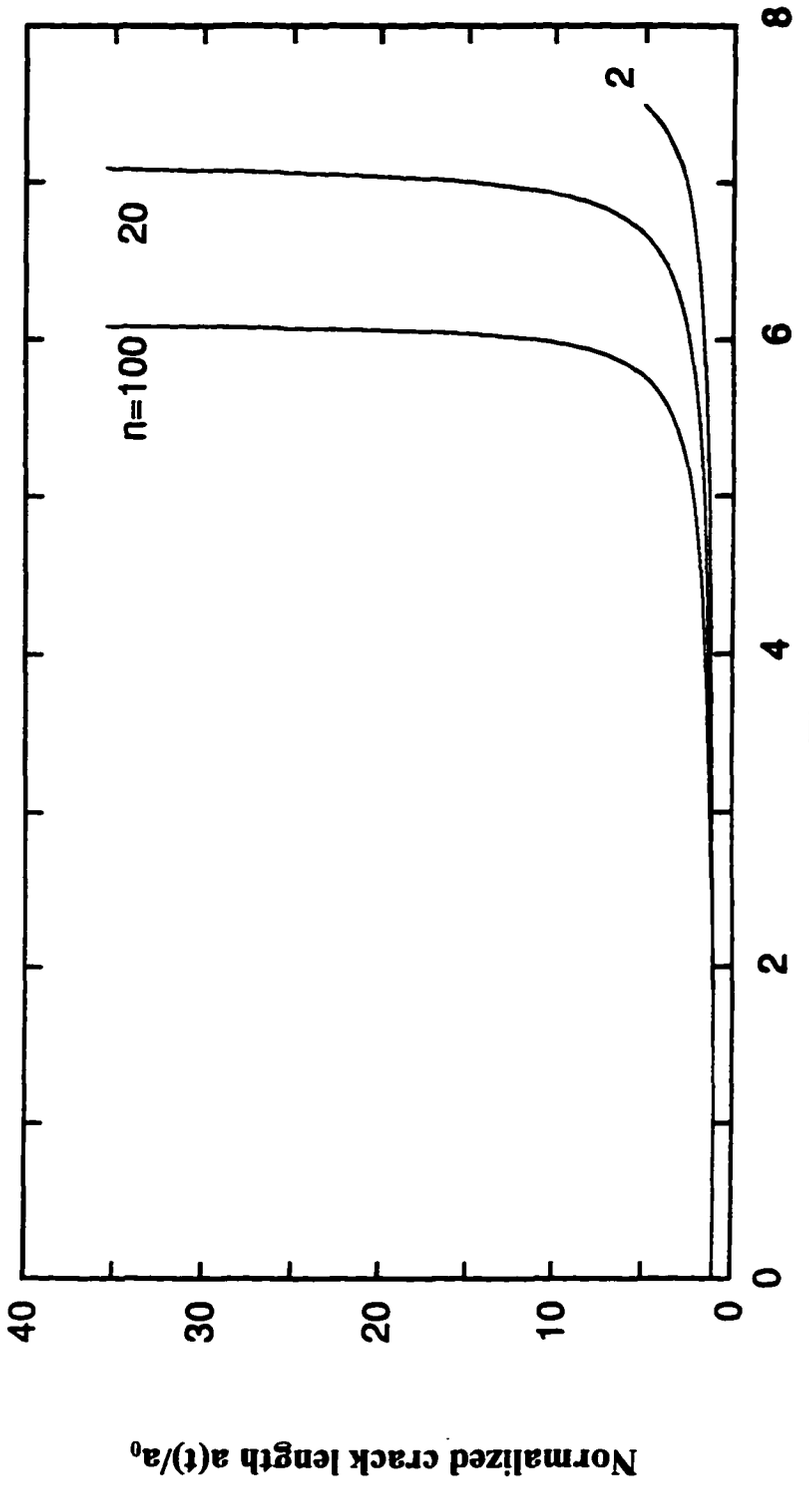

Figure 6.8 Crack growth due to steady-state creep at $\sigma_\infty/s_0 = 0.5$, F/E = 10 and $\beta s_0 a_0/E = 60$.

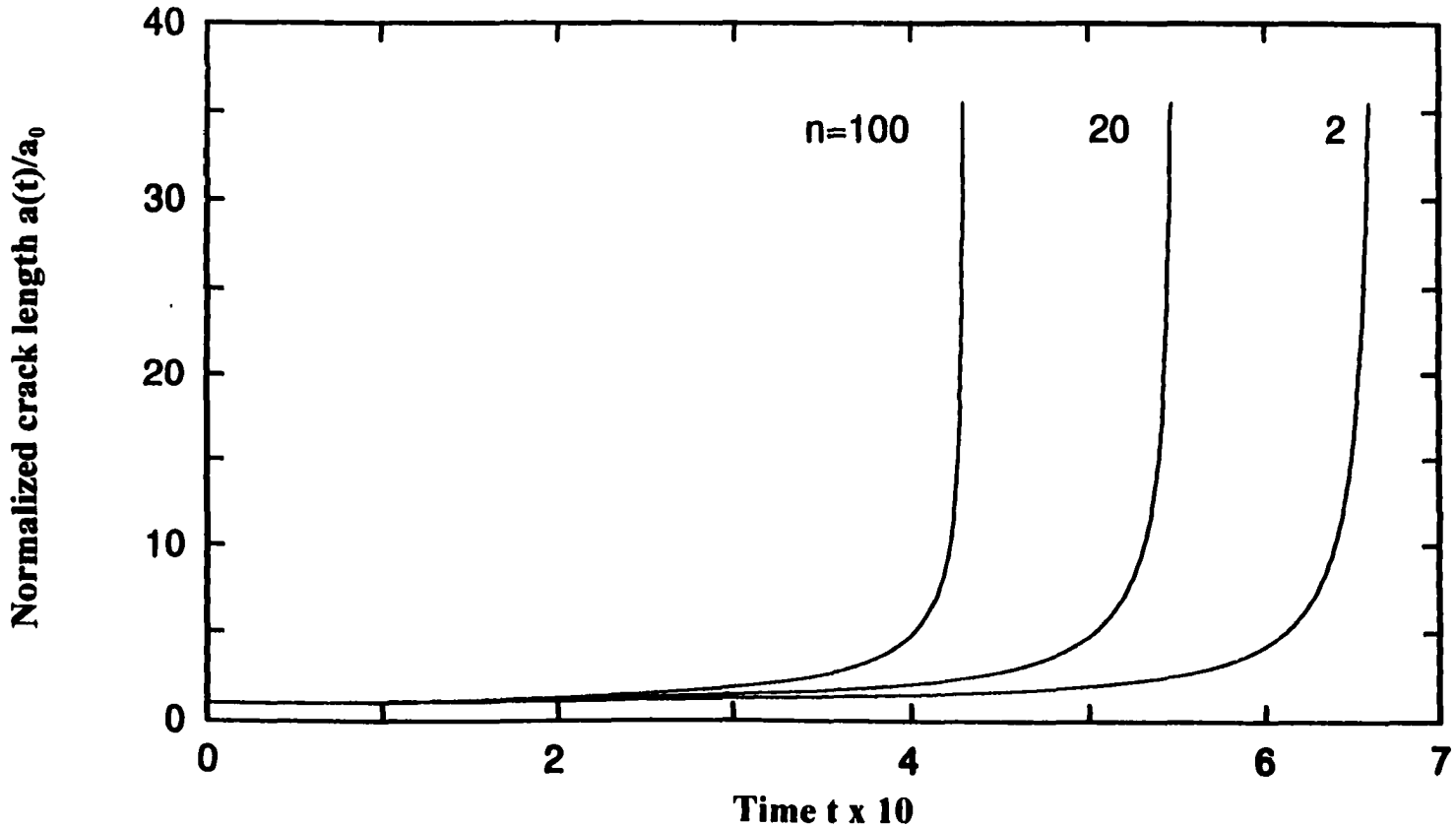

Figure 6.9 Variation of time versus normalized crack length at $\sigma_{\infty}/s_0 = 0.5$, $F/E = 10$ and $\beta s_0 a_0 / E = 120$.

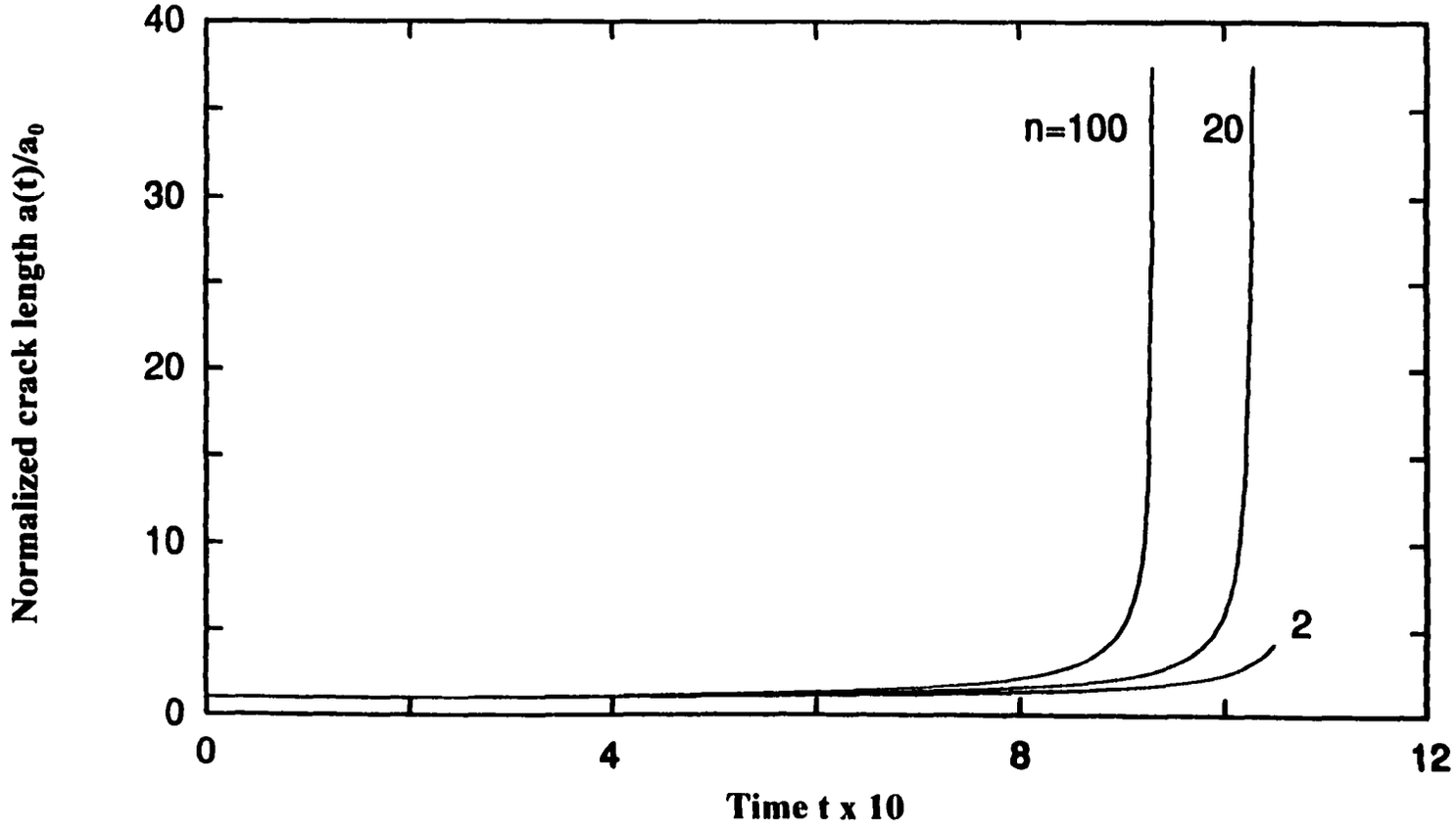

Figure 6.10 Influence of creep exponent on crack growth at $\sigma_\infty/s_0 = 0.4$, $F/E = 10$ and $\beta s_0 a_0 /E = 60$.

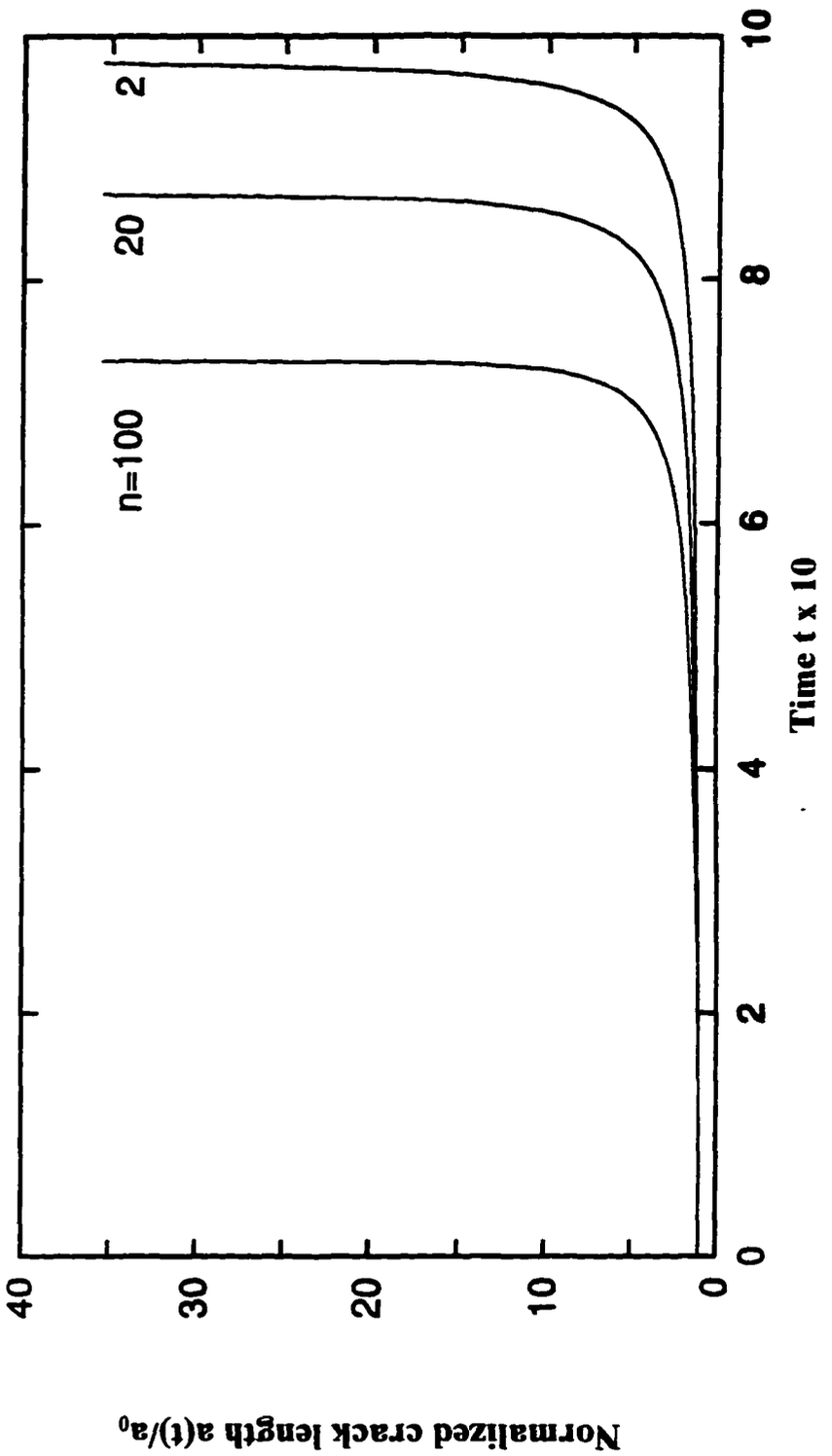

Figure 6.11 Steady-state creep crack growth at $\sigma_\infty/s_0 = 0.4$ F/E = 5 and $\beta s_0 a_0/E = 60$.

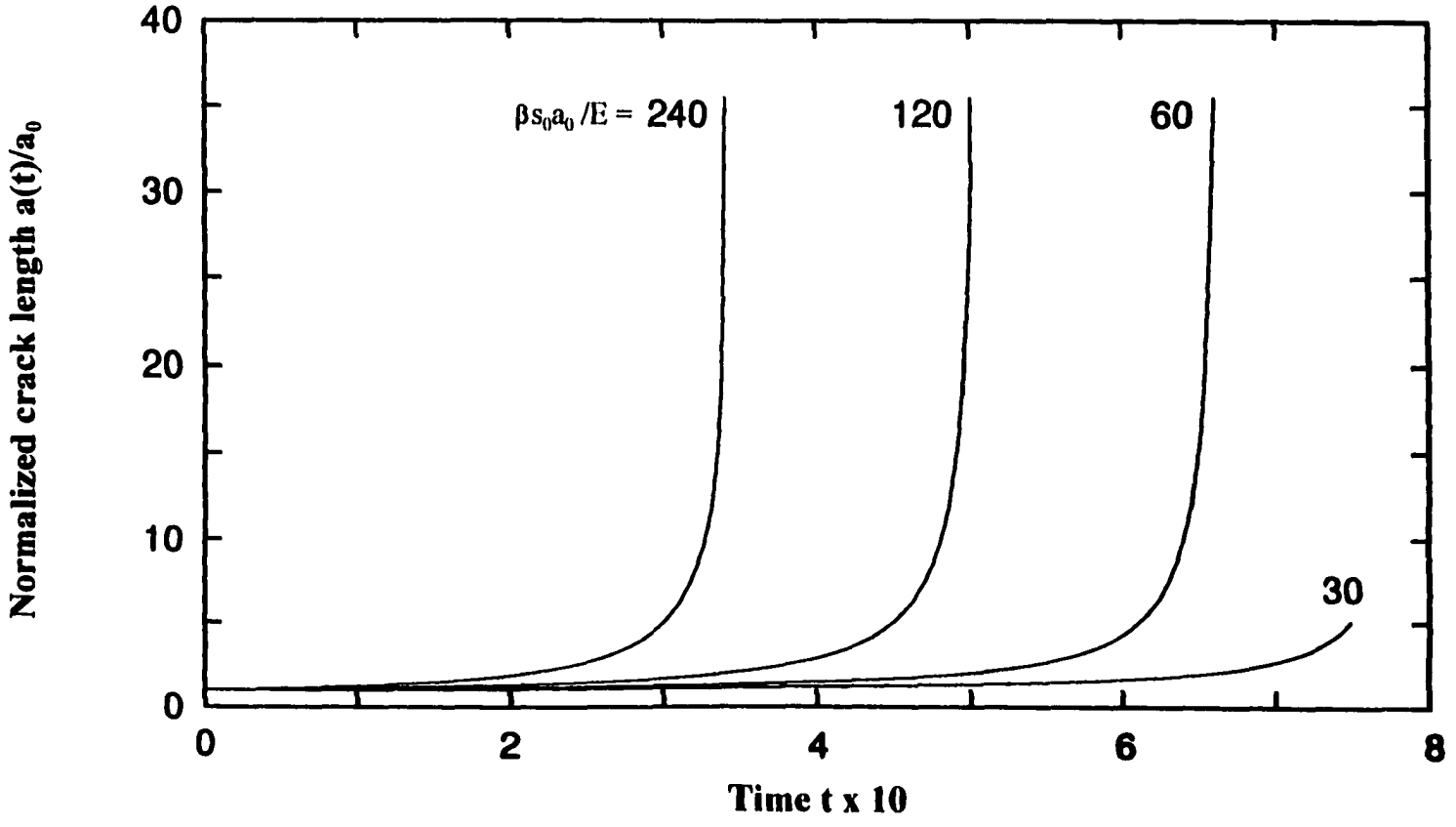

Figure 6.12 Influence of the material parameter, $\beta s_0 a_0 / E$, on creep crack growth at $\sigma_\infty / s_0 = 0.5$ and $F/E = 5$, for $n = 2$.

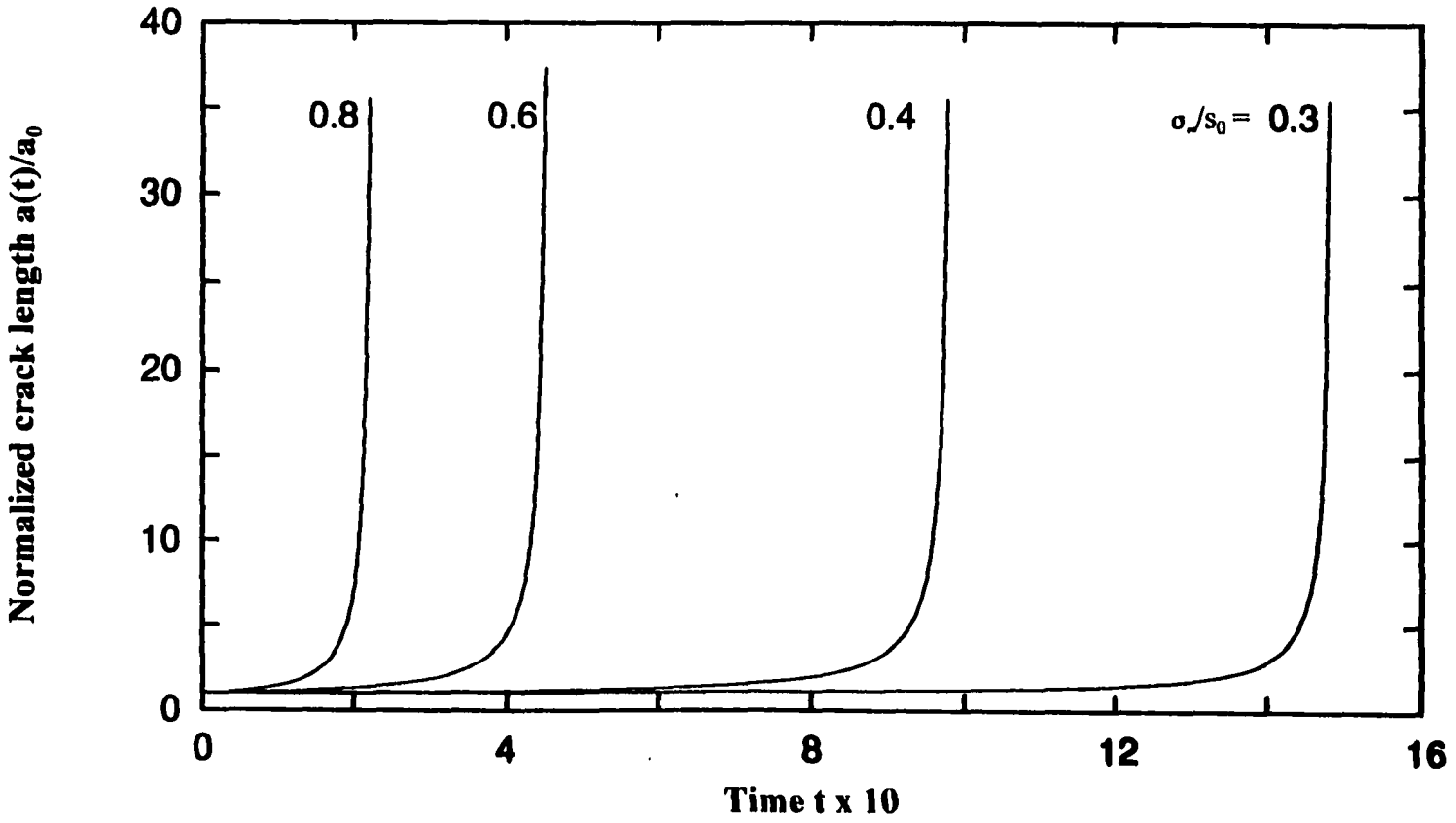

Figure 6.13 Creep crack growth corresponding to different external stress ratios at F/E = 5 and $\beta s_0 a_0 / E = 60$, for n = 2.

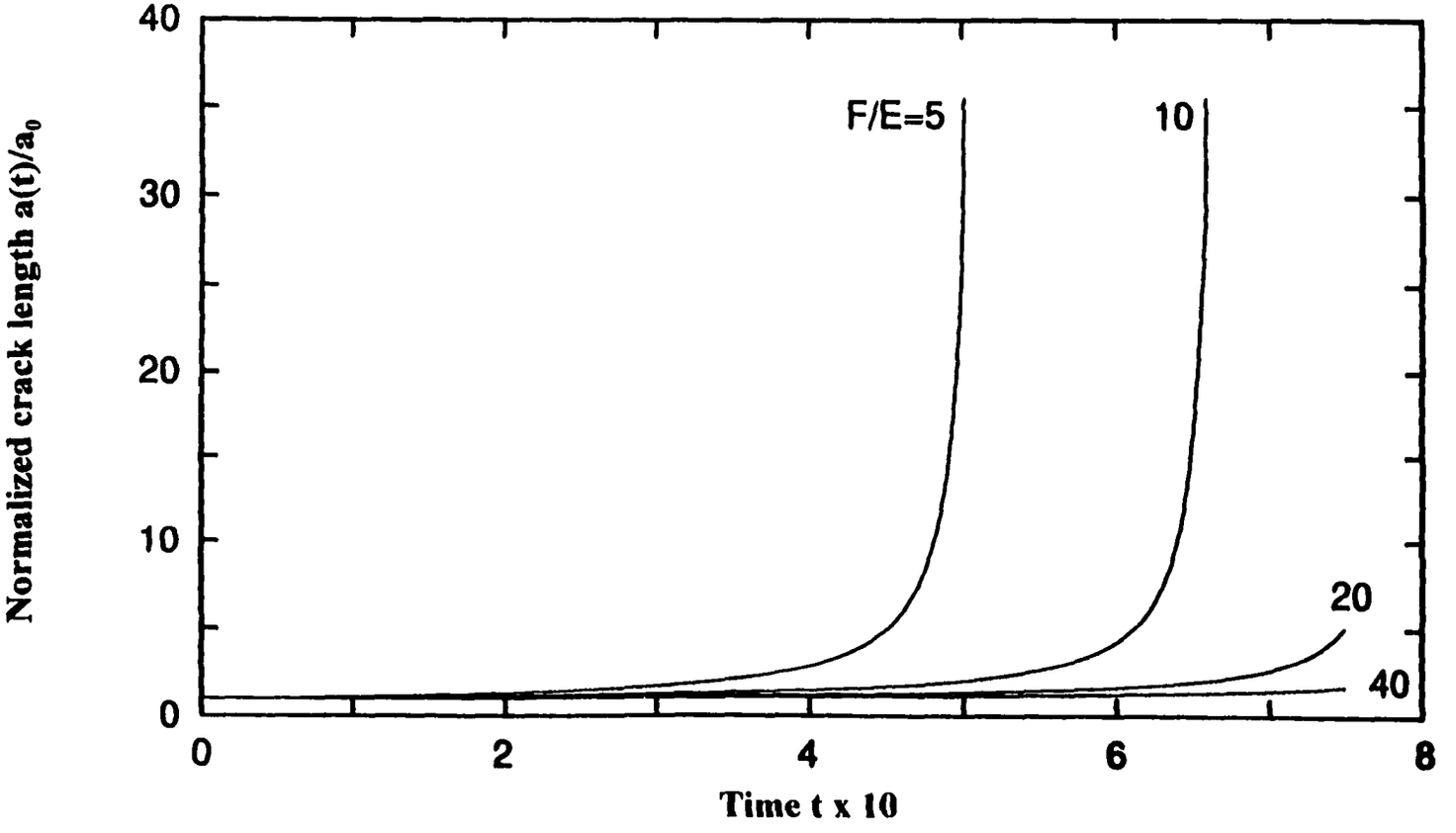

Figure 6.14 Variation of time versus normalized crack length due to different values of F/E at $\sigma_\infty/s_0 = 0.5$ and $\beta s_0 a_0 / E = 120$, for $n = 2$.

6.4.2 Theoretical Instability Time

Considering the fact that the crack grows into the material at all the time with damage D_0, the theoretical instability time, t_R, is obtained by setting $s_- = s_0$. Using equations (5.65) and (5.68), it follows that:

$$t_R = [\,1 - (\sigma_- / s_0)^{(\hat{v}+1)}\,] / [\,(\hat{v}+1)\,\kappa\,(\sigma_- / s_0)^{\hat{v}}\,] \qquad (6.1)$$

The instability time in equation (6.1), does not depend on the existence of a crack but is purely a creep phenomenon satisfying the assumption that the crack growth is not influencing the external stress. The instability time, t_R, is shown as the top curve in Figure 6.15, where log (σ_-/s_0) is plotted versus log t_R, for material parameters $(\beta s_0 a_0/E) = 60$, F/E =5, κ =.01 and $\hat{v} = 1$. However, for high values of $(\beta s_0 a_0/E)$, low values of F/E, and/ or high external stress, the crack grows to very large size compared with the initial crack length before the theoretical instability time, t_R, is reached. Therefore, t_R is not a relevant measure of the fracture time, because a real, macroscopic crack seldom has the possibility to grow to such large size under a state of constant stress. Considering this fact, log (σ_- / s_0) is plotted versus log t_2, for different values of the creep constant , n=2 to n=100, in Figure 6.15, where t_2 is the time needed to double the initial crack length, i.e., $a(t_2)=2\,a_0$. It is interesting to note that a longer time is needed to double the initial crack length for reduced values of the creep exponent, a readily established fact of the previous analysis. It is also clear that the dependence of the time t_2 on the creep exponent, n, is very mild. On the other hand, the theoretical time t_R is independent of the creep exponent, n, as indicated in equation (6.1). It should be noted that the theoretical time curve in Figure 6.15 is the envelope for other curves corresponding to different values of n. Upon further examination of Figure 6.15, it is worth

noting that at high stresses, the crack growth instability dominates, but at low stresses the creep damage instability prevails.

A theoretical instability time curve and also the time t_2 needed to double the initial crack length are plotted versus the external load ratio, (σ_- / s_0), to show the influence of different material parameters for a creep exponent, n = 2, in Figure 6.16. An important aspect shown in Figure 6.16, is the influence of the material parameter and the modular ratio. A decrease in the elapsed time is observed corresponding to an increase in the material parameter and/or a decrease in the modular ratio. The theoretical time curve in Figure 6.16 is the envelope of all the time curves generated for different material parameters.

Similar to the anti-plane mode case, it is worthy to note that the theoretical time curves in Figures 6.15 and 6.16 have an asymptotic slope of $-1/\hat{n}$ in the log-log plot when $t_R \to \infty$. It can be shown using equation (6.1), when $t_R \to \infty$, that:

$$d\,[\log(\sigma_- / s_0)]\,/\,d(\log t_R) = -1/\hat{n} \qquad (6.2)$$

From equation (6.1) this condition is satisfied when $(\sigma_- / s_0) \to 0$. For mode I calculations the slope of the theoretical time curve is found to be -1, confirming the validity of equation (6.2). It is interesting to see the identical similarity of equations (4.24) and (6.2) for mode III and mode I, respectively. This similarity reveals that the theoretical instability time exhibits the same behavior regardless what mode of loading the structural component is subjected to.

It is interesting to observe that the results obtained in this section resemble those of mode III, obtained in section 4.4. This observation suggests that the characteristics of time-dependent behavior of mode I are similar to the corresponding ones in mode III.

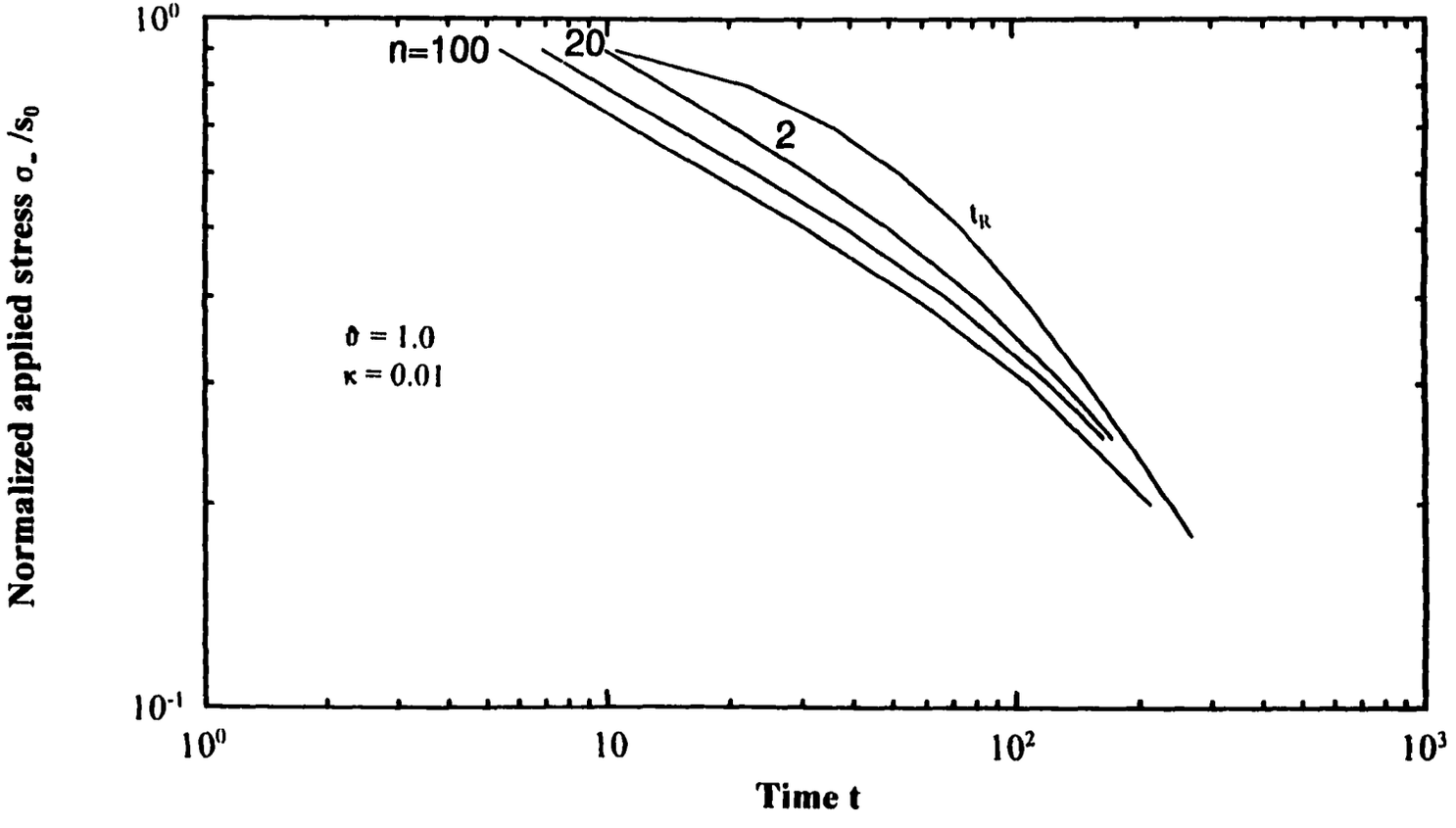

Figure 6.15 Influence of creep exponent on elapsed time needed to double the initial crack length at F/E = 5 and $\beta s_0 a_0 / E = 60$.

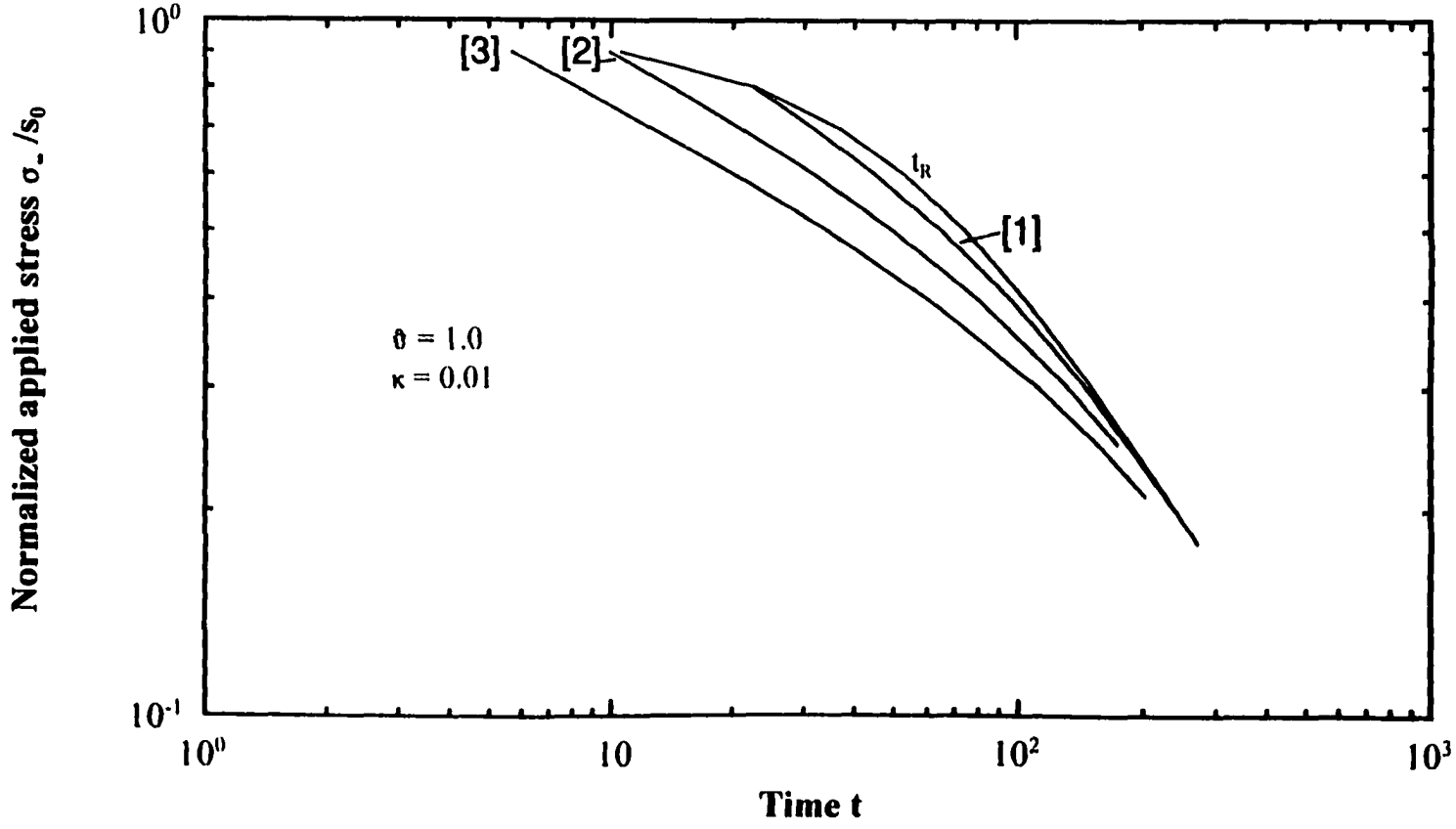

Figure 6.16 Influence of material parameters on elapsed time needed for doubling the initial crack length for n=2.
[1] $(\beta s_0 a_0 / E) = 120$ and $F/E = 20$.
[2] $(\beta s_0 a_0 / E) = 60$ and $F/E = 5$.
[3] $(\beta s_0 a_0 / E) = 120$ and $F/E = 5$.

7 SUMMARY AND CONCLUSIONS

Elastic-plastic solutions of the deformation theory of plasticity are used in conjunction with a continuum damage model to describe the conditions necessary for the onset of crack instability, fatigue crack propagation due to cyclic loading, and rates of crack growth due to steady-state creep. A power law relates the stress to the strain of the material. The damage which invokes nucleation, growth and coalescence of microvoids due to elevated strain very near the crack-tip, is confined to a damage-zone engulfing the tip.

Because of mathematical simplicities, an anti-plane crack subjected to shear loading (mode III) is used to illustrate the model. Then, the model is applied to a crack subjected to remotely in-plane tensile loading (mode I). For applied loadings below the yield stress, the small-scale and large-scale yielding solutions are used to develop a criterion for the onset of crack instability. Crack growth due to cyclic loading and due to steady-state creep are investigated.

A critical stress is found to be proportional to $a_0^{-1/(n+1)}$. For mode I, the influence of Poisson's ratio is demonstrated. It is found that the crack length required to cause the onset of crack instability has an insignificant dependence on Poisson's ratio in the large-scale yielding and more appreciable dependence in the small-scale range. For a highly ductile material, the crack sustains more external load. Fatigue crack propagation and steady-state creep crack growth results exhibit an incubation period ending with an onset of crack growth establishing a well-defined criterion for the onset of crack extension. A growth period follows immediately after the onset is triggered. It is also found that the theoretical time

curve demonstrates an asymptotic slope of $-1/\hat{v}$ when $t_R \rightarrow \infty$ for the two modes of cracking. All results indicate an interesting similarity of the basic characteristics of the two modes for crack extension and growth, an observation that is well-known from conventional fracture mechanics analyses.

The model demonstrates the powerful capabilities of continuum damage mechanics which can be used to predict failure at the microscopic level.

In modelling the interaction between fracture mechanics and damage mechanics, this study differs from previous similar studies in its consideration of the strain hardening of the material past the yield point. It also introduces a criterion of pin-pointing the onset of crack growth through a clear definition of the incubation period for time-dependent and time-independent deformations. Through the revealed results, this study lays out another bench-mark in establishing damage mechanics as a powerful tool in achieving interaction with the well-established nonlinear fracture mechanics techniques.

8 SUGGESTIONS FOR FUTURE RESEARCH

The most obvious extensions to this research effort would be those issues identified as limitations throughout the dissertation. These include, but not limited to, the following:

- Assuming a more complicated form of the continuity function that is not constant in the damage-zone.
- Development of a different damage law by postulating damage to be proportional to critical principal strain or considering a kinematic evolution of damage.
- Identification of damage parameters, λ,η, and β, which involves extensive experimental work.
- Extending the model to study mode II (sliding mode) behavior and develop a criterion for the mixed mode problem.
- Assuming no elastic damage, the model demonstrates a "fractal set" characterization of damage, suggesting that damage is a self-similar process, an issue that needs much further explorations on the possible relation between metal fracture and the chaotic nature of fractal geometry.

References

[1] Bolotin, V. V., *Statistical Methods in Structural Mechanics*. Izd. Literaturi po Stroitel'stvu, Moscow, 1965.

[2] Cherepanov, G., *Mechanics of Brittle Fracture*. McGraw-Hill Book Inc., New York, Translated from Russian, 1979.

[3] Kachanov, L.M., "Time of The Rupture Process Under Creep Condition." Izv. Akad. Nauk SSSR, Otd. Tekh. Nauk (8), pp. 26-31, 1958.

[4] Rabotnov, Y. N., "Creep Rupture." Proc. 12th. Int. Congr. Appl. Mech., pp.342-349, Springer, Berlin, 1969.

[5] Krajcinovic, D., "Damage Mechanics." Mechanics of Materials, Vol. 8, pp. 117-197, 1989.

[6] Janson, J. and Hult, J., "Fracture Mechanics and Damage Mechanics - A Combined Approach." Journal de Mecanique Appliquee, Vol. 1, pp. 69-84, 1977.

[7] Lemaitre, J. and Chaboche, J.L., *Mechanics of Solid Materials*. Cambridge University Press, 1990.

[8] Leckie, F.A. and Hayhurst, D.R., "Creep Rupture of Structures." Proc. Royal Soc., London, Vol. 340, pp. 323-347, 1974.

[9] Hult, J., *Creep in Contiua and Structures*. Topics in Applied Continuum Mechanics, pp. 137-155, Springer, Wien, 1974.

[10] Broberg, H., *Creep Damage and Rupture*. Ph. D. Dissertation, Chalmers University of Technology, Goteborg, Sweden, 1975.

[11] Krajcinovic, D. and Foneska, G. U., "The Continuous Damage Theory of Brittle Materials-Parts I and II." Journal of Applied Mechanics, Vol. 48, pp. 809-824, 1981.

[12] Hutchinson, J. W., "Singular Behavior at The End of a Tensile Crack in a Hardening Material." Journal of the Mechanics and Physics of Solids, Vol. 16, pp. 13-31, 1968.

[13] Rice, J. R. and Rosengren, G. F., "Plane Strain Deformation Near a Crack Tip in a Power-Law Hardening Material." Journal of the Mechanics and Physics of Solids, Vol. 16, pp. 1-12, 1968.

[14] Rice, J. R. "A Path-Independent Integral and The Approximate Analysis of Strain Concentration by Notches and Cracks." Journal of Applied Mechanics, Vol. 35, pp. 379-386, 1968.

[15] Eshelby, J. D., *The Energy Momentum Tensor in Continuum Mechanics.* Inelastic Behavior of Solids, Edited by M.F. Kanninen *et al.*, McGraw-Hill, New York, 1970.

[16] Begley, J. A. and Landes, J. D., "The J-Integral as a Fracture Criterion." ASTM STP 514, American Society for Testing and Materials, Philadelphia, pp. 1-20, 1972.

[17] E 813-81, "Standard Test Method for J_{IC}, a Measure of Fracture Toughness." American Society for Testing and Materials, Philadelphia, 1981.

[18] Shih, C. F. and Hutchinson, J. W., "Fully Plastic Solutions and Large-Scale Yielding Estimates for Plane Stress Crack Problems." Journal of Engineering Materials and Technology, Vol. 98, pp. 289-295, 1976.

[19] Kumar, V., German, M. D. and Shih, C. F., "An Engineering Approach for Elastic-Plastic Fracture Analysis." EPRI Report NP-1931, Electric Power Research Institute, Palo Alto , Ca., 1981.

[20] Shih, C. F., "Relationship Between the J-Integral and The Crack Opening Displacement for Stationary and Extending Cracks." Journal of the Mechanics and Physics of Solids, Vol. 29, pp. 305-326, 1981.

[21] Burdekin, F. M. and Dawes, M. G., "Practical Use of Linear Elastic and Yielding Fracture Mechanics with Particular Reference to Pressure Vessels." Proceedings of the Institute of Mechanical Engineers Conference, London, pp. 28-37, May 1971.

[22] Wells, A. A., "Unstable Crack Propagation in Metals: Cleavage and Fast Fracture." Proceedings of the Crack Propagation Symposium, Vol 1, Paper 84, Cranfield, UK, 1961.

[23] Harrison, R. P., Loosemore, K., Milne, I, and Dowling, A. R., "Assessment of The Integrity of Structures Containing Defects." Central Electricity Generating Board Report R/H/R6-Rev 2, UK, April, 1980.

[24] Dugdale, D. S., "Yielding of Steel Sheets Containing Slits." Journal of the Mechanics and Physics of Solids, Vol. 8, pp. 100-104, 1960.

[25] Barenblatt, G. I., *The Mathematical Theory of Equilibrium Cracks in Brittle Fracture.* Advances in Applied Mechanics, Vol. 7, Academic Press, pp. 55-129, 1962.

[26] Janson, J., "A Continuum Damage Approach to the Fatigue Process." Engineering Fracture Mechanics, Vol. 10, pp. 651-657, 1978.

[27] Janson, J., "Damage Model of Crack Growth and Stability." Engineering Fracture Mechanics, Vol. 10, pp. 795-806, 1978.

[28] Alam, M. A. and Kassir, M. K., "Plastic Strip Model of Circular Crack Under Cyclic Loading With Damage Accumulation." Theoretical and Applied Fracture Mechanics, Vol. 26, pp. 81-87, 1997.

[29] Argon, A., S., Im, J. and Safogln, R., "Cavity Formation From Inclusion in Ductile Fracture." Metallurgical Transactions, Vol. A6, pp. 825-837, 1975.

[30] Ritchie, R. O. and Thompson, A. W., "On Macroscopic and Microscopic Analyses for Crack Initiation and Crack Growth Toughness in Ductile Alloys." Metallurgical Transactions, Vol. 16A, pp. 233-248, 1985.

[31] Miyamoto, H., Machida, K., Okaysu, H. and Kawazoe, T., "Study of The Process Zone at the Crack Tip (Behaviour of the Voids at the Crack Tip of Aluminum Alloy Specimen)." Mechanical Behaviour of Materials, V, ICM-5, M.G. Yan et al. (eds.), Vol. 1, Pergamon Press, Oxford, pp. 39-50, 1987.

[32] Griffith, A.A., "The Phenomena of Rupture and Flaw in solids." Philosophical Transactions, Series A, Vol. 221, pp. 163-198, 1920.

[33] Rice, J.R., "Stresses Due to a Sharp Notch in a Work-Hardening Elastic-Plastic Material Loaded by Longitudinal Shear." Journal of Applied Mechanics, Vol. 34, pp. 287-298, 1967.

[34] Neuber, H., "Theory of Stress Concentration for Shear Strained Prismatical Bodies With Arbitrary Nonlinear Stress-Strain Law." Journal of Applied Mechanics, Vol. 28, Trans. ASME, Vol. 83, Series E, pp. 544-550, 1961.

[35] Courant, R.A. and Friedricks, K.O., *Supersonic Flow and Shock Waves*. Interscience Publisher Inc., New York, N.Y., 1948.

[36] Lemaitre, J., "A Continuum Damage Mechanics Model for Ductile Fracture." Journal of Engineering Materials and Technology, Vol. 107, pp. 83-89, 1985.

[37] Lemaitre, J. and Chaboche, J. L., "Aspect Phenomenologique de la Rupture Par Endommagement." Journal de Mecanique Appliquee, Vol. 2, pp. 317-365, 1978.

[38] Hayhurst, D. R. and Leckie, F. A., "The Effect of Creep Constitutive and Damage Relationships Upon the Rupture Time of a Solid Circular Torsion Bar." Journal of Mechanics and Physics of Solids, Vol. 21, pp. 431-446, 1973.

[39] Lemaitre, J., *A Course on Damage Mechanics*. Springer Verlag, 1992.

[40] Amazigo, J.C., "Fully Plastic Crack in an Infinite Body Under Anti-Plane Shear." Int. Journal of Solids Structures, Vol. 10, pp. 1003-1015, 1974.

[41] Anderson, T.L., *Fracture Mechanics, Fundamentals and Applications*. CRC Press, Inc., 1991.

[42] Riedel, H. and Rice, J.R., "Tensile Cracks in Creeping Solids." Fracture Mechanics: Twelfth Conference, ASTM STP 700, American Society for Testing Materials, Philadelphia, pp. 112-130, 1980.

[43] Riedel, H., "Creep Deformation at Crack Tips in Elastic-Viscoplastic Solids." Journal of the Mechanics and Physics of Solids, Vol. 29, pp. 35-49, 1981.

[44] Goldman, N.L. and Hutchinson, J.W., "Fully Plastic Crack Problems: The Center-Cracked Strip Under Plane Strain." Int. Journal of Solids Structures, Vol. 11, pp. 575-591, 1975.

[45] Hoff, N. J., "Approximate Analysis of Structures in the Presence of Moderately Large Creep Deformations." Quarterly of Applied Mathematics, Vol. 12, pp. 49-55, 1954.

[46] Shih, C. F., "Tables of Hutchinson-Rice-Rosengren Singular Field Quantities." Brown University Report MRL E-147, June 1983.

[47] Tracey, D. M., "Finite Element Solutions for Crack-Tip Behavior in Small-Scale yielding." Journal of Engineering Materials and Technology, Vol. 98, pp. 146-151, 1976.

[48] McMeeking, R. M., "Finite Deformation Analysis of Crack Tip Opening in Elastic-Plastic Materials and Implications for Fracture." Journal of Mechanics and Physics of Solids, Vol. 25, pp. 357-381, 1977.

[49] Rice, J. R., McMeeking, R. M., Parks, D. M. and Sorensen, E. P., "Recent Finite Element Studies in Plasticity and Fracture Mechanics.", Journal of Computer Methods in Applied Mechanics and Engineering, Vol. 17/18, pp. 411-442, 1979.

[50] Hutchinson, J. W., "Fundamentals of the Phenomenological Theory of Nonlinear Fracture Mechanics." Trans. of the ASME, Vol. 50, pp. 1042-1051, 1983.

[51] Kanninen, M. F. and Popelar, C. H., *Advanced Fracture Mechanics*. Oxford University Press, 1985.

[52] Rice, J. R., *Mathematical Analysis in the Mechanics of Fracture*. Fracture - An Advanced Treatise, Vol. II, Liebowitz (ed.), Academic, New York, pp. 191-308, 1968.

[53] McMeeking, R. M., Parks, D. M., "On Criteria for J-Dominance of Crack Tip Fields in Large-Scale Yielding." ASTM STP 668, American Society for Testing and Materials, Philadelphia, pp. 175-194, 1979.